Exxon Valdez Oil Spill
Gulf Ecosystem Monitoring and Research Project Final Report

Evaluation of Airborne Remote Sensing Tools for GEM Monitoring

GEM Project 030584
Final Report

Evelyn Brown[1]
James H. Churnside[2]
Susan Hills[1]
Richard Collins[3]
Robert Foy[1]

1. School of Fisheries and Ocean Science
University of Alaska
Institute of Marine Science
PO Box 757220
Fairbanks, AK 99775-7220

2. NOAA Environmental Technology Laboratory
R/E/ET1
325 Broadway
Boulder, Colorado 80303

3. Geophysical Institute
University of Alaska
PO Box 757320
Fairbanks, Alaska 99775-7320

December 2006

Exxon Valdez Oil Spill
Gulf Ecosystem Monitoring and Research Project Final Report

Evaluation of Airborne Remote Sensing Tools for GEM Monitoring

GEM Project 030584
Final Report

Evelyn Brown[1]
James H. Churnside[2]
Susan Hills[1]
Richard Collins[3]
Robert Foy[1]

1. School of Fisheries and Ocean Science
University of Alaska
Institute of Marine Science
PO Box 757220
Fairbanks, AK 99775-7220

2. NOAA Environmental Technology Laboratory
R/E/ET1
325 Broadway
Boulder, Colorado 80303

3. Geophysical Institute
University of Alaska
PO Box 757320
Fairbanks, Alaska 99775-7320

December 2006

Evaluation of Airborne Remote Sensing Tools for GEM Monitoring

GEM Project 030584
Final Report

Study History: During 2001 and 2002, an airborne, remote sensing project was conducted to address two main research goals. The first goal was to compliment a suite of studies designed to address questions concerning severe declines in the Steller sea lion population, especially in the western Gulf of Alaska region, funded by the Steller Sea Lion Research Initiative (SSLRI) program. The second goal was to evaluate the usefulness of aerial remote sensing in ecological monitoring of the Gulf of Alaska as part of the *Exxon Valdez* Oil Spill Trustee Council (EVOS TC) Gulf Ecosystem Monitoring (GEM) program. Because the study area and data collection needs for the two programs overlapped, the two studies were conducted simultaneously and results are therefore combined in one report.

Abstract: During 2001 and 2002, an airborne remote sensing project was completed that encompassed two main goals: 1) contribute to a suite of studies designed to determine why western Alaska Steller sea lion populations have declined so drastically, and 2) to evaluate airborne remote sensing in relation to the Exxon Valdez Oil Spill Trustee Council's Gulf Ecosystem Monitoring (EVOS TC GEM) program. For the sea lion work, we proposed to address questions directly related to food availability and variations in the type and distribution of prey available; in areas with decline, preferred food types were hypothesized to be less available and patchy in distribution. Approximately 300 hrs were flown over a region expanding from the eastern Aleutian Chain to northern Southeast Alaska spanning over the entire Gulf of Alaska (GOA). Surveys were especially concentrated in two regions for the sea lion work: Kodiak where the population is in decline and Southeast Alaska where the population is stable or expanding. Surveys were also concentrated along the Seward Line south of Prince William Sound and across the continental shelf in coordination with major scientific studies and within the GEM region. The airborne instrument package consisted of 1) a lidar (light detection and ranging) using pulsed green laser light to map subsurface, vertical biological features day and night to a maximum of 50 m, 2) an infrared radiometer to map SST day (similar to AVHRR satellite data), 3) a low-light level CCD gated camera synchronized with lidar pulses and used to obtain subsurface imagery of biological targets observed with reflected lidar signal, 4) a 3-chip digital color video set up to map ocean color (chlorophyll), ocean fronts, near-surface fish schools, and seabird or mammal aggregations, 5) an infrared digital video to map birds and mammals at night, and in 2002, 6) a MicroSAS used to measure ocean color.

Key Words: Remote sensing tools, Steller sea lion, lidar, IR radiometer, ocean color video, high resolution digital video, IR video

Project Data: Five types of data were acquired: 1) lidar system data, 2) digital video imaging footage, 3) MicroSAS ocean color binary files, 4) log files from the navigational software, and 5) video footage from the gated video. From the synchronized lidar system, raster files were created that contained header information followed by a time coded sequence of depth-specific registered optical signal resulting from reflectance of laser light on particles in the water column.

Within the header and each line of the file, latitude, longitude, and a GMT time code were coded and each file represented 60 seconds of along path data. Digital video images were recorded on 1 hr digital tapes with a separate tape for color and for thermal data. MicroSAS data was recorded directly to the lap-top computer that controlled the lidar system. The raw MicroSAS files are binary in a proprietary format from Satalantic. Navigation log files were recorded directly to a separate lap-top also in a binary proprietary format particular to the software. Gated video footage was recorded directly to digital tapes and was collected intermittently when conditions were optimal for camera testing and when large sub-surface biological targets (fish and marine mammals) were observed that needed to be identified. The first four data types were collected at all times during aerial surveys. Data is available by contacting Evelyn Brown, School of Fisheries and Ocean Science University of Alaska, Institute of Marine Science, PO Box 757220, Fairbanks, AK 99775-7220

Citation: Brown, E.D., J.H. Churnside, S. Hills, R.L. Collins, and R. Foy. 2006. Evaluation of airborne remote sensing tools for GEM Monitoring, *Exxon Valdez* Oil Spill Gulf Ecosystem Monitoring and Research Project Final Report (GEM Project 030584), University of Alaska, Fairbanks, Alaska.

Table of Contents

Executive Summary

During 2001 and 2002, an airborne remote sensing project was completed that encompassed two main goals: 1) contribute to a suite of studies designed to determine why western Alaska Steller sea lion populations have declined so drastically, and 2) to evaluate airborne remote sensing in relation to the Exxon Valdez Oil Spill Trustee Council's Gulf Ecosystem Monitoring (EVOS TC GEM) program. For the sea lion work, we proposed to address questions directly related to food availability and variations in the type and distribution of prey available; in areas with decline, preferred food types were hypothesized to be less available and patchy in distribution. Approximately 300 hrs were flown over a region expanding from the eastern Aleutian Chain to northern Southeast Alaska spanning over the entire Gulf of Alaska (GOA). Surveys were especially concentrated in two regions for the sea lion work: Kodiak where the population is in decline and Southeast Alaska where the population is stable or expanding. Surveys were also concentrated along the Seward Line south of Prince William Sound and across the continental shelf in coordination with major scientific studies and within the GEM region. The airborne instrument package consisted of 1) a lidar (light detection and ranging) using pulsed green laser light to map subsurface, vertical biological features day and night to a maximum of 50 m, 2) an infrared radiometer to map SST day (similar to AVHRR satellite data), 3) a low-light level CCD gated camera synchronized with lidar pulses and used to obtain subsurface imagery of biological targets observed with reflected lidar signal, 4) a 3-chip digital color video set up to map ocean color (chlorophyll), ocean fronts, near-surface fish schools, and seabird or mammal aggregations, 5) an infrared digital video to map birds and mammals at night, and in 2002, 6) a MicroSAS used to measure ocean color.

The major findings of this study spanned several topics. Concerning the sea lion hypothesis, we found no evidence that areas with sea lion declines were less productive and had fewer available forage resources than areas with stable or increasing populations. Rather, we found areas with declining sea lion populations to be higher in marine production in terms of zooplankton and euphausiid density and abundance of surface fish schools consisting mainly of high energy species. We were able to demonstrate the extreme diel change in structure of fish and zooplankton around Kodiak Island and the spatial patchiness of features by depth and over small spatial scales. Surface waters over topographical gullies near Kodiak were especially productive in terms of density of biological features. Storm-induced variability in the sea surface ecology was found to be dramatic over time scales of a week or less. We observed changes in SST, primary production and Chlorophyll a, and day and night distribution and density of fish and zooplankton. Marine sea bird and mammal foraging behaviors also shifted. This short-term variability likely has a large impact on overall ecosystem productivity and implications on interpretation of ship survey data that spans such a storm event. Direct comparisons between areas cannot be considered valid if one area was surveyed before and the other after a storm. We were able to document that large ships (over 30 m) had dramatic affects on schooling forage fish distribution causing schools to move laterally or vertically to avoid the vessel. We were able to directly relate lidar signal by depth with

zooplankton abundance and biomass sampled with depth-specific nets. Strong correlations were found between lidar signal and several large zooplankton groups. Small zooplankton species were poorly correlated with lidar signal. We also observed correlations of plankton density from lidar and net data to SST and Chl a measured from aircraft. Lidar signal indicated fine scale vertical structure in the plankton community and the presence of a "two-layer" plankton distribution also observed in net sampling. The implications of these results are that airborne methods can appropriately measure large zooplankton abundance, distribution, and relationship to environmental characteristics. In contrast to a vessel, airborne techniques can be used to cover large spatial areas and perform high resolution temporal sampling appropriately matching the patchiness and variation observed in GOA plankton. If appropriately validated, lidar can be used to map zooplankton community structure that has large implications for fish, bird and mammal community structure. Using a combination of airborne and satellite data, we were able to estimate phytoplankton biomass and develop algorithms specific and appropriate for Alaskan coastal waters. The use of airborne video was evaluated with three instrument types: RGB multispectral, thermal and CCD low-light level gated and synced with the laser. The multispectral images proved most useful for determining values of ocean color (Chl a proxy) and for interpreting data from other sources (lidar and thermal imager). The thermal imager has incredible potential for sea bird and marine mammal census and should be tested on a more expansive scale. The gated video is useful in interpreting lidar signal resulting from fish schools and is best used in areas of known fish distribution. The cost of aircraft, fuel, personnel time and data processing costs (approximated at 3:1 processing time to data collection) was approximately $1400 per hour for this study. At a typical survey speed of 125 knots, the cost of data collection per km is $5.20. A typical ship survey including vessel and scientific crew costs and excluding data processing costs is $15,000 per day. Given a 12 hr work day and average data collection speed over the period of 6 knots, the cost of data collection per km is estimated at $112.5. It is not suggested that airborne survey techniques replace ship surveys, but rather be used to expand studies, especially of processes occurring in the upper 50 m of the ocean. In subarctic waters, this is the most productive region. Airborne methods would be especially useful in exploring processes with high short-term variability, such as primary and secondary ocean production, in increasing the probability of detection of ephemeral events, such as apex predator foraging bouts, and in expanding the spatial coverage of ocean surveys. We have merely "scratched the surface" of possibilities for data collection and marine science inquiry using these techniques and the data we have collected. Our data has been archived and could be of use for future investigations, data sharing and collective analyses. It is our hope this can be accomplished.

Introduction

During 2001 and 2002, an airborne, remote sensing project was conducted to address two main research goals. The first goal was to compliment a suite of studies designed to address questions concerning severe declines in the Steller sea lion population, especially in the western Gulf of Alaska region, funded by the Steller Sea Lion Research Initiative (SSLRI) program. The second goal was to evaluate the usefulness of aerial remote sensing in ecological monitoring of the Gulf of Alaska as part of the *Exxon Valdez* Oil Spill Trustee Council (EVOS TC) Gulf Ecosystem Monitoring (GEM) program. Because the study area and data collection needs for the two programs overlapped, the two studies were conducted simultaneously and results are therefore combined in this report.

For the SSLRI work, our project addressed six research priorities and was coordinated with ongoing shipboard sea lion research programs in three areas in Alaska (Kodiak, Lower Cook Inlet, and Southeast AK) during two time periods (late spring, late summer). The overall objective was to compare synoptic marine ecological information between two sea lion foraging regions over large spatial regions at three temporal scales (diurnal, seasonal, interannual), supplementing data from the existing surveys. One region (Southeast Alaska) had a healthy population and the other (Kodiak) had a population in decline. The secondary objective was to cover regions not accessible by ship in the extreme nearshore and upper surface (< 5 m) and to extend coverage beyond ship transects. The hypotheses to be addressed were:

> *Easily obtainable (near-surface, near-shore) and preferred (high energetic value) sources of food for Steller sea lions are lower abundance near Kodiak Island than in southeast Alaska;*

> *Sea lion foraging patterns reflect the spatial and temporal patchiness in prey fields; foraging tends to occur in accessible, productive areas where preferred prey and secondary production is concentrated.*

Using airborne remote sensing instrumentation (including lidar, IR radiometer, ocean color video, high resolution digital video, and IR video), we mapped ocean fronts, chlorophyll, zooplankton, fish prey resources, fish and marine mammal predators, predator/prey interactions (foraging bouts), and human activity in the upper 50 m of the water column during the day and night. We used shipboard results for signal validation and interpretation. We linked aerial to satellite data, and perform geostatistical analysis for interpretation.

For the EVOS TC GEM work, the four objectives were: 1) determine the types of information that can be collected from remote sensing instrumentation and the limitations of the collection, 2) interpret the information collected in an ecological sense, 3) evaluate the extent of data collected and cost-effectiveness per unit area, and 4) evaluate the limitations and usefulness of the interpretation in relation to GEM questions. Data collection for this project was completed during the 2002 field season over two sampling periods: May and July in coordination with GLOBEC research cruises. These data included: lidar (light detecting and ranging using a green laser), SST from an infrared

radiometer, ocean color and index of ChlA from a MicroSAS and derived from RGB video, video imagery from simultaneous RGB and thermal infrared video cameras, and visual sightings. The data derived from these sensors and incorporated into databases from the processed data include: locations, relative size, and density of fish schools and patches of zooplankton, SST, ChlA, location and dynamics of ocean fronts, and location and numbers of marine mammals and seabirds. Also archived was coordinated data from shipboard collections used to validate and interpret airborne derived measurements.

A pilot study, that included airborne remote sensing instrumentation similar to this project, was completed in 2000 and we build upon those results in this study (Brown et al. 2002 a and b). For the 2000 study, we explored and developed better lidar signal processing algorithms. We observed the significant relationship among lidar depth penetration (i.e. green light attenuation), ocean color from airborne video and satellite, and measurements of Chlorophyll a. We mapped size and movement of ephemeral capelin schools that were observed in catches from a ship sampling the same region. We compared estimates of plankton density observed using lidar with plankton densities obtained from ship sampling. We quantified the relationship between acoustic and lidar signal obtained in the same area within a four day period of one another. We compared the spatial distribution and dynamics of lidar and acoustic signals via spatial statistics and recommended a survey design with adaptive sampling statistical methods to best utilized airborne data collection techniques. In this study, we further explored and quantified instrument measurements of Chlorophyll a, plankton, and fish schools expanding on the previously established biological relationships**.**

The results and analysis of our data went beyond the original objectives. We compared indices of productivity among sea lion ecosystems framing the Gulf of Alaska in order to satisfy the original SSLRI study objective. However, because we were never able to obtain ship and satellite tag information from the western (Kodiak) region, we were not able to make a full ecosystem analysis of synthesized data. Instead, we utilized the study data to explore diel patterns of biological distribution in the surface waters within the study regions, to examine the short-term impacts of storms on surface productivity, we documented ship avoidance by key forage prey species, to estimate plankton biomass using airborne remote sensing, and to create a aerial training set for evaluation of airborne photo identification of sea birds. Several of the latter results were pertained directly to the evaluation objectives for the EVOS TC project. We incorporated these results in addition to a direct comparison of ship and airborne plankton sampling within the GEM sampling region in the discussion meant to satisfy the EVOS TC study objectives.

Methods

Instrumentation

The airborne instrument package consisted of 1) a lidar (light detection and ranging) using pulsed green laser light to map subsurface, vertical biological features day and night to a maximum of 50 m, 2) an infrared radiometer to map SST day (similar to

AVHRR satellite data), 3) a low-light level CCD gated camera synchronized with lidar pulses and used to obtain subsurface imagery of biological targets observed with reflected lidar signal, 4) a 3-chip digital color video set up to map ocean color (chlorophyll), ocean fronts, near-surface fish schools, and seabird or mammal aggregations, 5) an infrared digital video to map birds and mammals at night, and in 2002, 6) a MicroSAS used to measure ocean color. The lidar consists of a green laser with a telescope receiver; the system was simple without scanning or imaging capabilities. The laser is a frequency-doubled, Q-switched YAG laser (532 nm wavelength), linearly polarized parallel to the plane of incidence. A negative lens in front of the laser increases the beam divergence.

The lidar system was developed by the NOAA Environmental Research Laboratory in Boulder CO and is fully described in Churnside et al. (1997). The lidar consisted of a laser is mounted next to the receiver telescope and the diverged beam is directed by one mirror to a second mirror mounted to the back of the telescope secondary. The laser beam is directed toward the water coaxial with the telescope. The lidar receiver is a simple refractor that uses a condensing lens to focus the returned signal onto a photomultiplier tube (PMT) detector. An interference filter reduces the contamination of the lidar signal by background light. A rotating polarizer is used to make measurements of the parallel- and cross-polarized returns. The PMT output is passed through a logarithmic amplifier to reduce the dynamic range of the signal. This signal is routed to an analog-to-digital converter (ADC) in a personal computer where it is digitized and saved to the computer hard disk. In other cases, two ADC boards with different gains are used to increase the dynamic range of the receiver. The maximum range and sensitivity of the lidar system is highly dependent on the clarity of the water, but fish can be detected to depths of 30-50 m below the sea surface in clear waters.

The infrared radiometer is a passive instrument that receives energy signals naturally emitted from objects within the instrument's viewing angle. The radiometer antenna for this project was mounted next to the lidar and pointed downward to receive infrared emissions from the ocean surface monitoring thermal emissions near the wavelength of 11 microns. The IR brightness temperature is approximately equal to the physical temperature of the ocean surface. The IR brightness temperature is calibrated in the laboratory prior to and following field data collection. Samples of SST will be spaced at about 50-75 m, depending on aircraft speed, providing much higher resolution than is capable with satellite

For the first time with this lidar system, a gated video camera (low-light level CCD) was tested. This camera allowed "snap-shots" of lidar returns at specified depth levels in 0.1 m increments providing a more detailed examination of optical targets within a given data bin (5-7 m by 0.1 m). This camera is mounted next to and synchronized with the lidar.

During 2001, a Duncan Tech multispectral camera was co-counted with a Raytheon thermal imaging camera on a gimbaled frame that maintained a constant data collection angle. In 2002, the Duncan Tech was replaced with a Hitachi 3-CCD color camera. The swath width of the imagers is altitude and focal length dependent but ranged from 150-

200 m at the 1000 ft altitude typically flown during the surveys for this project. Focal length was set to obtain a ground resolution of a approximately 6 cm.

The MicroSAS, model OCR-507 produced by Satlantic Inc., is a passive light collection device with 7 10 nm or 20 nm bandwidths within the bandwidth range of 400-700 nm. Similar to bandwidths colored by the SeaWiFS and MODIS ocean color satellite instrumentation, these bandwidths are specially designed to provide measurements of ocean color and other optical qualities in ocean surface waters. The instrument collects upwelled and downwelling radiance, that latter used to correct for changes in ocean irradiance due to varying sky conditions.

The lidar system, including the IR radiometer and MicroSAS was controlled by a single lap-top computer. The digital video system (color and thermal) was controlled by a separate lap-top computer. The gated video was controlled independent of the latter two systems. Both system lap-tops had custom software designed by the users for the sole purpose of data acquisition and logging.

Finally, a lap-top computer with navigational software and connected to the aircraft GPS collected flight path information and visual sighting information including log notes were coded in along the path.

Both instrument systems, lidar and video imaging, received geo-coding from the same GPS separate from the aircraft GPS.

Data Acquisition and Format

Five types of data was acquired: 1) lidar system data, 2) digital video imaging footage, 3) MicroSAS ocean color binary files, 4) log files from the navigational software, and 5) video footage from the gated video. From the synchronized lidar system, raster files were created that contained header information followed by a time coded sequence of depth-specific registered optical signal resulting from reflectance of laser light on particles in the water column. Within the header and each line of the file, latitude, longitude, and a GMT time code were coded and each file represented 60 seconds of along path data. Digital video images were recorded on 1 hr digital tapes with a separate tape for color and for thermal data. MicroSAS data was recorded directly to the lap-top computer that controlled the lidar system. The raw MicroSAS files are binary in a proprietary format from Satalantic. Navigation log files were recorded directly to a separate lap-top also in a binary proprietary format particular to the software. Gated video footage was recorded directly to digital tapes and was collected intermittently when conditions were optimal for camera testing and when large sub-surface biological targets (fish and marine mammals) were observed that needed to be identified. The first four data types were collected at all times during aerial surveys.

Processing Methods and Analysis

Processing of lidar signal data is computer intensive. The laser fires 30 times per second and new files are produced every 66 seconds to limit size. Each file is a 2000 (no. of shots) by 1,000 (0.109 m depth intervals) array and represents approximately 5 km of lineal space. The lidar signal decays exponentially with depth in the water. The background slope and median signal profile (of the 2000 profiles) are estimated and subtracted from the shot returns. The relative target is calculated as the ratio of the difference between the individual profile and the slope or median water signal and normalized (to compare with other profiles) by dividing the difference by that same slope or median water signal. The probability or detection is related to the size and depth of targets with decreased sensitivity of smaller objects near attenuation depth (typically 30-50m in Alaskan, non-silty water. This probability will be taken into account (Lo et al. 2000) in expansion of remote sensed data.

In the processing of lidar data, we assume that the backscattered lidar power at depth z can be described by the following equation:

$$S(z) = A[\beta_w + \beta_p(z)]\frac{1}{L^2(z)}\exp(-2\alpha z) + B \qquad (1)$$

where A is a factor that depends on the system parameters and the geometry, b_w is the backscatter coefficient of the water column not including the plankton component, b_p is the backscatter coefficient of the plankton (or other biological feature), L is the optical distance from the aircraft to the measurement depth, a is the lidar attenuation coefficient, and B is the background signal level. B, primarily due to skylight reflected from the surface, was measured using the last 100 samples of each pulse, which is after all of the laser photons have been absorbed. The standard deviation of these same samples were used as an estimate of the receiver noise, s_R, for each pulse.

The quantities Ab_w and a were found for each lidar pulse using Eq. (1) and assuming that: 1) b_w does not vary with depth, 2) b_p is zero at a depth of 2 m, and 3) b_p is zero at the maximum penetration depth z_{max} of each lidar pulse. To calculate z_{max}, we first found the depth at which the signal first went below a value of $10s_R$ above B. The median value of 0.8 times this depth over a data segment of 500 pulses (about 1500 m along the flight track) was used as the estimate of z_{max}. A less restrictive definition would produce a greater value for z_{max}, but the signal would be noisier at the greater depths. The three assumptions allow us to solve the two equations for $S(2)$ and $S(z_{max})$ for the two parameters required. Visual inspection of the lidar data indicated that the assumptions were generally satisfied.

With these quantities in hand, $Ab_p(z)$ can be found from the measured values of $S(z)$. The factor A was known from laboratory calibration measurements, so we could estimate $b_p(z)$ for each pulse. We then applied a threshold to the lidar data to remove small values. That is, we set

$$\beta_p(z) = 0 \ \ if \ \ S(z) \triangleleft TA\beta_w \frac{1}{L^2(z)} \exp(-2\alpha z) + B \tag{2}$$

where T is the threshold value. A value of $T = 1$ means that all positive estimates of $b_p(z)$ were included. In general a value of $T=1$ were used to extract zooplankton information and $T=2$ for fish schools, single large fish or marine mammal targets.

As part of the pilot study, processing software improvements were made to automate some of the steps. The new software, named "fishmar" is written in matlab code and allows easy viewing of files, automation of background signal calculation, and batch processing selection. Bin sizes can be customized as well to address questions with varying spatial scales. Program output can be dumped via the dynamic links to Visual Basic, available in most MS Windows software for further processing, visualization and analysis. Mapping software (GIS) is used to overlay validation and image data. Acoustic density information is used, where available, to scale lidar backscatter values to biomass. Output files can also be created and dumped to the archive in a commonly used format for viewing on acoustic processing software in a form familiar to many oceanographers and fishery biologists. The inclusion of variables from equation 1 within the code are listed in Table 1 and a diagram of how the individual code sections are related is shown in Figure 1. Within the custom software, the log conversion of the signal gain is removed, the range of the signal is corrected to the surface (depth set at 0 here), and the lidar attenuation coefficient (α) is derived as the slope of a linear fit to the attenuation curve. The signal is then normalized:

$$S_N = (S_z - S_0 \exp(-2\alpha z))/S_z \tag{3}$$

where S_N is the normalized signal, S_z is the signal observed at depth z, and S_0 is the background signal derived from the linear fit. The normalized signal is rescaled by fitting a hyperbolic curve to the signal-depth relationship and then subtracting the curve from each value:

$$S_R = S_N - \frac{az}{(b+z)} \tag{4}$$

where S_R is the rescaled signal. Because the normalize signal is a value between 0 and 1, the rescaling allows a better separation between large and small signal values making it easier to detect and compare the variability. Finally, for statistical analysis, the rescaled signal was log transformed to normalize the distribution.

A general treatment of remote sensed and other aerial data is provided in Hunter and Churnside (1995). However, detailed statistical modeling of lidar results was explored by Lo et al. (2000) in relation to aerial census of anchovy off the coast of California. They provided methods 1) to estimate the number of transects needed to minimize abundance estimates, 2) to determine the effects of signal to noise ration (SNR) with attenuation (or depth) on the probability of detection, 3) to estimate the maximum detection depth (z_{max})

8

) based on threshold to noise ratio (TNR) and SNR, 4) to predict the probability of detection based on water mass characteristics, and 5) comparisons of estimates to other methods. The maximum detection depth is a function of the size of the organism or aggregation (i.e. school). For organisms residing partly below the maximum detection depth, acoustic data is combined with lidar data to produce a subsurface correction factor. Lo et al. (2000) suggest the application of line transect theory applied in the vertical along transect plane (rather than horizontal) to estimate abundance, estimation and detection error. For organisms above the maximum detection depth, we can assume 100% detection along the survey track. Finally, Lo et al. recommend the further development of signal processing algorithms to automate the SNR, TNR, z_{max}. Several of these algorithms have been developed under the NPMR pilot study and will be applied to this study. Models developed by Lo et al. to interpret the data collect for this project.

Table 1. Variable equivalence on fishmar software

Variable	FISHMAR	units	description
α	klidar[1]	m^{-1}	lidar attenuation coefficient
B	back[2]	V	background signal (sunlight0ambient light)
Z	i	m	depth
h or L	dd[3]	m	altitude
S_W	back[2]	V	signal from the water only
S	sumsignal[4]	V	integrated signal
S(z)	ifinal2[5]	V	total signal versus depth
	RP[6]	dimensionless	relative perturbation
	SZ[7]	V	lidar signal with exponential model
	dif[8]	dimensionless	(S(z)-SZ)/S(z)
	y[9]	dimensionless	hyperbolic fitting of dif
	res[10]	dimensionless	dif-y
	prof[11]	m	penetration depth

[1]klidar is calculated is calculated using the first 2 m or 50 m in the routine mediana.m and klidar.m respectively. The klidar model assume a lidar attenuation negative exponential with exponent –2.

[2]back is defined as the mean of the last 100 bins in the vertical component. This calculation is done in logamp.m routine. logamp2.m routine is similar to logamp.m but does not consider the background subtraction.

[3]altitude is calculated in routine logamp or logamp2.

[4]sumsignal is equal to log(toti+1) in process.m routine of int egra program. It is res integrated in 50 m vertical and 1 file (2000 shots).

[5]ifinal2 is in logamp2.m routine.

[6]relative perturbation is defined as the signal-median of the signal*signal/signal at 2 m*exp(-klidar*i)

Figure 1. Processing diagram for "fishmar", the matlab processing algorithm.
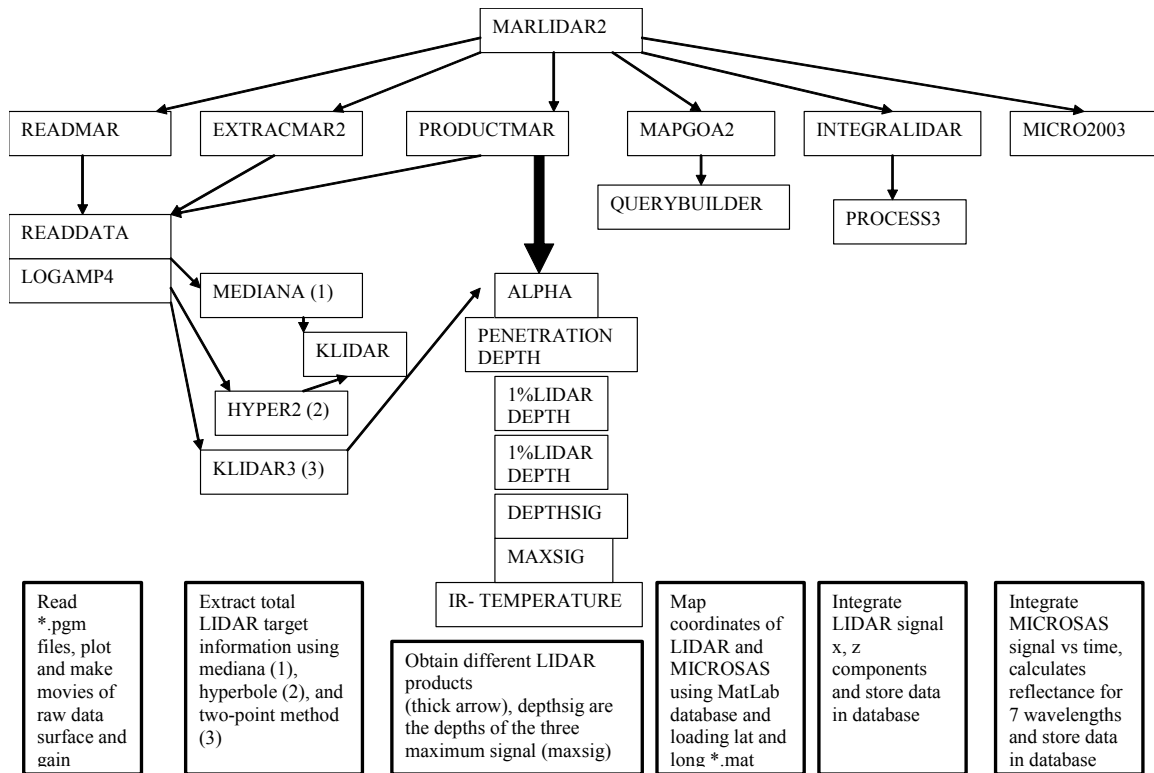
In order to produce ocean color data, the 3 chip digital multispectral camera image data was used. The imager is set up to capture the blue, green, red and near infrared bands. Both an analog output and digital output are recorded. The analog output is recorded onto digital tape at 7.5 fps during the course of the flight. GPS information was recorded onto one of the available sound tracks and later retrieved through post-process to create a dbf file of GPS points along the flight track. The digital signal is captured via a frame grabber at a pre-determined distance along the flight track. In this case, we captured an image every 1000 meters. These images were then batch processed to create a database file of RGB color values for each image at its given location. From this database file the following algorithm was run that gave us a value of green for each image.

$$Vn = G(An)/G(An)+R(An)+B(An)$$

Where: Vn is calculated green value for nth image in the set of images
G is the mean green value of the histogram of An
B is the mean blue value of the histogram of An
R is the mean red value of the histogram of An
An is an area of interest centered on the nth image in order to mask the outer pixels from being included in the calculation. This was done in order to eliminate vignetting effect from the lens and camera port.

The following block diagram shows the relationship of the imaging components for image capture and post-process.
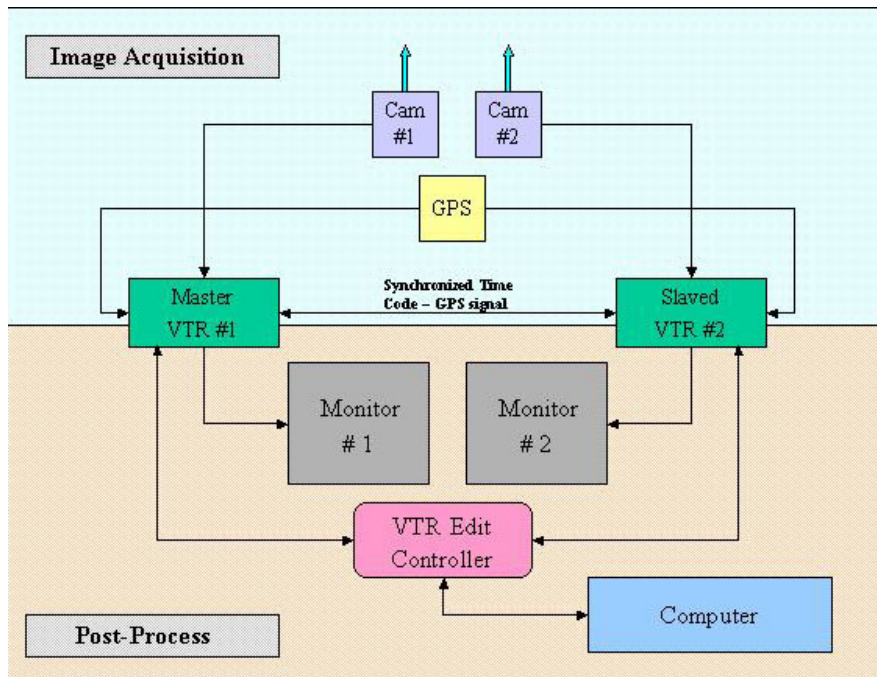
Results and Discussion

Data Collection

During the first study year, 2001, a Beech King Air twin turbine A90 was chartered through Airborne Technologies Inc. (Wasilla, Alaska) and flown from Virginia (point of origin) to Alaska on July 15. The aircraft was modified, prior to leaving Virginia, to provide two separate camera points (36.6 by 40.6 cm and 30.5 by 30.5 cm; Figure 1). The instrument package and mounts were assembled on July 16 and 17th in Wasilla. Rack mounts were constructed for housing the lidar/IR radiometer downlooking through the rear hole and the two imagers downlooking through the front hole (Figure 2). The lidar and imagers were configured to transmit and collect signals at a 10 degree angle in the same direction, to minimize backscatter interference and glare and to provide 100% overlap in data collection. Two GPS systems were mounted with one system used for aircraft navigation and one to integrate with the instruments and provide 1 second geocoding recorded with the digital information. The two GPS systems were synchronized and co-calibrated prior to flights.

Prior to the field seasons, a data collection schedule was devised to maximize airborne–ship synoptic surveys (Table 2). In 2001, a total of 124.7 hours were flown from the period of July 15 to September 23 (Table 3). In 2002, 170.9 hours were flown from the

period of May 10 to September 6 (Table 4). In 2001, during the month of July, we flew 9 surveys, 4 during the day and 5 during the night. For day-night pairs, the same flight path was flown within the 24 hr period in order to do a true diel comparison. Figure 3 shows the flight paths for the day and night surveys; each individual mark in the figure represents a data file approximately 2000 shots long which represents a distance of approximately 4 km, assuming a flight speed of approximately 130 knots. During the month of August, we flew 13 surveys, 7 during the day and 6 at night. As in July, day-night pairs were matched in survey track during a 24 hr period. Figure 4 shows the flight paths and the concentration of effort in the Chiniak Gully (northern concentration) and Barnabas Gully (southern concentration). However, we collected a fair amount of information over the shelf between the two gullies, an area that the ship was not able to work. During the month of September, we flew two daytime surveys in Stephens Passage and Frederick Sound (Figure 5). During the first night flight (Sept. 11-12), we experienced a mechanical problem and returned to the base. However, the terrorist attack resulting in grounding the aircraft and we were not able to complete the September field season as a result. In 2002, flights paths near Kodiak and in Southeast Alaska were similar to 2001, however, during May a GOA broadscale survey was conducted to document variability in biological productivity indices (Figure 6).

Following the end of the 2002 season, a list of ship data requirements was assembled with the intention of developing a database for combined data analysis (Table 5). Highlighted rows indicate data that was actually received after numerous attempts to get the data. Comparisons of airborne, ship and satellite data were completed where possible.

Figure 2. The remote sensing instruments shown mounted in the twin engine aircraft. Inside the aircraft, the dual RGB/CIR imagers controls and monitors are shown in the rack mount (left) with the lens viewing through the camera port in the belly of the aircraft (third from left). The rack mount for the lidar controls and power supply are shown (second from left) with the laser head and receiving telescope mounted behind to send and receive through the rear camera port (right).

Table 2. The initial proposed survey schedule for aerial remote sensing coordination and revised 2002 schedule.

Date	Location	Objective	Ship/Ground Contacts
2001			
July 15-29	Kodiak	Offshore Foraging near Kodiak	Foy
Aug. 8-19	Kodiak	Pre-fishery Offshore/Bays	Hollowed/Wilson
		Nearshore Resources	Foy
Aug. 23-31	Kodiak	Post-fishery Offshore/Bays	Hollowed/Wilson
		Nearshore Resources	Foy
Sept. 4-21	SE	Nearshore/Offshore Foraging	Sigler
2002			
May 7-11	SE	Nearshore/Offshore Foraging	Sigler
May 10-20	Kodiak	Nearshore/Offshore Foraging	Foy
May 22-June 2	SE	Nearshore/Offshore Foraging	Sigler
July 15-29	Kodiak	Offshore Foraging near Kodiak	Foy, Wynne
Aug. 8-19	Kodiak	Pre-fishery Offshore/Bays	Hollowed/Wilson
		Nearshore Resources	Foy
Aug. 21-Sept.1	Kodiak	Post-fishery Offshore/Bays	Hollowed/Wilson
		Nearshore Resources	Foy
Sept. 4-21	SE	Nearshore/Offshore Foraging	Sigler
Revised 2002			
May 10-20	Kodiak	Nearshore/Offshore Foraging	Foy
May 21-June 3	SE	Nearshore/Offshore Foraging	Sigler
July 18-31	Kodiak	Offshore Foraging near Kodiak	Foy, Wynne
Aug. 8-31	Kodiak	Pre- and Post-fishery	
		Offshore/Bays	Hollowed/Wilson
		Nearshore Resources	Foy

Table 3. Actual flight schedule flown during the 2001 field season.

Date	Description	Hobbs	Survey Total	Season Total	Route Flown	Comments
15-Jul	Ferry flight to Alaska	19.8	0.0	19.8	Transit	
16-17,Jul	Install equipment	0.0	0.0	19.8		
18-Jul	Palmer to Kodiak	2.0	2.0	21.8	Transit	Met with Bob Foy
19-Jul	Weather	0.0	2.0	21.8		Fog and rain
20-Jul	Day flight	2.4	4.4	24.2	North & East routes	Fog limited transects
21-Jul	Weather	0.0	4.4	24.2		Fog and rain
22-Jul	Day off	0.0	4.4	24.2		
23-Jul	Day & night flight	8.8	13.2	33.0	North & East routes	
24-Jul	Day off	0.0	13.2	33.0		
25-Jul	Day & night flight	9.8	23.0	42.8	Southeast route	
26-Jul	Day off	0.0	23.0	42.8		
27-Jul	Day off	0.0	23.0	42.8		
28-Jul	Night flight	1.8	24.8	44.6		Weather - cut short Wx
29-Jul	Day & night flight	4.9	29.7	49.5	Southeast route	Day flight cut short Wx
30-Jul	Day flight	4.6	34.3	54.1	Southeast route	
31-Jul	Kodiak to Palmer	1.8	36.1	55.9		Ferry flight
8-Aug	Palmer to Kodiak	2.0	38.1	57.9		Ferry flight
9-Aug	Weather	0.0	38.1	57.9		Evelyn to Kodiak am
10-Aug	Day & night flight	5.6	43.7	63.5	Chiniak	1st day attempt Wx out
11-Aug	Day & night flight	7.0	50.7	70.5	Barnabas	Good weather
12-Aug	Day off	0.0	50.7	70.5		
13-Aug	Day & night flight	4.9	55.6	75.4	Barnabas	Foy aboard, night flight fogged out
14-Aug	Day flight	1.1	56.7	76.5	Chiniak	Partial due to weather
15-Aug	Night flight	2.7	59.4	79.2	Chiniak	Night competion of Chiniak
16-Aug	Day off	0.0	59.4	79.2		
17-Aug	Day off	0.0	59.4	79.2		
18-Aug	Day flight	3.6	63.0	82.8	Chiniak	Day competion of Chiniak
24-Aug	Weather	0.0	63.0	82.8		
25-Aug	Day & night flight	3.5	66.5	86.3	Chiniak	Poor weather both night & day - partial
26-Aug	Day off	0.0	66.5	86.3		
27-Aug	Day off	0.0	66.5	86.3		
28-Aug	Day & night flight	8.8	75.3	95.1	Barnabas	Good surveys both day and night
29-Aug	Day off	0.0	75.3	95.1		
30-Aug	Ferry flight to Juneau	3.4	78.7	98.5		Wayne positioned A/C in Juneau
8-Sep	Day flight	3.4	82.1	101.9	Fredrick Sound	1st Juneau flight - good weather
9-Sep	Day off	0.0	82.1	101.9		
10-Sep	Day off	0.0	82.1	101.9		
11-Sep	Day flight	3.4	85.5	105.3	Fredrick Sound	2nd Juneau flight
12-Sep	Night flight	1.3	86.8	106.6	Fredrick Sound	Lidar equipment failure
13-Sep	Day off	0.0	86.8	106.6		Airport closed due to attack
14-Sep			86.8	106.6		Return aircraft to Palmer
23-Sep	Ferry flight to Virginia	18.1		124.7		

Table 4. Actual flight schedule flown during the 2002 field season.

AST Date	Survey Objective and Route Name	Day/Night	Hobbs	Season Total
10-May	Ferry to Kodiak		1.6	1.6
11-May	Kodiak -MACH - Foy	D	3.5	5.1
11-May	Kodiak -MACH - Foy	N	2.4	7.5
12-May	Kodiak -MACH - Foy	D	3.3	10.8
12-May	Kodiak -MACH - Foy	N	2.0	12.8
13-May	GOA X-Shelf PWS Zoop*	D	0.0	12.8
16-May	Aleutian Prod. Front - Hunt	D	3.4	16.2
17-May	Aleutian Prod. Front - Hunt	D	3.7	19.9
18-May	Kodiak LICH - Foy	D	3.3	23.2
18-May	Kodiak LICH - Foy	N	3.3	26.5
20-May	Kokiak LICH	N	3.6	30.1
21-May	Kodiak LICH - Foy-Buck	D	4.9	35.0
22-May	Kodiak LICH - Foy; X-Shelf-Homer	D	4.1	39.1
23-May	Homer to N. LICH area	D	3.4	42.5
24-May	Kodiak LICH - Foy and ferry	D	3.3	45.8
24-May	Ferry to Juneau-BS GOA	D	3.4	49.2
25-May	SE AK-Frederick Sound and ferry	D	3.8	53.0
25-May	SE AK-Frederick Sound	N	3.7	56.7
26-May	SE AK-Frederick Sound	D	3.7	60.4
26-May	SE AK-Frederick Sound		0.7	61.1
31-May	Southeast - LICH - Sigler	D	1.5	62.6
2-Jun	Southeast - LICH - Sigler	D	0.0	62.6
3-Jun	Ferry to Wasilla - PWS survey	D	0.0	62.6
13-Jul	Ferry to Kodiak	D	0.0	62.6
16-Jul	Kodiak -MACH - Foy	D	4.1	66.7
16-Jul	Kodiak -MACH - Foy	N	2.4	69.1
25-Jul	EVOS - Seward Line*	D	3.1	72.2
26-Jul	Kodiak LICH - Foy	D	2.7	74.9
26-Jul	Kodiak LICH - Foy & Seward Line	N	3.7	78.6
27-Jul	Kodiak LICH - Foy	D	2.6	81.2
27-Jul	Kodiak LICH - Foy	N	4.8	86.0
28-Jul	Kodiak LICH - Foy	D	4.7	90.7
28-Jul	Kodiak LICH - Foy	N	3.6	94.3
29-Jul	Chiswell - TS Seward Line*	D	4.0	98.3
29-Jul	Kodiak LICH - Foy	N	3.1	101.4
31-Jul	Seward - Weathered out*		1.2	102.6
1-Aug	Seward - Early Eve. - Inside Fog*	D	3.7	106.3
2-Aug	Ferry to Wasilla*		0.0	106.3
10-Aug	Ferry to Kodiak*		0.0	106.3
11-Aug	Five-Bay Broadscale - Foy	D	4.1	110.4
12-Aug	Five-Bay Broadscale - Foy	D	4.1	114.5
13-Aug	Five-Bay Broadscale - Foy	D	4.2	118.7
14-Aug	Chiniak-Barnabas - Wilson	D	4.9	123.6
14-Aug	Chiniak-Barnabas - Wilson	N	1.1	124.7

Table 4. Continued.

AST Date	Survey Objective and Route Name	Day/Night	Hobbs	Season Total
16-Aug	Chiniak-Barnabas - Wilson	D	4.9	129.6
16-Aug	Chiniak-Barnabas - Wilson	N	4.6	134.2
17-Aug	Kodiak -MACH - Foy	D	2.9	137.1
17-Aug	Kodiak -MACH - Foy	N	2.9	140.0
20-Aug	Aborted Chin.-Barn.	D	0.5	140.5
20-Aug	Chiniak-Barnabas - Wilson-Ran into Fog	N	1.9	142.4
22-Aug	Chiniak-Barnabas - Wilson	D	5.0	147.4
22-Aug	Chiniak-Barnabas - Wilson	N	4.3	151.7
27-Aug	Boat Avoidance Test - Wilson	N	1.3	153.0
28-Aug	Chiniak-Barnabas - Wilson	D	5.1	158.1
28-Aug	Chiniak-Barnabas - Wilson	N	3.8	161.9
1-Sep	Chiniak-Barnabas - Wilson	D	0.0	170.4
2-Sep	Chiniak-Barnabas - Wilson	N	0.0	170.4
4-Sep	Chiniak-Barnabas - Wilson; aborted		0.5	170.9
6-Sep	Ferry Home		0.0	170.9

* These survey hours, and associated time processing the data, were charged to other integrated projects (PWS OSRI, EVOS GEM)

Figure 3. Day (yellow) and night (red) surveys flown in Kodiak over the period July 20 to 30, 2001. These surveys were conducted in coordination with Bob Foy's broadscale ship survey over eastern Kodiak.

July Flights - Broadscale Survey
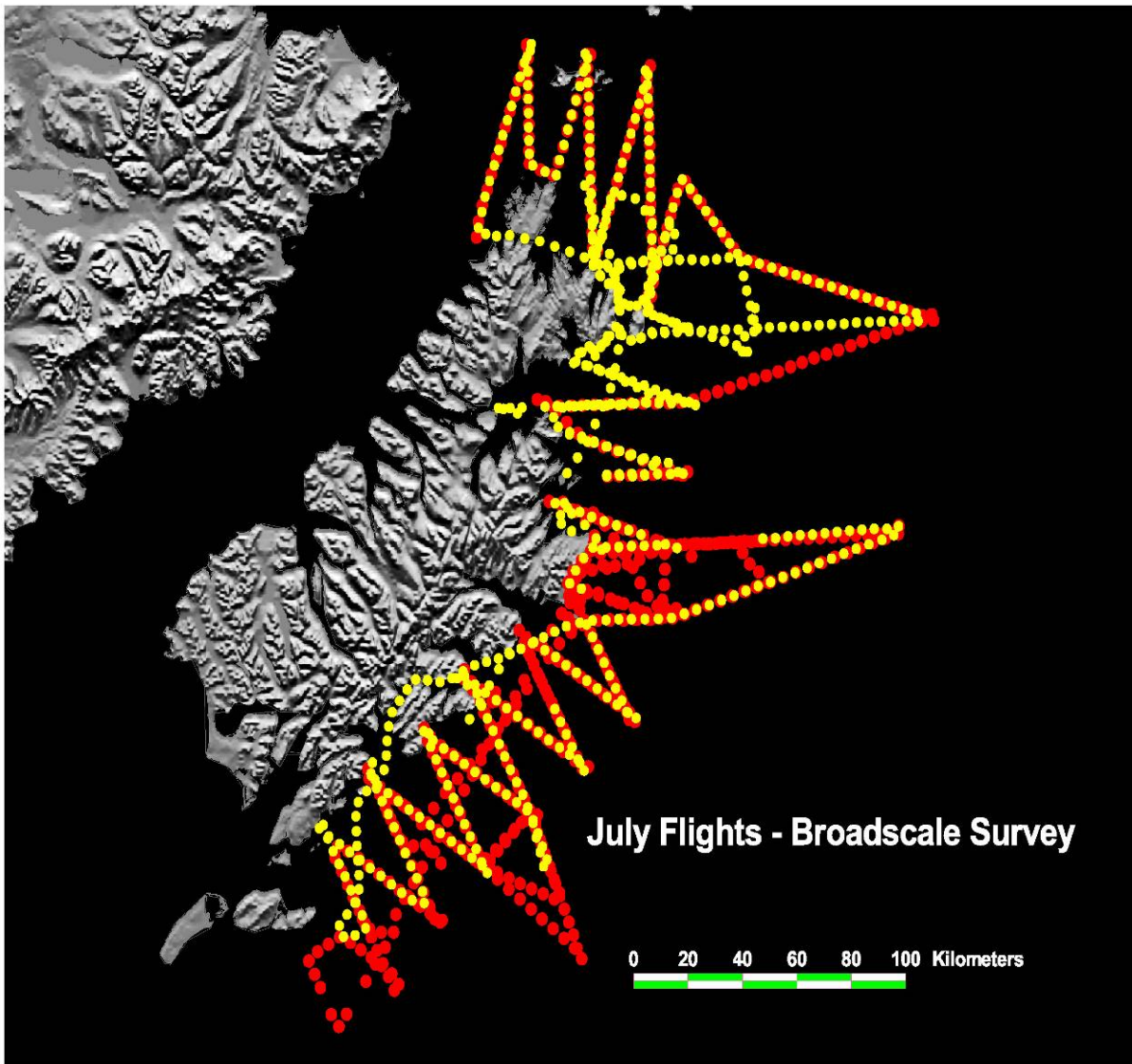
Figure 4. Day (yellow) and night (red) surveys flown over Chiniak and Barnabas Gullies off Eastern Kodiak Island from August 10 to 28, 2001 in coordination with the pre- and post-pollock fishery ship surveys conducted by Chris Wilson and Anne Hollowed.

August Flights - Pre-, Post-Fishery Surveys
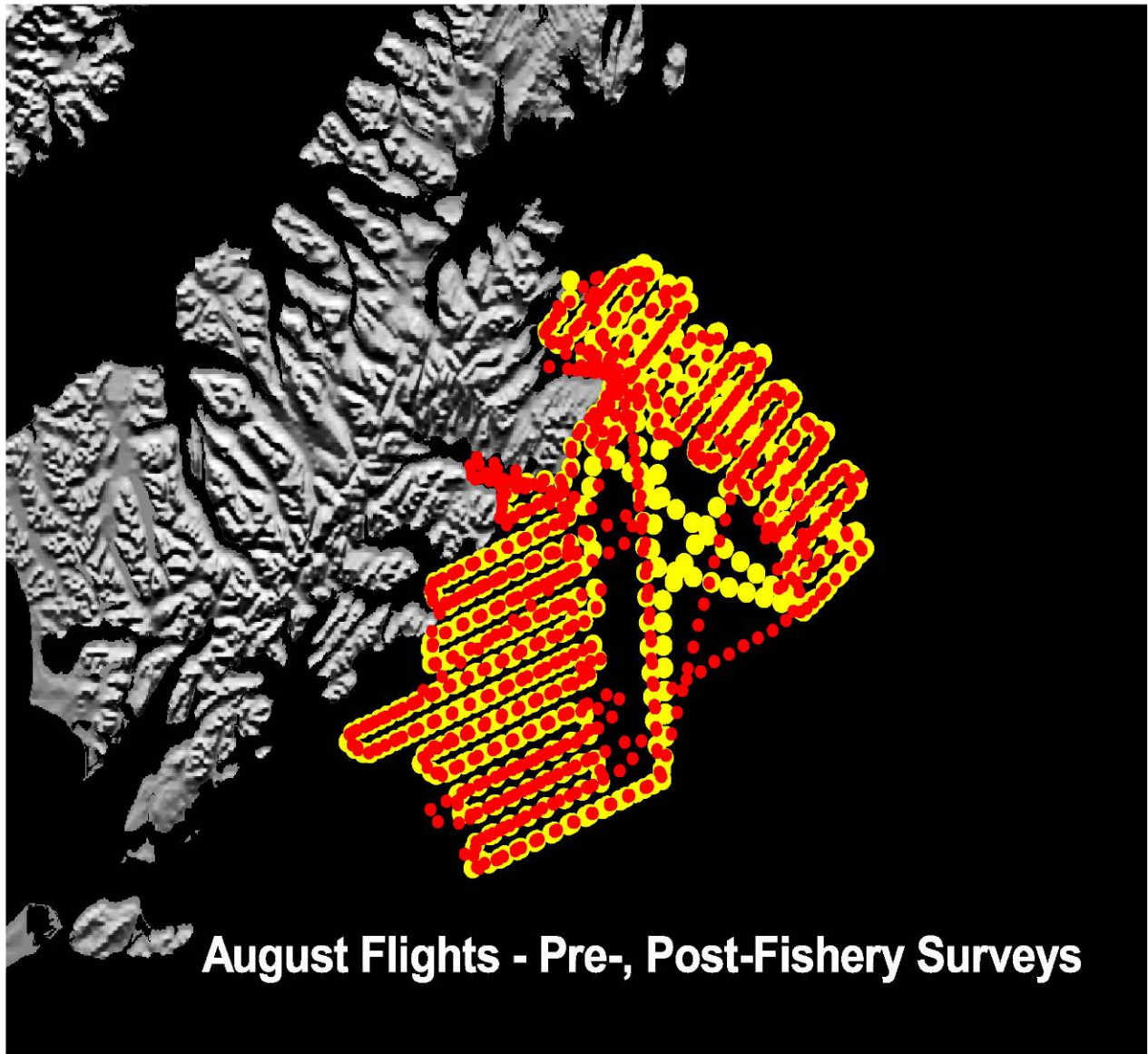
Figure 5. Day surveys flown over northern Southeast Alaska in Frederick Sound September 8-11, 2001 in coordination with the broadscale ship-board surveys conducted by Mike Sigler.

Sept. Flights - SE AK Survey

0   20   40   60   80   100 Kilometers
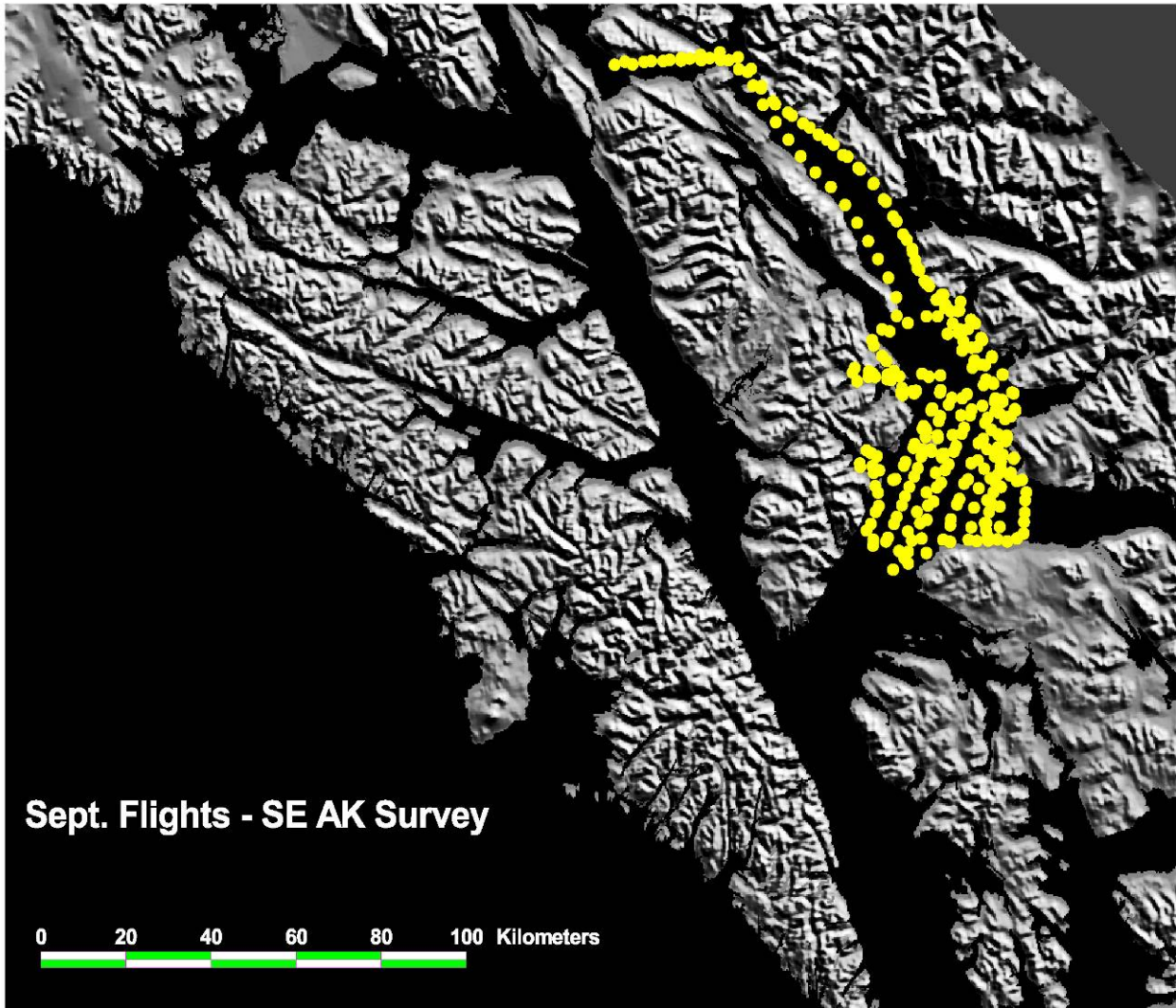
Figure 6. Location of aerial surveys in May, 2002 and allocation of data among ocean habitats.
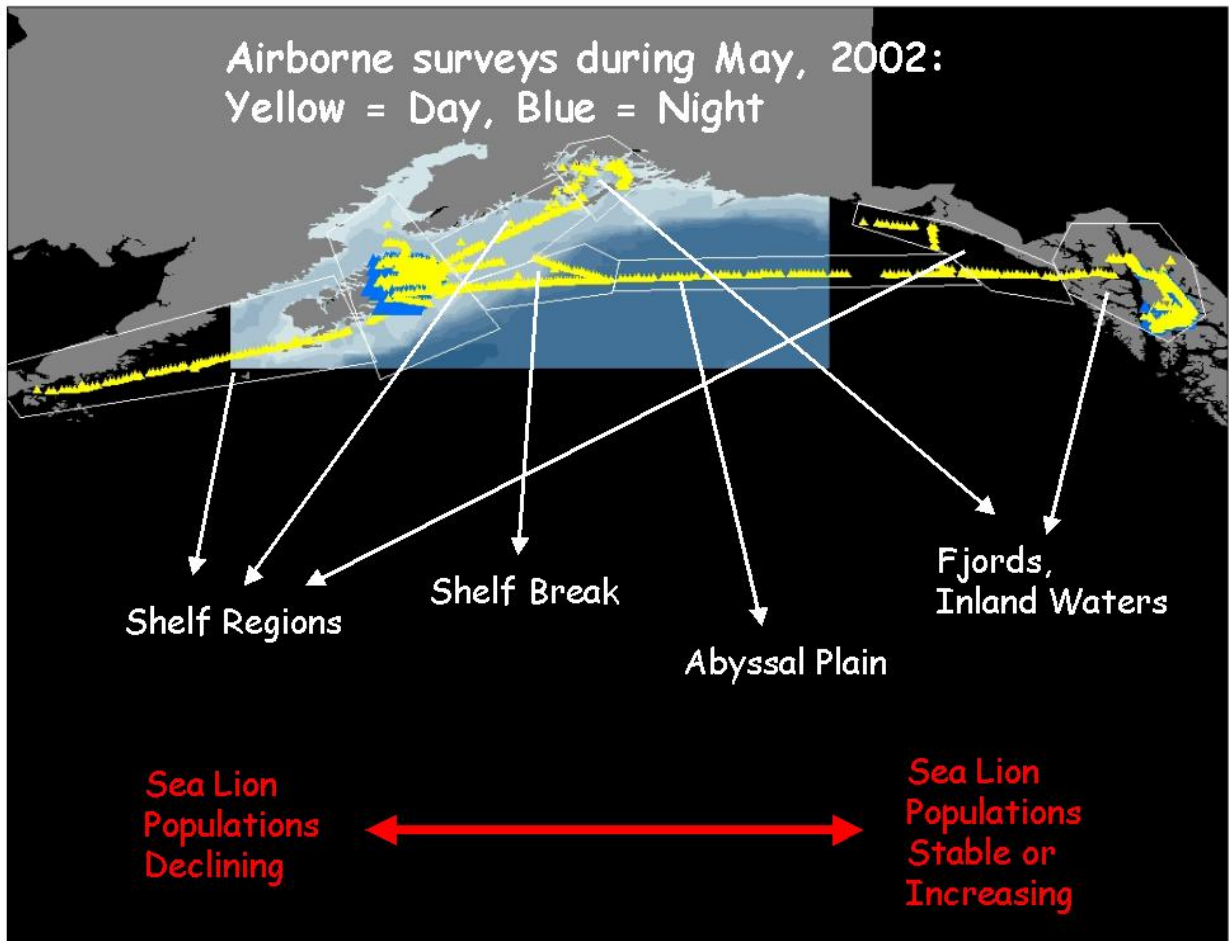
Table 5. Data components of the database that were requested for this project are listed including year collected, general location and project, data type, and contact person (SSL data is being combined with 2000 data collected outside the scope of this project but relevant in analysis). Highlighted rows indicate data that was received.

Year	Month	Location	Project	Type	Contact Person
2000 & 2002	May & July	N GOA(PWS to outer shelf)	GLOBEC	Zoop (Abundance and Species Composition); Mocness Catches; Acoustics.	Ken Coyle, IMS
2000	July	SE AK (fjords)	NMFS Juv. Salmon Surveys	Zoop. (Abundance and Species), CTD	Molly Sturdevant, ABL
2000 & 2002	May & July	N GOA	GLOBEC	Chl A, PAR, and Fluorescence	Dean Stockwell, IMS
"	"	N GOA (shelf)	OCC	Fluorescence CTD, Thermo-Salinograph	Jack Helle, ABL; Ned Cokelet, PMEL
"	"	N GOA	GLOBEC	Fish cathces	Lew Haldorson, UAF, Juneau
"	"	N GOA	GLOBEC	Thermo-Salinograph, CTD	Seth Danielson, IMS
"	"	N GOA (point)	SALMON	GAK 4 Buoy TS profiles, Fluorescence	Hank Statscewich, IMS
2000-2002	May, July, Aug., Sept.	N GOA & Kodiak (points)	PMEL	Buoy data; TS profiles, Fluorescence	Phyllis Stebeno, PMEL
2001-2002	"	Kodiak (inner shelf)	GAP, SSLRI	Acoustic files, net catches, CTD, Fluorescence, Zoop. SV and species comp.	Bob Foy, FITC
2002	May	Kodiak-(outer shelf)	AFSC FOCI	Zoop. species comp, phytoplankton, CTD-PAR, ChlA, sediments	Jeff Napp, AFSC
2001-2002	August	Kodiak (inner shelf)	SLLRI	Acoustic files, net catches (fish), CTD, thermo-salinograph, ChlA, currents, sediments	Chris Wilson, AFSC & Phyllis Stebeno, PMEL
2000-2002	May, July, Aug., Sept.	Kodiak, AP, NGOA	?	SeaWiFS and AVHRR imagery	Sigrid Salo, PMEL
2000-2002	May & July	NGOA	GLOBEC	SeaWiFS imagery	Andrew Thomas, U Maine
2001-20021	May * Sept.	SE AK	SLLRI	Acoustic files, fish catches, CTD	Mike Sigler, ABL
2000-2002	May, July, Aug. Sept.	All Regions	EVOS GEM & SSLRI	lidar profiles, IR SST, RGB imagery, Thermal IR imagery, Microsas (ocean color)	This project
2001-2002	"	Kodiak	GAP	Sea bird validations	Loren Buck, FITC
2001-2002	"	Kodiak	GAP	Marine Mammal Validations	Kate Wynn and grad. student, FITC
2000 & 2002	May & July	N GOA	GLOBEC	Sea bird validations	Bob Day, ABR

Table 5. Continued; Key

Abbreviations:
ABL – Auke Bay Lab, NMFS NOAA, Juneau
ABR – Alaska Biological Research (consulting firm), Fairbanks
AFSC – Alaska Fishery Science Center, NMFS NOAA, Seattle
AP – Alaska Peninsula
FITC – Fishery Industrial Technology Center, UAF, Kodiak
GLOBEC – Global Oceans Ecosystem Dynamics program, N GOA region, IMS UAF Fairbanks
IMS – Institute of Marine Science, UAF, Fairbanks
N GOA – Northern Gulf of Alaska
OCC – Ocean Carrying Capacity project, ABL, Juneau
PMEL – Pacific Marine Environmental Lab, OAS NOAA, Seattle
PWS – Prince William Sound
SALMON – Sea-Air Land Modeling and Observing Network, IMS UAF, Fairbanks
SE AK – Southeast Alaska

Indices of Production Across the Gulf of Alaska

These results were initially reported at the 53rd Arctic Science Conference of the American Association for the Advancement of Science (AAAS) meeting in September, 2002. The title of that talk was:

"Spatial Variability in Ocean Productivity and SST Across the GOA Basin and Shelves", Brown, Montes and Churnside.

A key hypothesis for the suite of Steller sea lion studies related to food limitation. If food is a factor limiting the western populations as compared to the eastern population of GOA sea lions, than we might expect to see more food resources available in the east. A proxy for available sea lion prey may be primary and secondary production that limits fish and invertebrates feeding on zooplankton along with the piscivorous fishes, many of which are targeted by sea lions. We used the broad scale survey data from May, 2002, a time when biological production in the surface is at a peak, to test the hypothesis that spatial variability. The specific question we sought to answer was:

Is the spatial variability in GOA Steller sea lion population dynamics due to variability in food availability?

Given, the western population (Aleutian Chain) is low and decreasing, the Kodiak population is low, but stable, the PWS population is low with unknown stability, and the SE Alaska population is increasing, our hypothesis was:

H_0: Food resources are not limiting for sea lions in the GOA as evidenced by the lack of a gradient in ocean biological standing stock from the west to the east.

To test the hypothesis, our objective was to:

Determine if spatial variability in observed ocean productivity provides an explanation for the variability observed in sea lion population dynamics by 1) developing an index of biological standing stocks, in the upper 50 m, from airborne lidar and ocean color observations linked to airborne SST measurements, 2) linking that data with satellite imagery (SST & ocean color), and 3) performing statistical tests for testing including cluster analysis, multiple regressions, and ANOVAs. Using this information, we were also able to define the spatial variability in ocean conditions and biological standing stock across the GOA during a single time period.

Within the period of May 11-25, 2002, surveys were flown across the GOA region during the day and day-night survey pairs were conducted over eastern Kodiak and in northern SE Alaska in coordination with process studies (Figure 6). Therefore, we used only the daytime values for this analysis. We categorized the survey regions into 8 zones representing four oceanic habitat types: 1) shelf regions, 2) shelf break, 3) open ocean (over the abyssal plain), and 4) fjords or inland waters. The statistical analysis was based on differences or similarities among variables derived within these zones.

The index of standing stocks in surface waters (shallower than 50 m), used to test the hypothesis, were derived and interpreted in the context of other oceanographic data. The indices were derived from two sources: 1) light penetration depth or attenuation coefficient, and 2) integrated lidar signal return from upper 50 m. From past work, we believe that the light penetration depth is a proxy for primary production. There is a relationship between the lidar attenuation coefficient or penetration depth and a green index derived from the green broadband of the RGB imager (Figure 7; Brown et al. 2002). Furthermore, the green index (G) is correlated with SeaWiFS derived values of Chl a (Figure 8). Also from past work, we found a relationship between zooplankton settled volumes and the integrated lidar signal in a 1 km block around the sampled site (Brown et al. 2002). Therefore, we feel justified in using the two sources of data to estimate an index of standing stock representing both primary and secondary production. After deriving the indices, we related the two source values to SST, collected at the same time by the infrared radiometer aboard the aircraft. We also derived the maximum signal observed at a given depth (from 0.1 m depth bins) and the depth at which the maximum signal occurred. The maximum signal exhibits a larger dynamic range than the mean signal values and therefore may better show differences between regions. Variation in the depth of the maximum signal has implications on food availability to surface feeders that, in turn, may represent forage quality for sea lions. Finally, we compared the SST observed from aircraft with SST observed from satellites (AVHRR) during the same time frame.

Figure 7. The correlation between the lidar attenuation coefficient (α) and the green index (G), derived as the spectral intensity from the green band of an RGB imager normalized over the total intensity from all three bands.
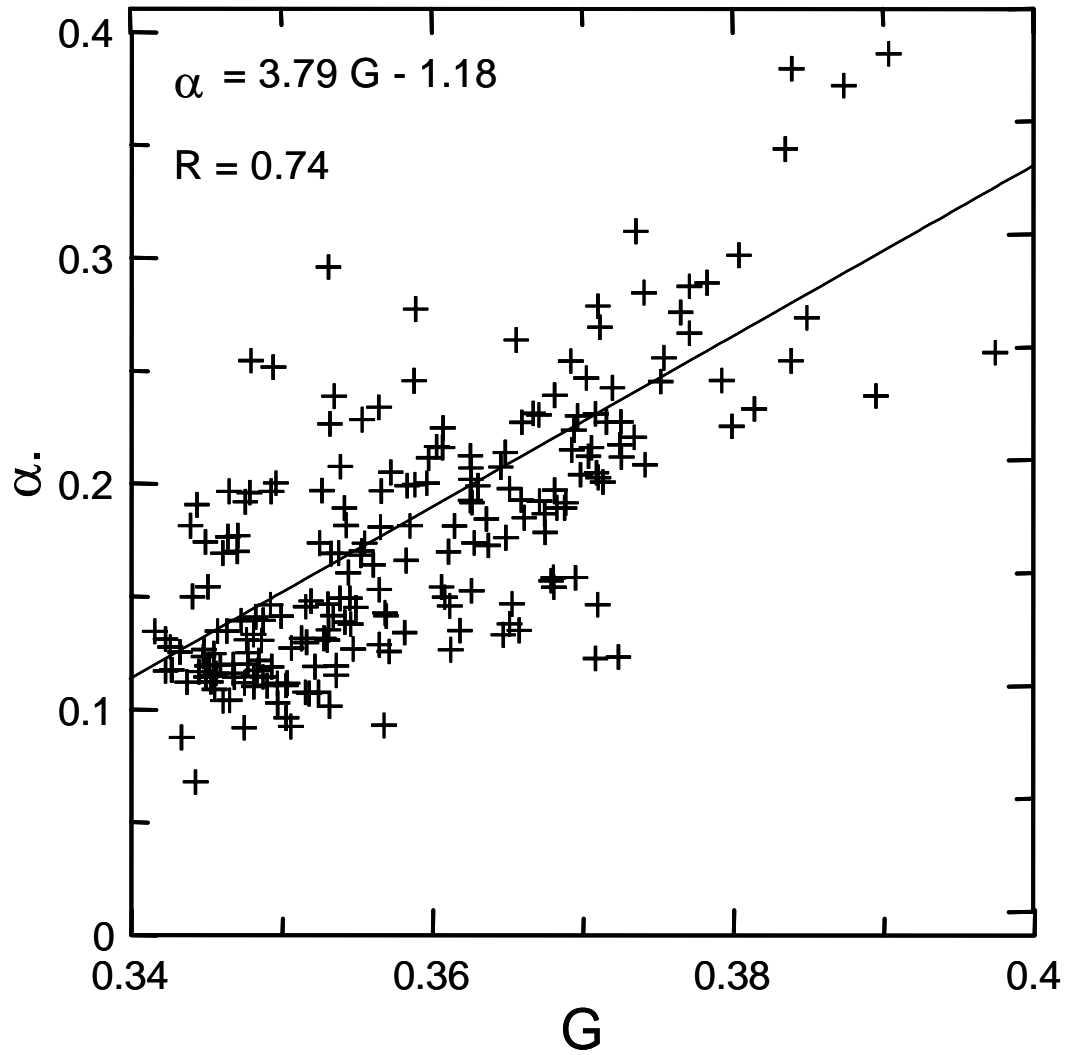
Figure 8. The green index (G) and true color images from an RGB imager in relationship to SeaWiFS derived Chl a values collected over the same time period. The right image is bluer and is associated with less productive waters immediately south of Prince William Sound as compared to the left greener image associated with higher productivity waters of Cook Inlet.
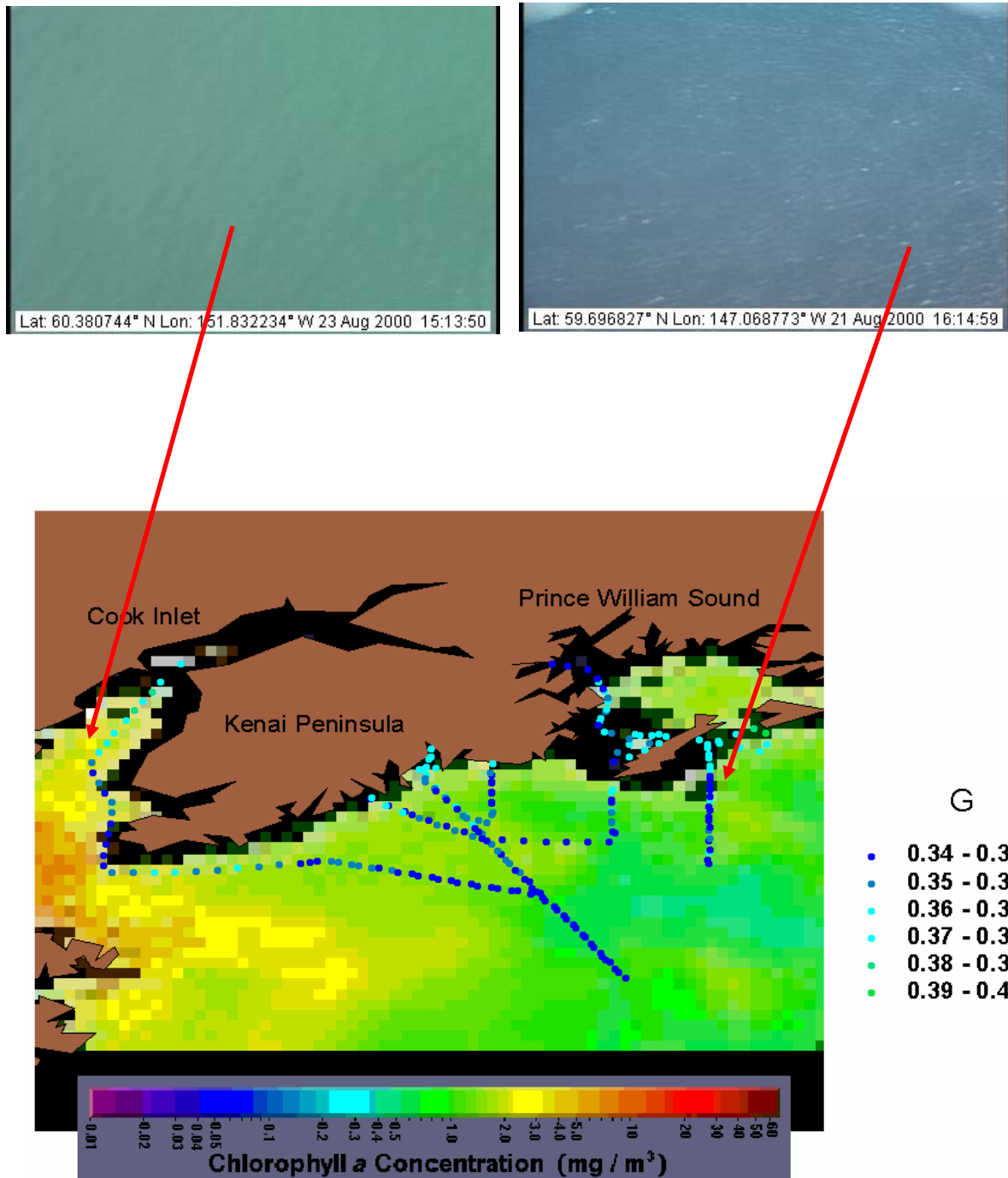
The penetration depth and attenuation coefficient did not co-vary in the same way as found in previous studies and there were variations in both across regions. In the previous study (Brown et al. 2002), penetration depth was estimated as the depth at which a threshold signal occurred and was found to be negatively correlated with the attenuation coefficient. In this study, the penetration depth was estimated as the depth where the signal turned into pure noise. This is generally deeper than a given threshold and was not related to the slope of the attenuation curve (i.e. attenuation coefficient). Penetration depths (Figure 9 and 10) were deeper over the Aleutian, E. Kodiak, and eastern GOA shelves and eastern shelf break. They were shallower over the western shelf break, central shelves (Outer Kenai) and within PWS and SE Alaska fjords; this could have been related to more suspended solids (silt) in these regions compared to the others. Penetration depths were most variable over the eastern shelf and shelf break (zone 7; Figure 9 and 10). Similarly, attenuation coefficients were highest over the Aleutian shelf and eastern shelf/shelf break, but also in SE Alaska. They were lowest and the least variable over the Outer Kenai shelf, the western shelf break and open ocean. They were most variable over the eastern shelf /shelf break. High attenuation coefficients are related to greener waters with higher phytoplankton concentrations, indicating that the western GOA shelves and fjords may have overall higher primary production despite lack of penetration depth from silt. From MANOVA results, the Wilk's Lambda and Rao's R test showed that all zones differed significantly ($p < 0.01$) from one another over all variables. I performed Tukey's pair wise Ad Hoc test for unequal variance for both variables and found a varying degree of significant similarities between pairs of zones. Clustering (not significantly different from one another) occurred among zones 3-5, 6-7, 1-7, but zone 8 (SE Alaska) stood out as significantly different from all groups (Figure 10). In the paired comparisons, penetration depth was more sensitive to detection of differences among regions with 41 out of 46 or 89.1% possible comparisons significant versus the attenuation coefficient at 46.4% significant comparisons.

The integrated and maximum signal co-varied with higher overall variability in the maximum signal, compared to integrated, as predicted. Signal was lowest in SE Alaska and highest on the Outer Kenai shelf, over open ocean, and over the eastern shelf / shelf break (Figures 10 and 11). PWS fjords had moderate signal values but the highest variability. These data indicate that standing stocks of large zooplankton and fish, which affect signal return most profoundly, were highest over the central portions of the GOA, including shelves and open ocean, than in the fjords or western GOA. The overall MANOVA test resulted in the same significant overall difference among zones for these two variables ($p < 0.00$) and the clustering resulting from the Tukey's test was complimentary. For the signal levels, the central zones (3-7 clustered) as did the western zones (1-2), but as found with attenuation and penetration, zone 8 stood on its own (Figure 10). As would be expected given the higher variability, maximum signal was a more sensitive measure of differences among regions with 73.9% significant pair wise comparisons compared to 52.2% for the integrated signal.

The depth of maximum signal did not vary much across regions versus the SST (airborne) that showed a steadily increasing trend from west to east (Figures 9, 12 and 13). The SST did not appear to co-vary with any of the other variables. As expected,

depth of maximum signal was a poor discriminator of differences among regions (34.8% significant pair wise comparisons; P < 0.01) versus SST (78.3% significant comparisons). Depth of maximum signal only separated zone 8 (SE Alaska) out as significantly different from the rest while SST indicated three main clusterings: Zones 1& 4 (Aleutian Shelf and PWS) overlapping with cluster Zone 1-2-3 (Aleutians Shelf, E. Kodiak and Outer Kenai), and Zones 5-8 (everything east except PWS). These two variables did not appear to co-vary with the others. The two regions with the highest variability (E. Kodiak and SE fjords (Figure 13), were also the regions most intensively and variation in depth of maximum signal was much greater in SE than around Kodiak.

The final examination of individual variables was SST derived from airborne instruments versus satellite. We derived an 8-day composite of available, 80% cloud-free AVHRR imagery overlapping the sampling period (May 11 to 31) and determined the mean SST at each pixel (Figure 12). We then sampled only image pixels directly touching locations along the flight path. There was very correlation between the sampled AVHRR image pixels and the airborne SST whether we compared them zone-wise or overall (Figure 13). Even when the measurements occurred on the same day and the satellite mean represented that daily value (i.e. no lag in measurement), the correlation was not significant. In general the distribution of airborne SST measurements was much less variable than AVHRR SST (Figure 13). We have more work to do on this comparison, since we would like to sub-sample for measurements taken within hours (versus days) of one another. However, if the lack of correlation holds, it may indicate a serious problem using AVHRR data to accurately represent actual SST values on the surface. We know that the surface values are extremely variable on very short time scales.

The final part of this preliminary analysis was to use all variables (except AVHRR SST) for evidence of regional clustering and to test the hypothesis. Clustering was completed by two methods: 1) summing up the number of significant pair wise (between zones) tests among all variables, and 2) a K-means cluster analysis using Euclidean distance (Figure 14). The first method revealed three possible groups: 1) zones 6-7 (GOA and eastern shelf) showing the most similarities (0 significant pair wise tests), 2) overlapping zone containing regions 4-6 (PWS, western shelf break and central GOA; 1 each), and 3) zone 8 (SE Alaska) by itself with the most significant numbers of tests among all variables tested. The K-means cluster analysis was performed first with eight clusters, then four, then three. For the 8-cluster analysis (not shown), the only obvious group, by examining grouping patterns, was zones 6-7 (GOA and eastern shelf/break) When reduced to four clusters (Figure 18), once again zones 6 and 7 clustered along with zones 3 and 4 while the other zones appeared to stand unique. The reduction to 3 clusters did not change the groupings. The conclusion was that the Aleutian (zone 1) and E. Kodiak shelf (2) were unique from one another as well as from the open ocean-eastern shelf region (6-7), the western GOA shelf and PWS (zones 3-4), the western shelf break (5), and SE Alaska fjords (8). The east and west GOA shelves and shelf breaks differed and the two fjord areas differed. Only zones 6-7 could be reliable grouped according to the variables used.

In testing the hypothesis, low attenuation rates (primary standing stock proxy) appeared to cluster with high integrated and maximum signal (fish and zooplankton), possibly

indicating a grazing affect. Assuming the combination (low attenuation and high signal) represents increased food availability, than the order of regions in terms of food (from high to low) was interpreted as the following: 1) open ocean – eastern shelf / shelf break and the western shelf or Outer Kenai, 2) the western shelf break (5), 3) PWS, 4) the Aleutian and E. Kodiak shelves, and 5) SE Alaska. Given SE Alaska is the only region with a stable and increasing sea lion population yet has the lowest food availability score and given that the western shelf and break (associated with a depressed sea lion population) has relatively high food availability, these data do not lead to a rejection of the null hypothesis (i.e. food is not a problem). However, the Aleutian shelf had the second to lowest score and it is associated with a depressed and declining population. This finding alone would lead to a rejection of the null hypothesis, but in combination with the other results, no conclusion can be determined unequivocally. Either our data is not a proxy for food availability for apex species or the food problem is not evident in May. We will continue to finalize this analysis by addition the other month and year strata and by combined these results with shipboard data.

Figure 9. The penetration depth (top) and depth of maximum signal (bottom) for each 4 km data point plotted over the 8 regions with greener values representing shallower penetration or maximum signal location. Zone 1 = Aleutian Shelf, 2 = Eastern Kodiak Shelf, 3 = Outer Kenai Shelf, 4 = Prince William Sound Fjords, 5 = Western Shelf Break, 6 = Open Ocean, 7 = Eastern Shelf /Shelf Break, 8 = SE Fjords.
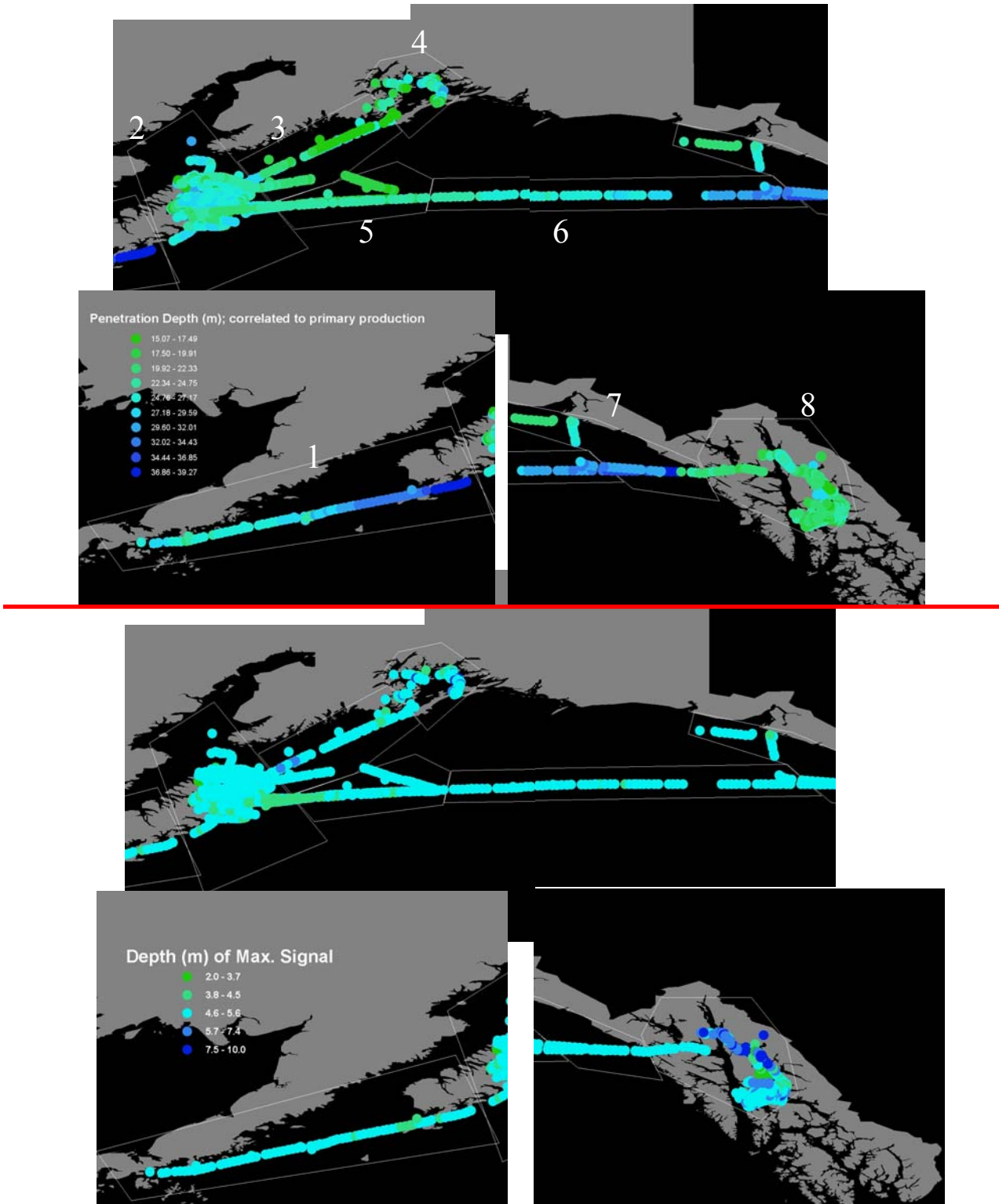
Figure 10. The distribution of penetration depth and lidar attenuation coefficient shows that they co-vary and that primary production standing stock is higher is zones 1, 7 and 8 than the others (using lidar attenuation coefficient).
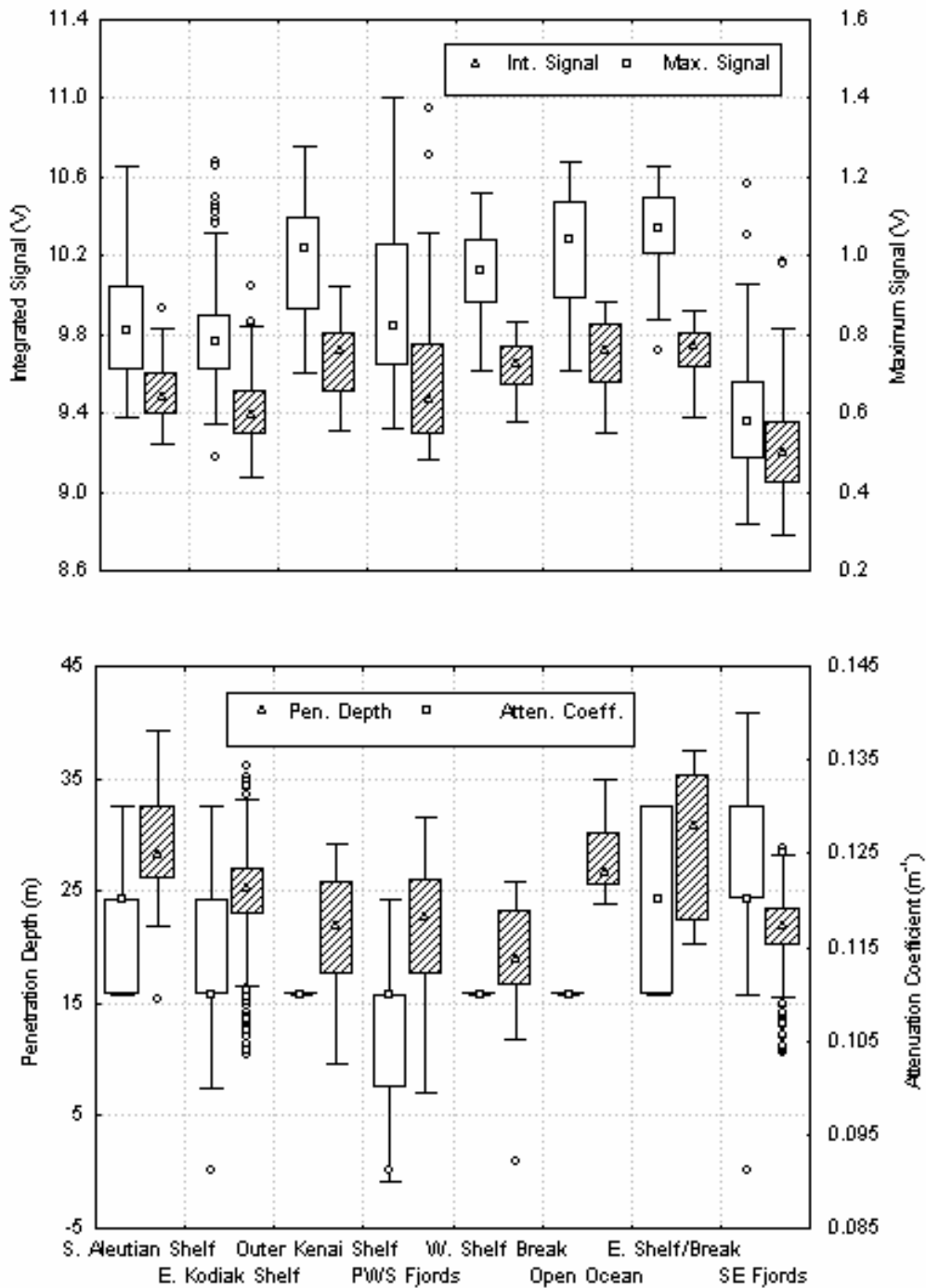
Figure 11. Integrated signal (to 50 m) and maximum signal at depth over the 8 zones.
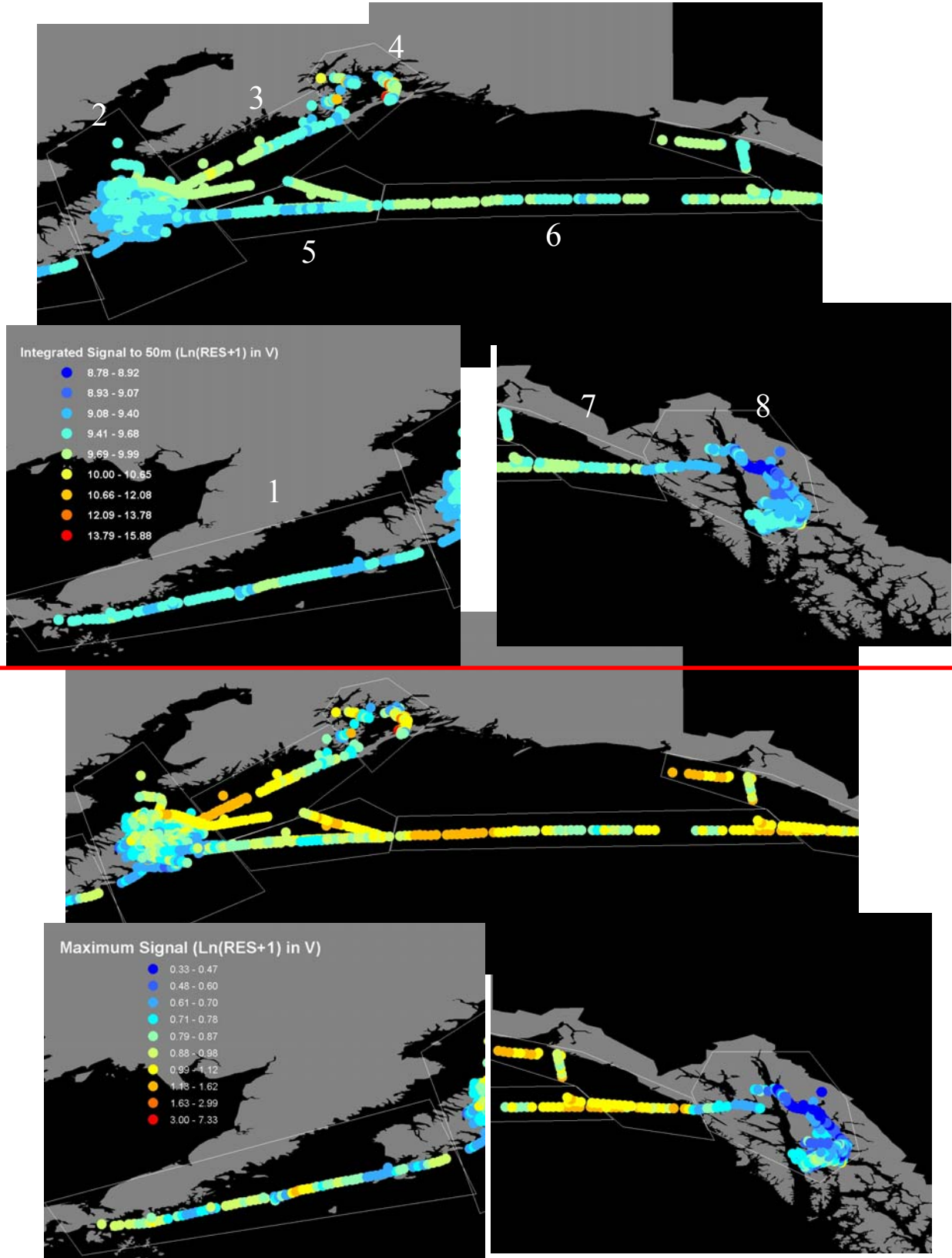
Figure 12. Satellite derived SST from AVHRR (top) with red being the hottest (about 12 degree C maximum and –3 C minimum) and SST from airborne measurements.
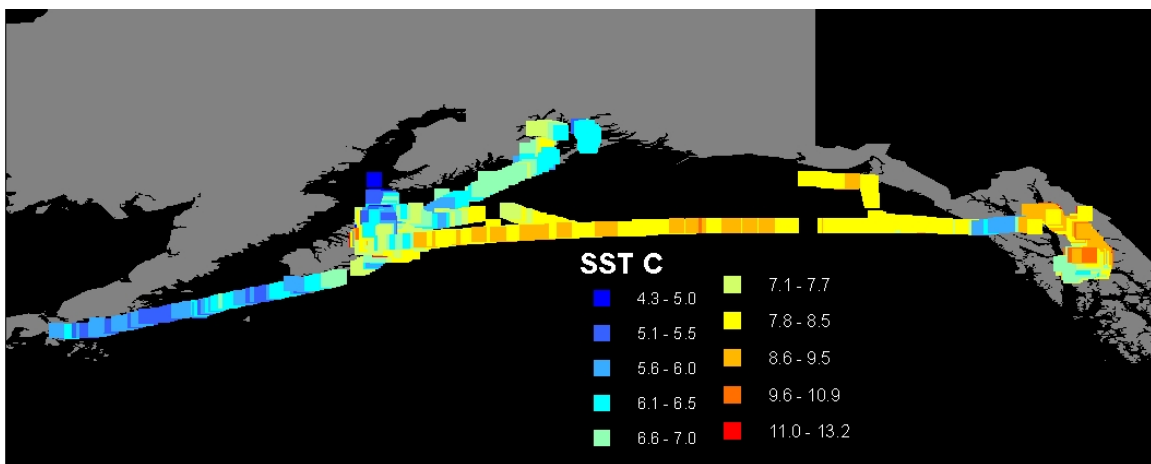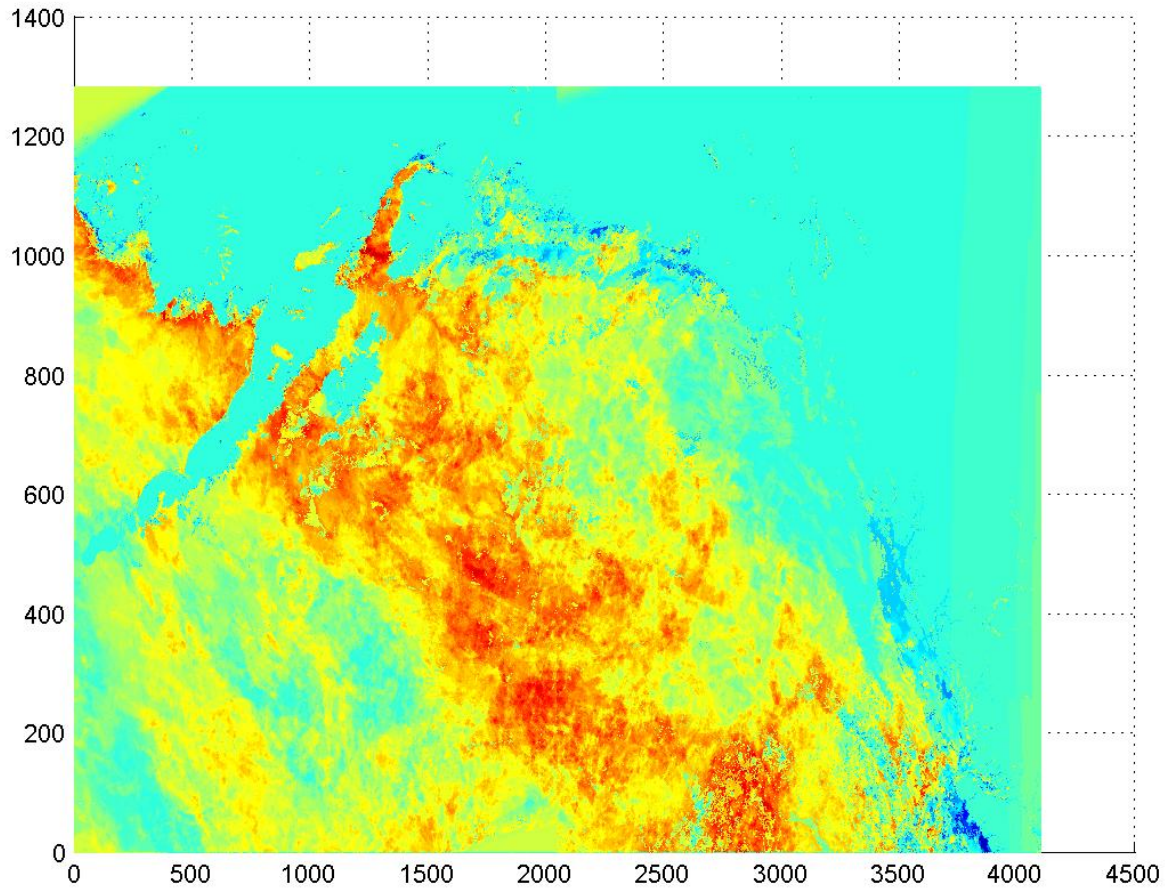
Figure 13. Although SST (airborne derived) showed an increasing trend from west to east (top), the mean depth of the maximum signal remained relatively constant. There was generally poor agreement between the satellite derived SST values and the airborne-derived values (bottom). Also, satellite values were more variable within each range than airborne values.
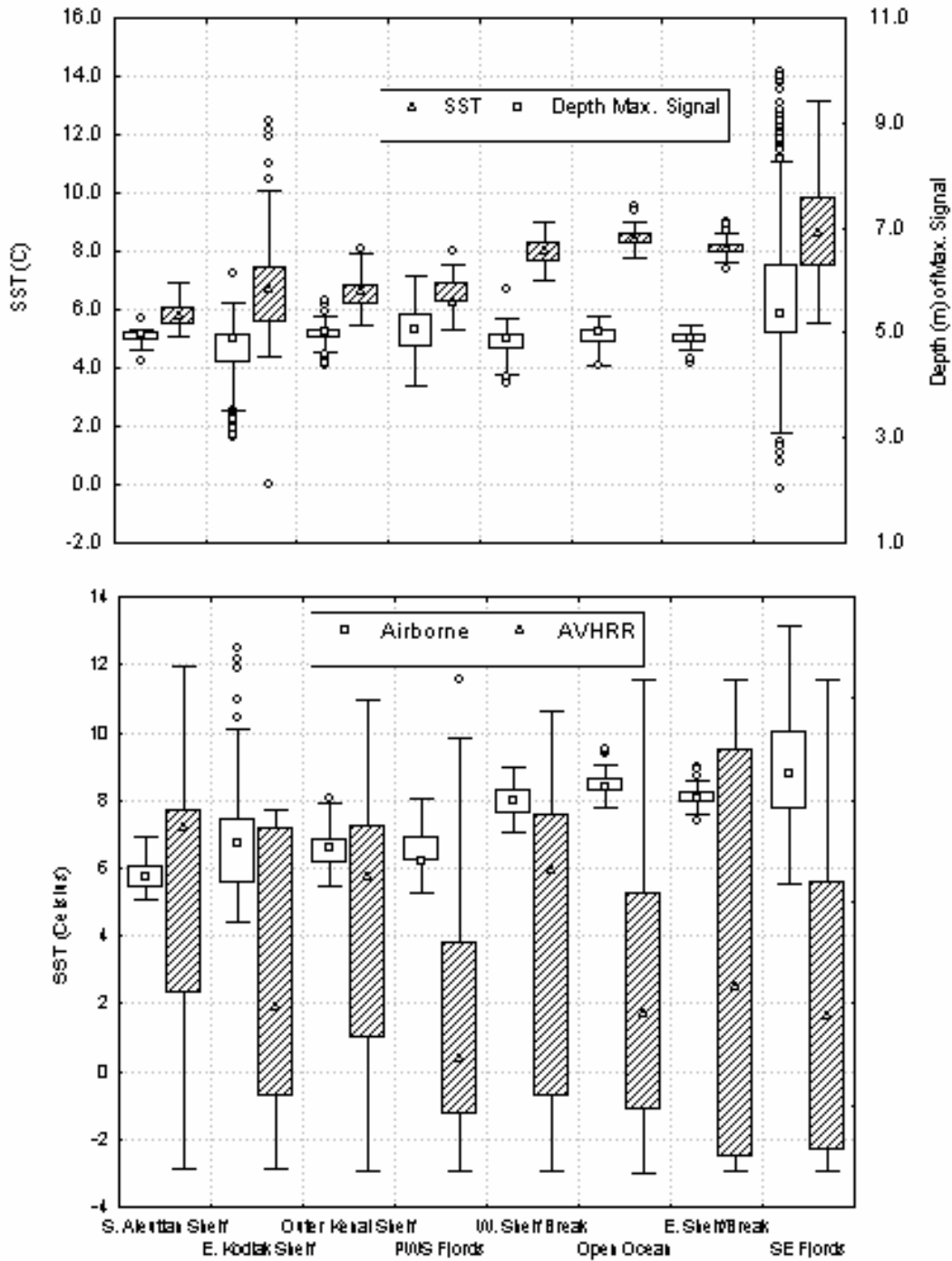
Figure 14. A cluster analysis based on the number of significant differences in pair wise testing between zones for all variables (top) and based on K-means clustering using Euclidean distances (bottom) among means of the 6 variables (attenuation coefficient, penetration depth, maximum signal, depth of maximum signal, airborne SST, and integrated signal). For the K-means cluster analysis, shown are the proportion of data points assigned to each cluster from each zone. Similarities are noted by looking for similar cluster assignment patterns. Zones 6 and 7 (open ocean-eastern shelf / shelf break) as well as zones 3 and 4 (Outer Kenai – PWS). All other zones were unique from one another.

Zone	1	2	3	4	5	6	7	8	Total
1		2	2	5	4	3	3	7	26
2	2		3	6	4	3	2	5	25
3	3	3		4	2	2	3	6	23
4	4	4	2		1	1	2	3	17
5	4	4	2	2		1	2	5	20
6	3	3	2	3	1		0	5	17
7	2	3	3	4	2	0		4	18
8	6	6	6	4	5	5	5		37

35
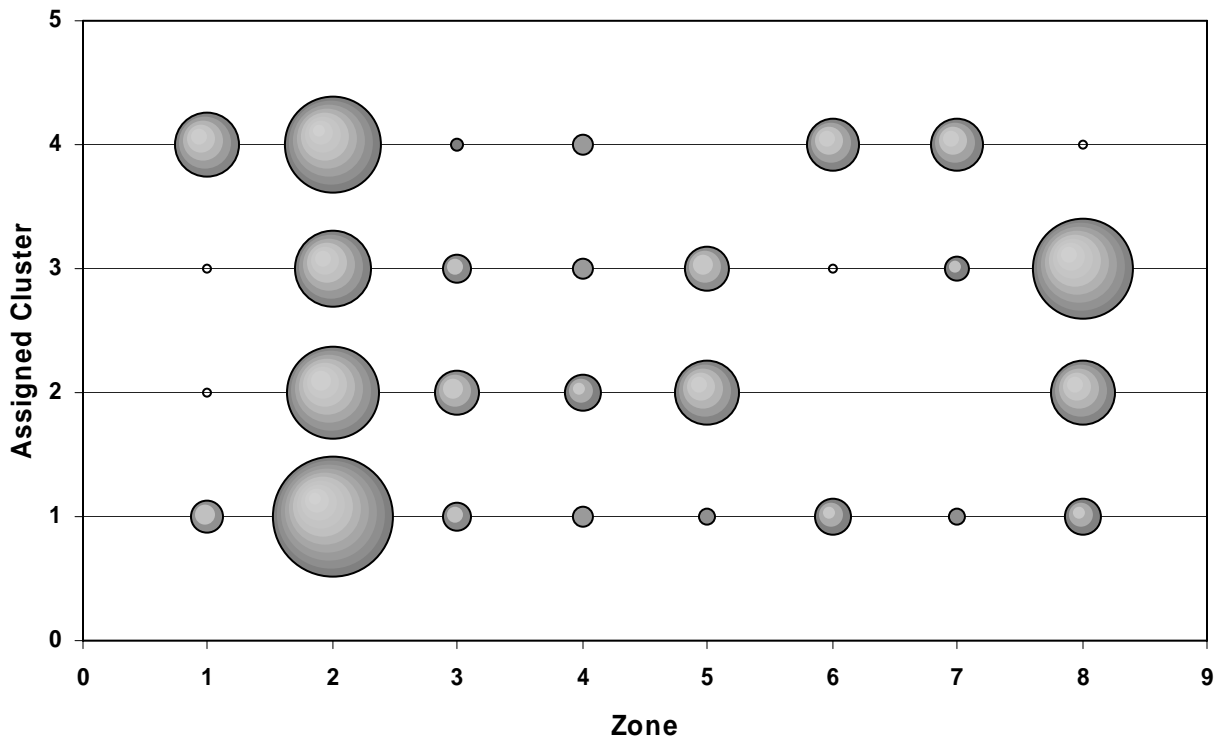
Diel Patterns of Horizontal and Vertical Fish and Plankton in the Kodiak Region

During July, 2001, a broadscale survey was conducting around Kodiak Island (Figure 3). We identified 1000 shot (half) files, representing approximately 2 km along track, that included two general feature types: plankton layers and fish aggregations. The layers are identified as signal (total return minus background at depth) that persists over several thousand shots, that occurs gradually in the shot profiles, and that is characterized by smooth "bulges" in the shot profiles and processed using a threshold value of 1 (T=1; equation 2). School aggregations are identified as signal that generally persists over only a few shots, that occurs suddenly in the shot profiles, that can be characterized as "spikey", and for which a very strong signal (compared to layers) is returned. For fish, a threshold value of 2 was used in signal processing. The distribution of 2 km bins that included signal interpreted as fish and/or plankton layers was plotted for day versus night flights (Figure 15). During the day, we identified 70 bins with fish and 81 bins with layers. During the night, 57 bins contained fish while 413 contained layers. The most notable differences were the abundance of fish in Marmot and Chiniak Bays (NE Kodiak) during the day but lack of any feature during nighttime. Plankton layers appeared along SE Kodiak in a nearly continuous band at night, possibly representing the concentration of vertical migrators, such as large copepods and euphausiids. During the day, plankton layers in this area were much patchier.

In order to demonstrate the fine-scale variability in horizontal and vertical distribution of biota, we processed data for a single survey conducted during the night on August 10 in Chiniak Gully. We plotted the variation in depth penetration, ranging from 20 to 50 m as well as the integrated signal from 0 to 25 m (Figure 16). The depth penetration along the flight path was estimated as the depth at which a threshold signal occurred. Because light attenuates with depth and attenuation varies with water body, at any given location there is a depth where signal cannot be discriminated from noise. The signal return at this depth is the threshold. In general, penetration was highest in the middle of the gully in water deeper than 100 m while penetration was lowest next to the coast or at the edges of the gully. The integrated signal, represented as the total signal between 0 to 25 m in depth, was also variable but highest in the center of the gully in areas over 20 km offshore (Figure 17). Each file was binned at 1 m depths to examine variation in signal by depth. Over the entire survey area, we plotted the average signal and the maximum signal observed at each 1 m depth bin (Figure 18). We observed that in Chiniak Gulley, during nighttime in mid-August, the mean signal peaked at 12 m while maximum signal peaks were observed at 9, 14, and 18 m depths in decreasing order of magnitude. The integrated and depth-specific signal was interpolated over a grid with 1000 m blocks and the smoothed surface plotted over the entire region (Figure 18). The hot spot was a concentration of targets approximately 20 km offshore in the center of Chiniak Gully. This hot spot occurred at all depths, but some depth-specific differences were noted. At the shallower depths (6 and 9 m shown), signal was also strong in nearshore areas in Chiniak Bay as well as at the edges of the gully. At the medium depths (12 and 14 m), there was a swath of strong signal centering over the gully but expanding out over the edges of the gully in some areas. At the deepest depth shown (18 m), the signal was

strongest at the hot spot and at the mouth of the gully crossing the 100 and 200 m isobaths approximately 50 km offshore.

The broadscale survey tracks were performed over a 3 d period for a total flight time of approximately 15 hours. The ship survey covered this region over a period of 10 days with several days anchored because of severe weather. Due to the high short-term (2-3 d) variability observed, we do not believe a ship survey can provide a true synoptic picture of biological features available to sea lions and other marine mammals. Rather, feeding events are ephemeral in relation to the availability of fish aggregations that are, in turn, likely responding the variation in plankton density and patchiness.

Figure 15. A day to night comparison in distribution of plankton layers (green circles) and fish aggregations (pink circles with diamonds) during the July survey period in Eastern Kodiak Island. Each day-night survey pair was completed within a 24 hr period. Each mark represents approximately 2 km along the survey track and indicates that the specified feature occurred within that area.
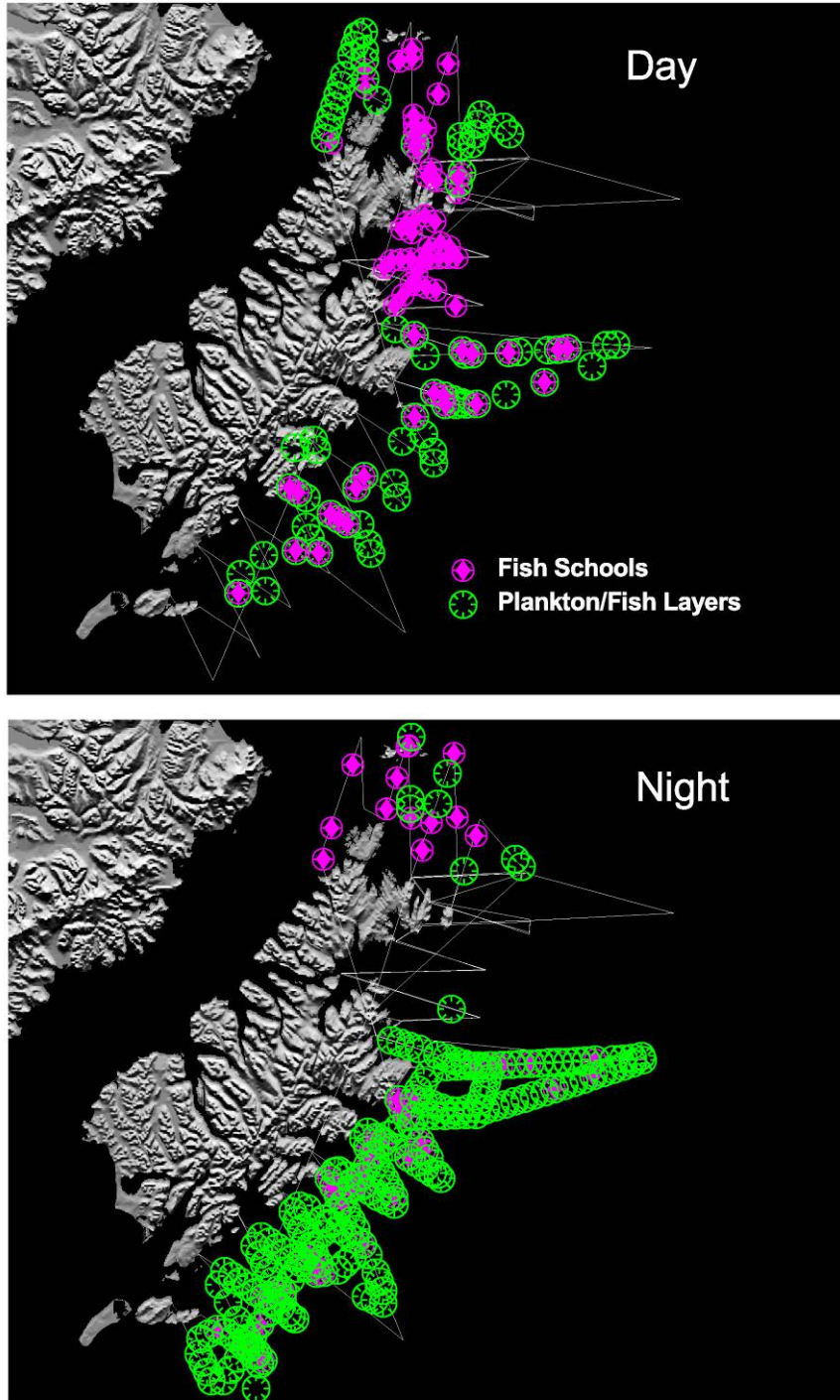
Figure 16. The along track depth penetration (top) of the lidar and integrated signal return through all depths (bottom) during the night survey on August 10, 2001 in Chiniak Gully. The level of the signal is related to the size or density of targets observed.
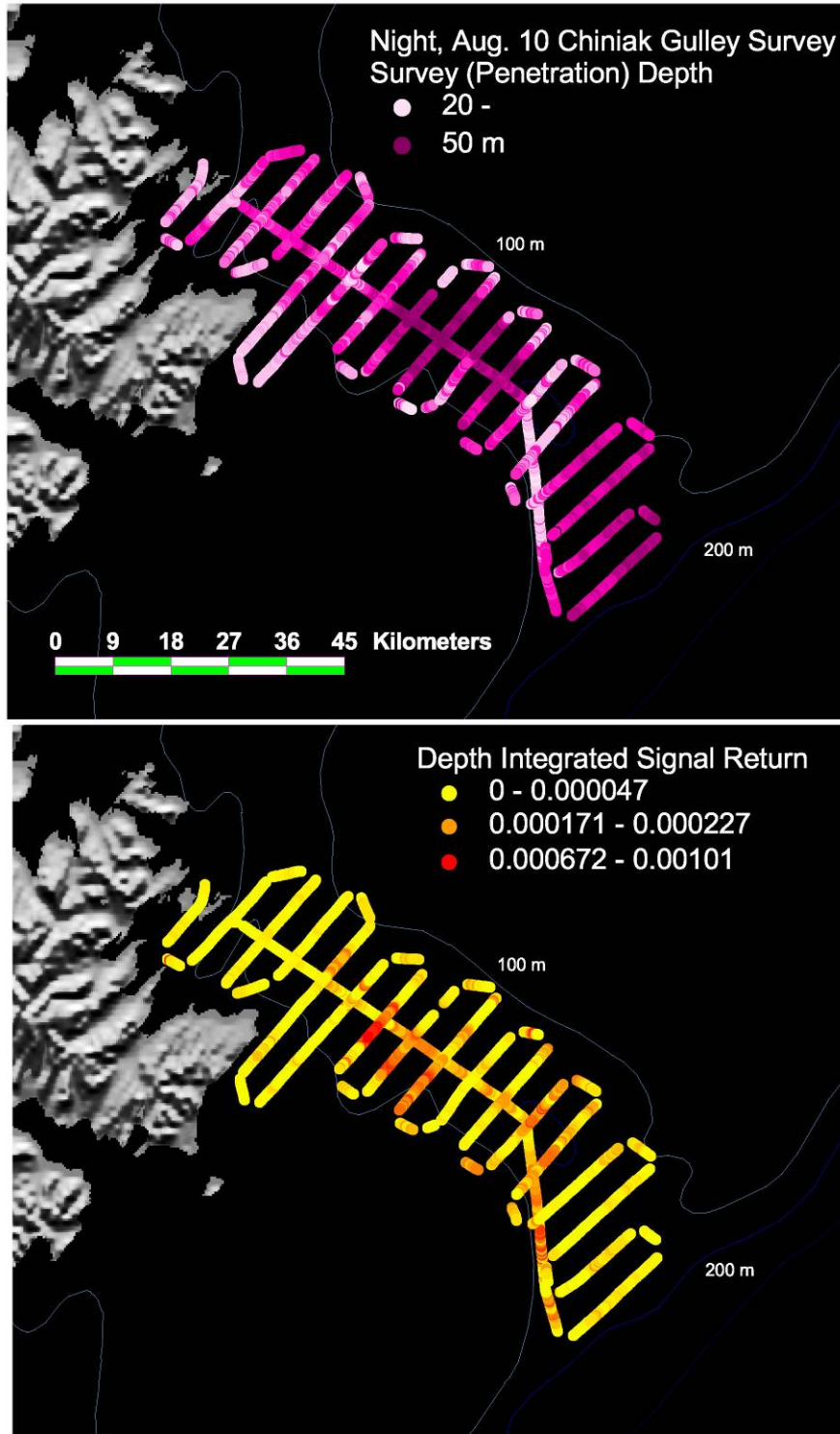
Figure 17. The maximum and average signal by depth at night over the entire survey area on August 10, 2001 in Chiniak Gulley.
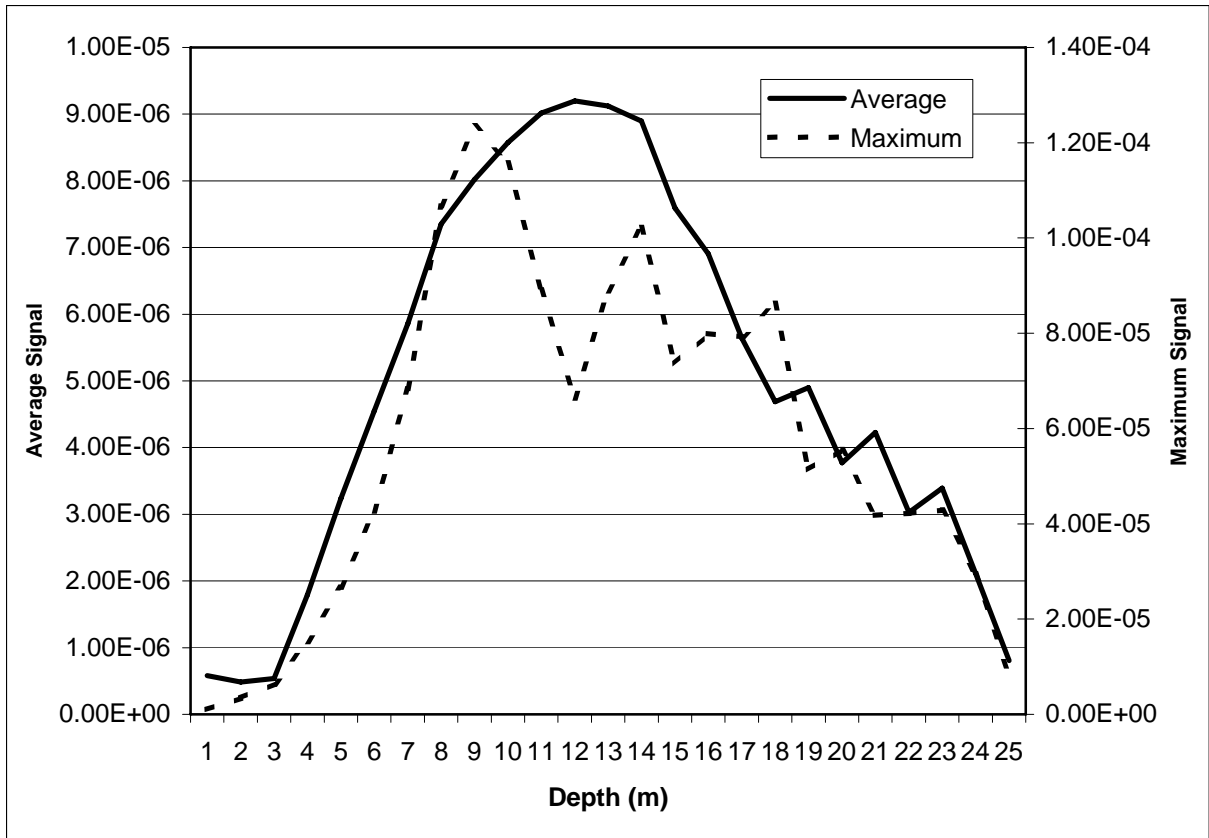
Figure 18. Spatial smoothing of signal intensity during the night survey on August 10, 2001 for the integrated signal between 0 and 25 m (upper right) and the depth specific data at 6, 9, 12, 14, and 18 m. The data was gridded at 1000m blocks and depths were chosen using Figure 6 and the depth at which the first peak maximum signal was observed (9 m), the peak of the mean signal (12 m), the second peak in maximum signal (14 m) and the third peak in maximum signal (18 m).
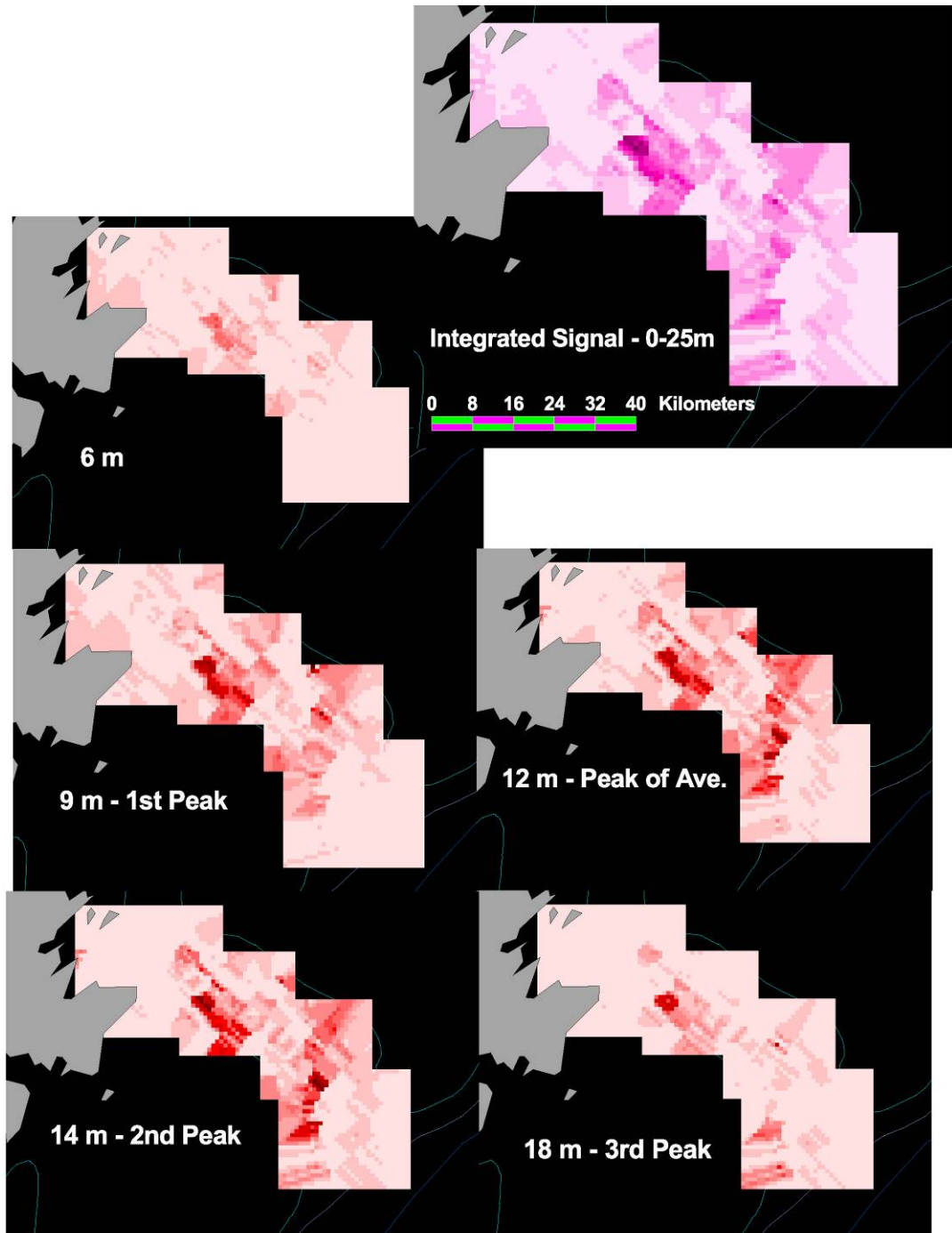
Ship Avoidance Affecting Surveys of Forage Fish

A problem in the ecological interpretation of data collected from ship is the destruction of *in situ* biological structure. Several species of fish, e.g. capelin, have been observed to avoid ships. The distribution of these fish is then interpreted to be deeper and abundance or density estimates are then affected.

These results are from synoptic airborne and shipboard surveys in an area known to be dominated by pollock and another dominated by capelin. In each flyover, we recorded the surface structure and changes in signal strength as a function of distance to the ship. Preliminary results were shown in the last interim report. These results have severe implications for interpretation of shipboard results of two intermixed species including one that has known ship avoidance behavior (capelin) and another that does not (pollock). The behavior of these two species is very different as capelin are tightly schooled and exhibit dynamic horizontal and vertical movements while pollock are loosely aggregated and do not exhibit dynamic movements. In this case, acoustic signal may be improperly interpreted if proportion of capelin signal is derived from deep-water trawl catches that contain capelin yet ship avoidance behavior excluded that proportion of capelin from acoustic signal. This phenomenon has been documented in Iceland, especially during the summer when capelin exhibit near-surface distributions as they feed on plankton blooms. If sea lions are utilizing capelin in the summer and research on foraging ecology depends on ship-board results, the potential for error may be high.

In 2002, we worked with Chris Wilson on the Miller Freeman who was examining the problem. An acoustic buoy with a hydrophone was deployed and the ship ran multiple transects toward and away from the buoy in two localities. Fish species at one locality was mainly juvenile pollock while the other locality was dominated by capelin. We flew multiple transects over these same transects and, in a preliminary analysis, found that signal strength from biological structure decreased steadily as a function of distance to the ship (Figure 19). In addition, integrated signal return in the upper 20 m was significantly reduced behind the ship compared to in front of the direction of travel (Figure 20). A full analysis of the combined lidar-acoustic data set was desired but the acoustic data was not available despite repeated requests. A full analysis and publication of the important work should be completed and should be prioritized in the future.

Figure 19. Preliminary results for an analysis of ship avoidance in cooperation with Dr. Wilson and the Miller Freeman. Average lidar return in depth bin 3 – 10 m versus distance from center of ship. Negative distances are behind, positive in front. Ship signal saturated receiver and has been arbitrarily set to zero.
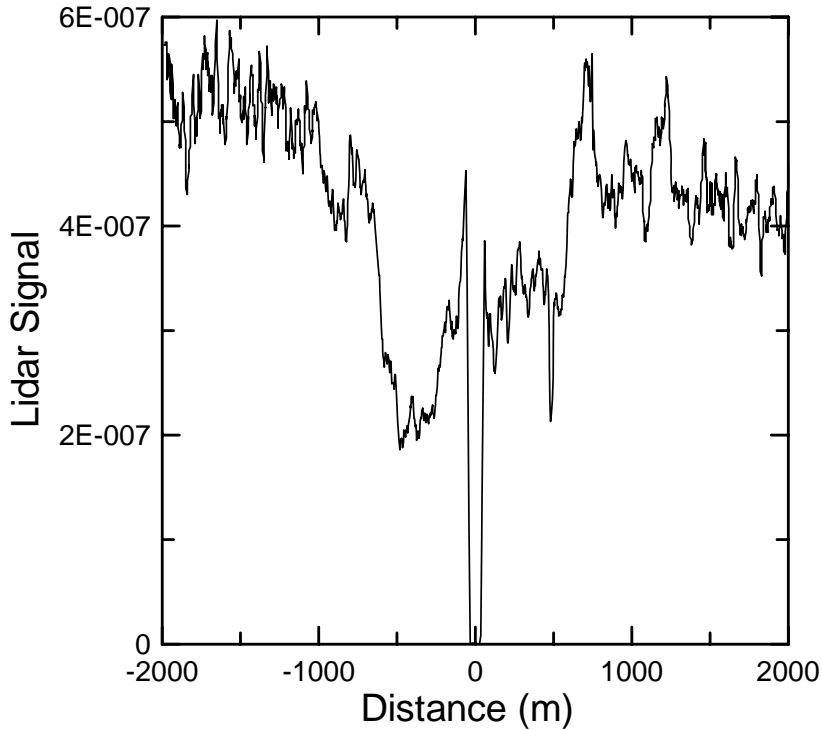
Figure 20. Preliminary results for a study on ship avoidance shown here as an echogram in the vicinity of the Miller Freeman. The ship is moving from left to right. White space in center is where the lidar went over the ship. Enhanced scattering just behind ship is probably bubbles from wake.
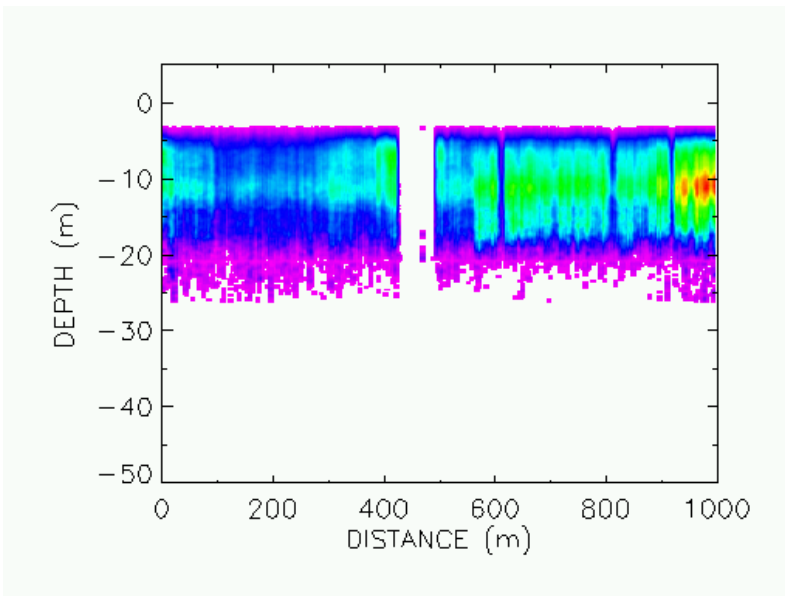
Short-term Impacts of Storm on Surface Productivity and Biological Distributions

Frequency and intensity of storms can greatly affect the overall biological productivity of a region and, in turn, affect the prey availability and density of food for sea lions. In cooperation with AFSC cruises in August of 2001 and 2002 (Miller Freeman), we examined our data in the two sampling locations for the NMFS study, Chiniak and Barnabus Gullies on the eastern shelf of Kodiak.

These results were presented at the American Society of Photogrammetry and Remote Sensing in Anchorage Alaska during May of 2003. The title of the talk was:

Aerial Remote Sensing: How storms and topography affect biological distributions in the upper 20 m by Brown et al.

The storm had a significant impact on physical and biological structure in the surface. The SST was significantly reduced both during the day and night surveys (Figure 21). The daytime mean was reduced by 4 degrees (15.1 to 11.0) while the nighttime mean was reduced 3 degrees (14.6 to 11.6). This drop was caused by wind mixing during the storm that brought cold water up from depth (Hollowed et al. 2002). Although the mean green index value increased slightly after the storm (.27 from .24; Figure 22), the range of values drastically narrowed with maximum values dropping by half. The means of the average integrated day and night time signals were significantly ($p<0.001$) higher before the storm than after (day: 805 to 675, night: 384 to 258)(Figure 23). There was also a significant difference between day and night during both periods. After the storm, the range of signal values also decreased. The changes in spatial structure can be seen in Figure 24 for ocean color (green index) and in Figure 25 for the average integrated lidar signal. Overall, structure was patchier with a wider range in values (complex spatial structure) before the storm. In general, the storm reduced patchiness and likely mixed the plankton layers below the euphotic zone. The result was less food in the surface for fish, less fish for seabirds to prey on, and an overall dramatic change in ecosystem structure.

This data demonstrates the importance of storm events to biological processes and marine ecosystem functioning. It under scores the potential effects from global climate change if storm frequency is affected.

Figure 21. Distributions of SST values during the day (top plots) and night (bottom plots) before (yellow) and after (red) the storm.
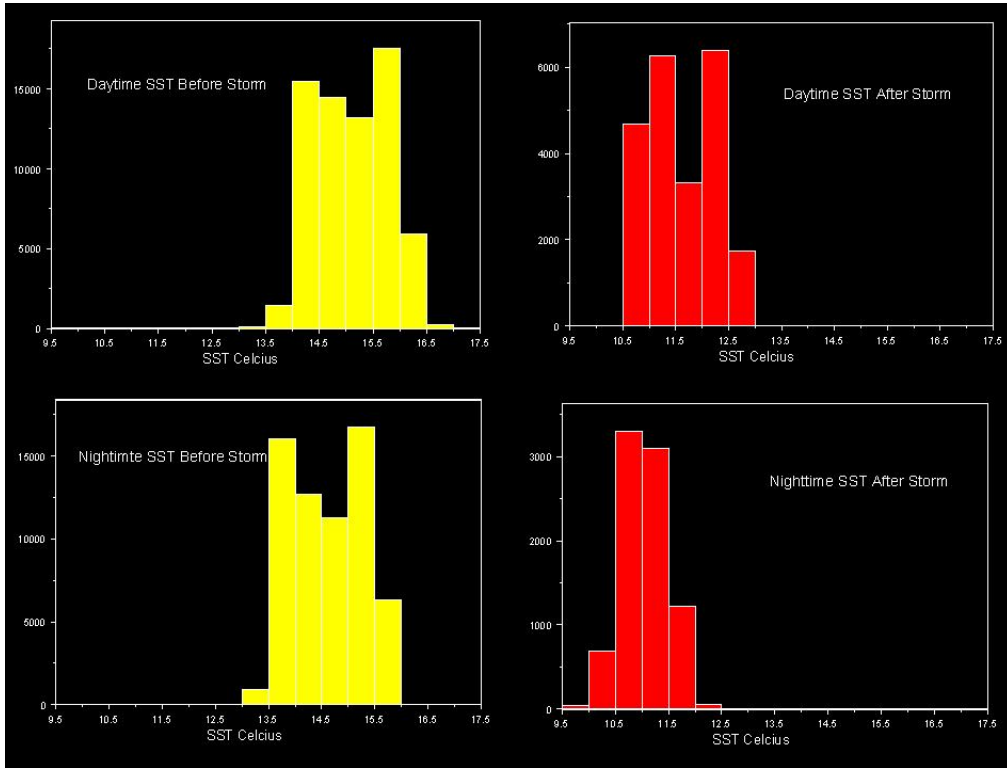
Figure 22. Distributions of ocean color values (expressed at the green index, a proxy for ChlA) during the day before (yellow) and after (red) the storm.
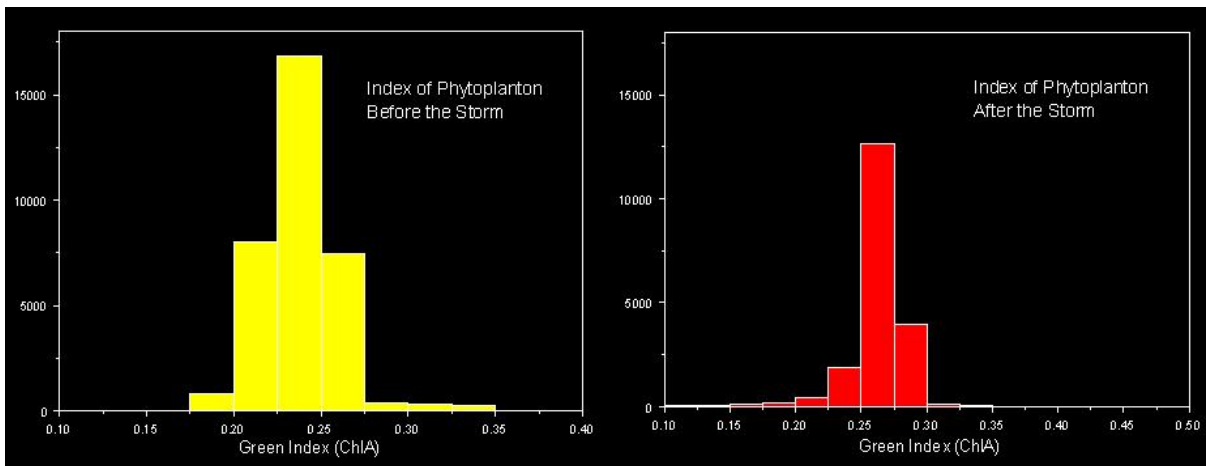
Figure 23. Distributions of lidar signal representing mixed zooplankton and fish aggregations during the day (top plots) and night (bottom plots) before (yellow) and after (red) the storm.
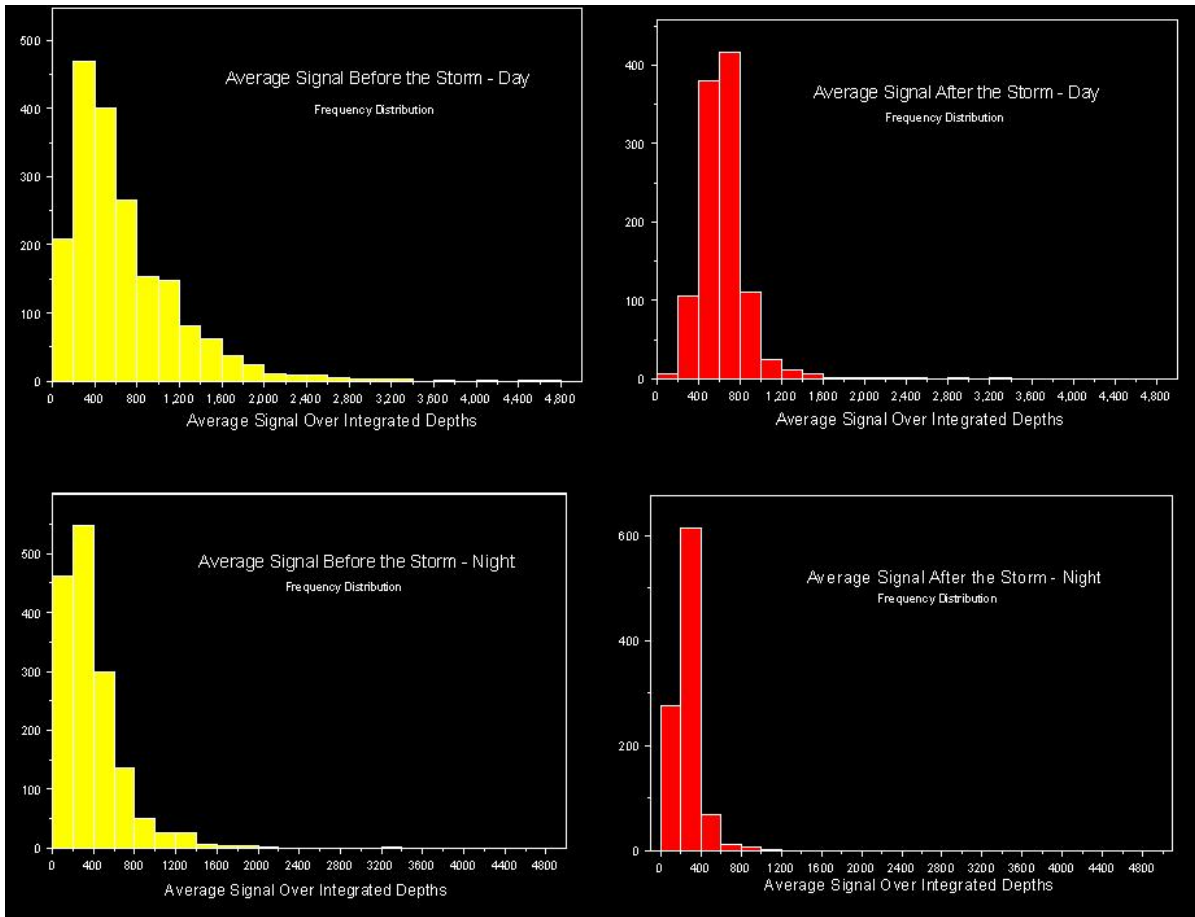
Figure 24. Spatial distributions of ocean color values (represented by Green Index) during the day before (left) and after (right) the storm. Higher values correlate to more ChlA.
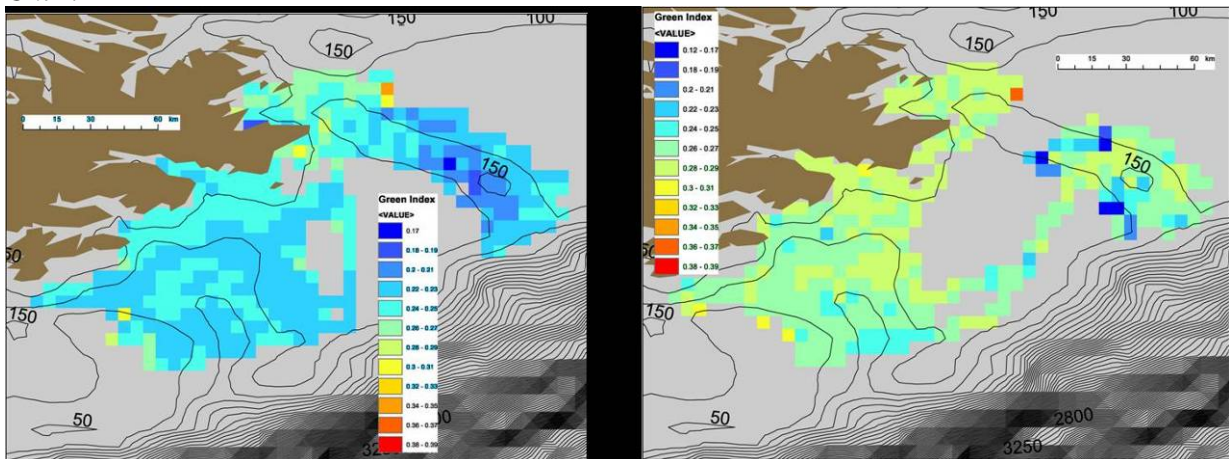
Figure 25. Spatial distributions of average integrated lidar signal during the day (top figures) and night (bottom figures) before (left) and after (right) the storm. Higher signal values correspond to increased numbers or density of fish and zooplankton. Note that the scales change.
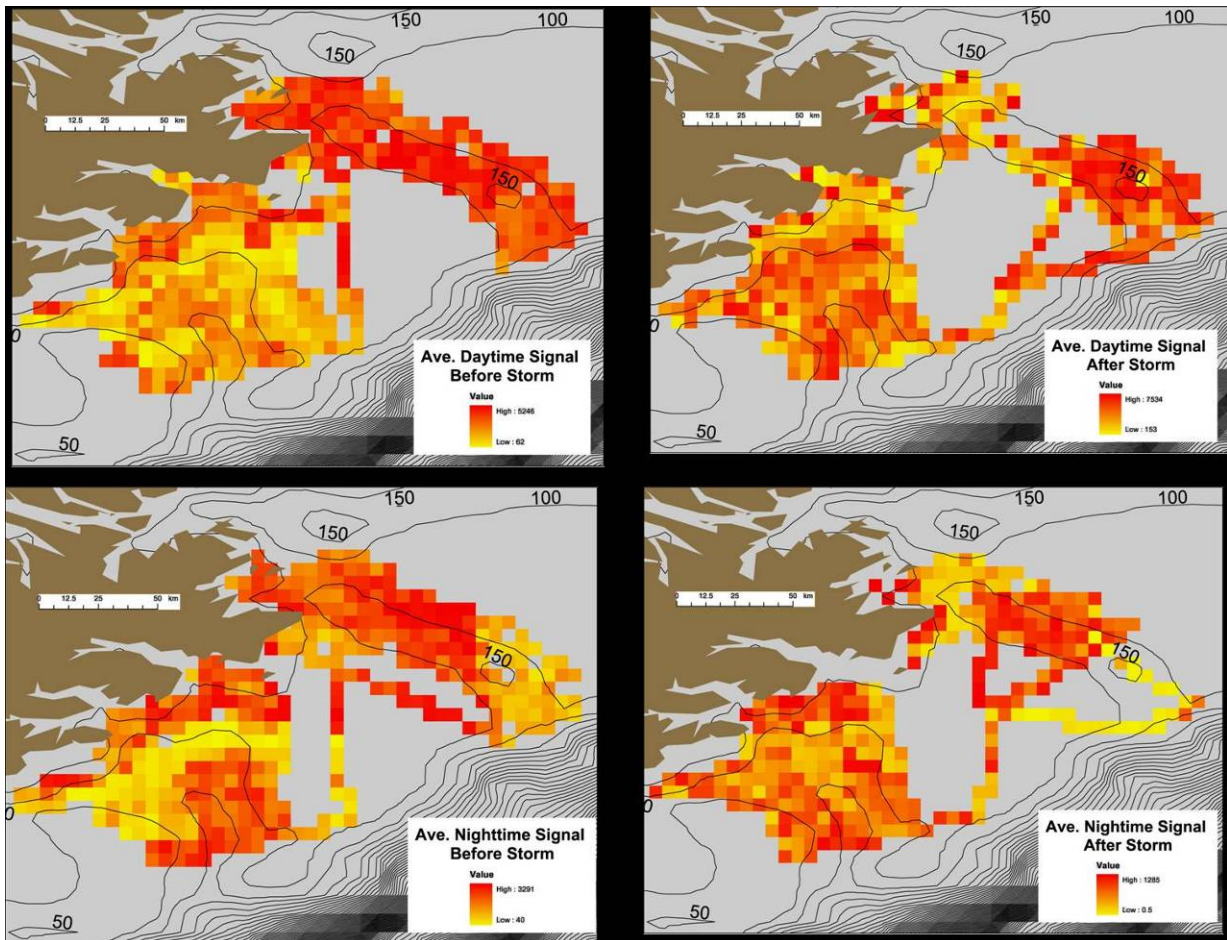
Evaluation of Airborne Lidar for Estimation of Zooplankton Standing Stocks

The results for this section result from a talk given at the ICES 3rd International Zooplankton Production Symposium in May of 2003. The title of the talk was:

Using airborne remote sensing to map zooplankton standing stocks, associated ocean conditions, and to develop community-level optical signatures.

E.D. Brown, M. A. Montes Hugo (Institute of Marine Science, University of Alaska Fairbanks, Fairbanks, AK 99775-7220; ebrown@ims.uaf.edu, mmontes@ims.uaf.edu)
J.M. Churnside (NOAA Environmental Technology Laboratory, R/E/ET1,

325 Broadway,Boulder, CO 80303; James.H.Churnside@noaa.gov
K.O.Coyle (Institute of Marine Science, University of Alaska Fairbanks, Fairbanks, AK 99775-7220; coyle@ims.uaf.edu)

This study demonstrates the potential utility of airborne derived data for zooplankton studies. Aircraft surveys were coordinated with ship studies during May 2000 over a cross-shelf transect in the northern Gulf of Alaska (GOA). Data from lidar (532 nm laser) backscatter, an infrared radiometer, and the green band from a RGB imager provided information on distribution and densities of plankton layers, fish schools, SST, and an index of Chl a or phytoplankton standing stocks. Shipboard data included depth-specific sampling using a Mocness plankton trawl, high frequency acoustics, hydrographic data, and Chl a measurements. Remotely sensed data were validated and interpreted using shipboard and fixed-location buoy data. Signal data from lidar was integrated within 10 m depth and 100 m along track bins where there was overlap with a ship sampling station and an aerial survey transect. Only these overlapping bins were used in the regression analysis. Airborne derived measures of Chl a, including the light attenuation coefficient, were positively correlated with shipboard measurements of Chl a (Figure 26a). Airborne derived Chl a and the attenuation coefficient were negatively correlated with SST (Figure 26b) but positively correlated to lidar signal strength (Figure 27a). Ship derived biomass of zooplankton and abundance of larval fish were weakly positively correlated to Chl a (Figure 27b) whether derived from ship or airborne data. These results indicate that oceanographic data deterministic of plankton density or abundance can be collected from airborne platforms. Depth specific airborne derived lidar signal strength was correlated to density of some species groups of plankton derived from Mocness tows. In the 11 to 20 m depth range, correlations between biomass per unit area of gastropods, chaetognatha, amphipods or large copepods and lidar signal strength were among the most highly significant (Figure 28a). For density expressed as abundance per unit area, correlated for amphipods, gelatinous zooplankton, gastropods as well as total zooplankton (all species) were among the highest (Figure 28b). The differences in correlation between lidar signal strength and zooplankton species groups were probably due to differences in optical signatures among the groups. Profiles of lidar return (Figure 29) reflected a highly structured community by depth often with a roughly bimodal shape reflecting a two-layer biological structure. There was a distinct signal profile in the upper 10 m and a different, often stronger profile from 10 to 20m. Species compositions from the Mocness tows reflected a similar two-layer structure with distinct community structures in each of the two depth strata.

The conclusions of these results are that differences in community structure across regions can be detected by unique optical signatures and that differences in physical parameters (ocean color, light attenuation and Chl a, detected from remote sensing) explain the variability observed. These are exciting findings that require in *situ* and in *vitro* targeted studies to understand and model the signatures observed that reflect community structure.

Figure 26. Correlations between (a) airborne-derived green index from the RGB imager and shipboard Chl a measurements or the airborne derived optical attenuation coefficient; (b) correlations between airborne-derived SST and the green index or attenuation coefficient.
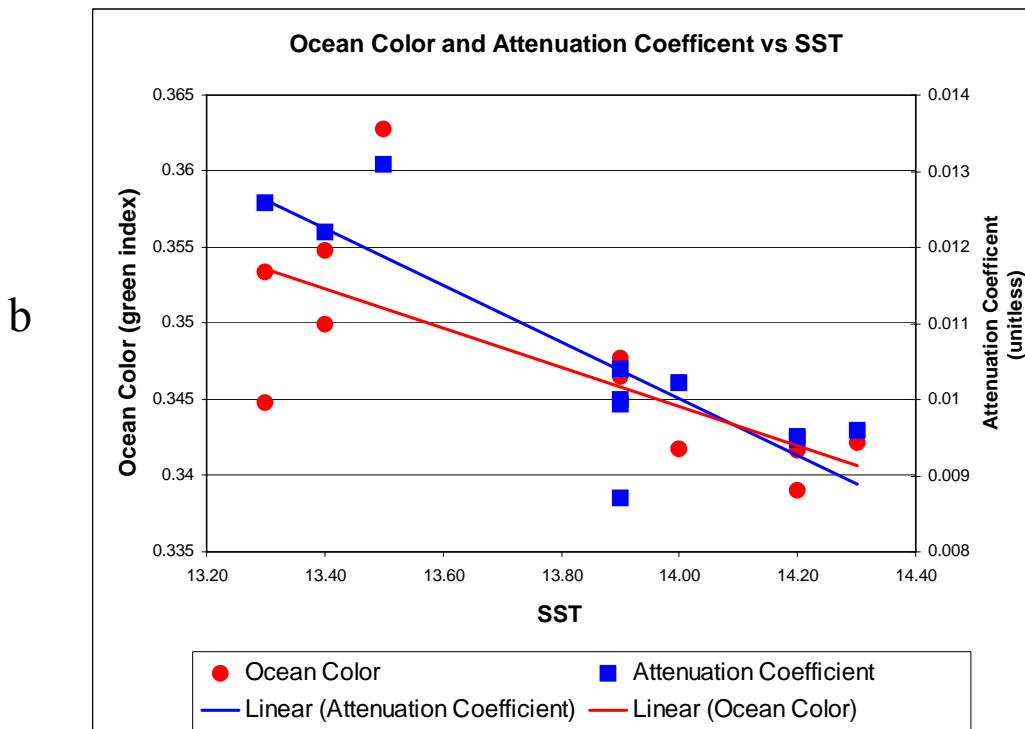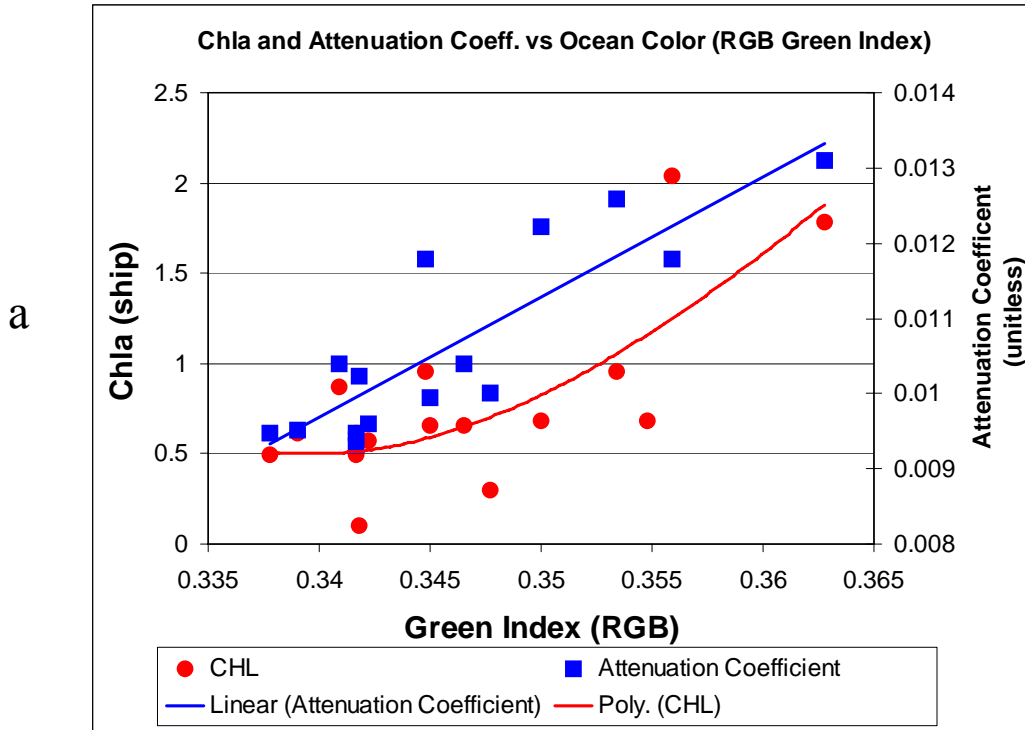
Figure 27. Correlations between (a) airborne-derived integrated lidar signal strength from 10-20m and airborne-derived green index from the RGB imager or the airborne derived optical attenuation coefficient; (b) correlations between shipboard-derived Chl a and the density of zooplankton (biomass per unit area) from 10 to 20m depths or the density of larval fish (abundance per unit area) in the upper 10 m.

a

b
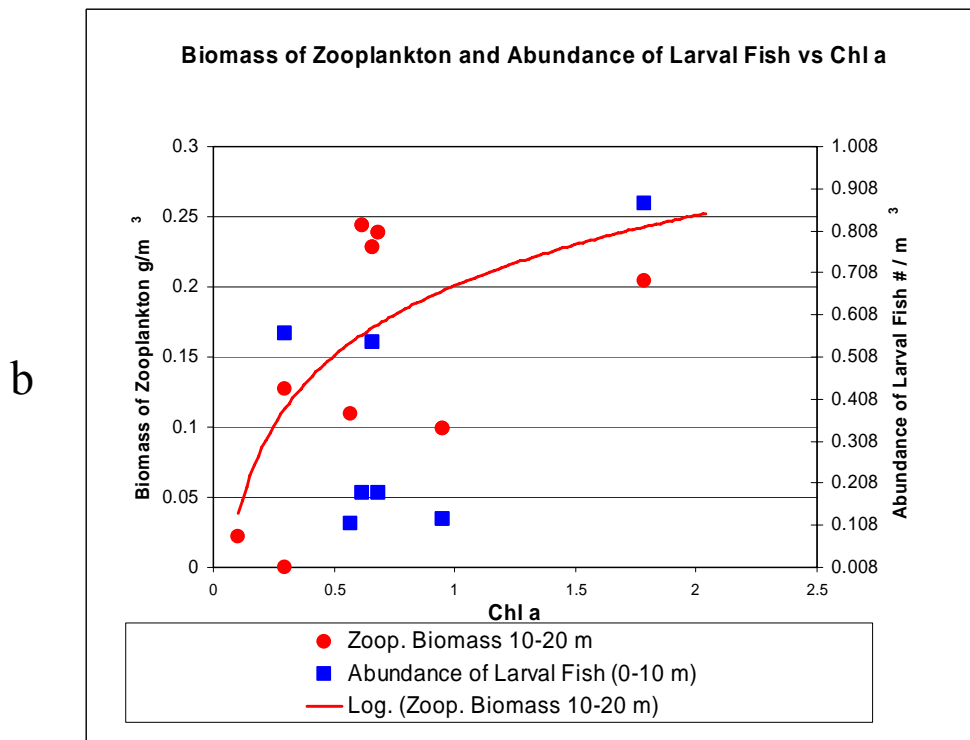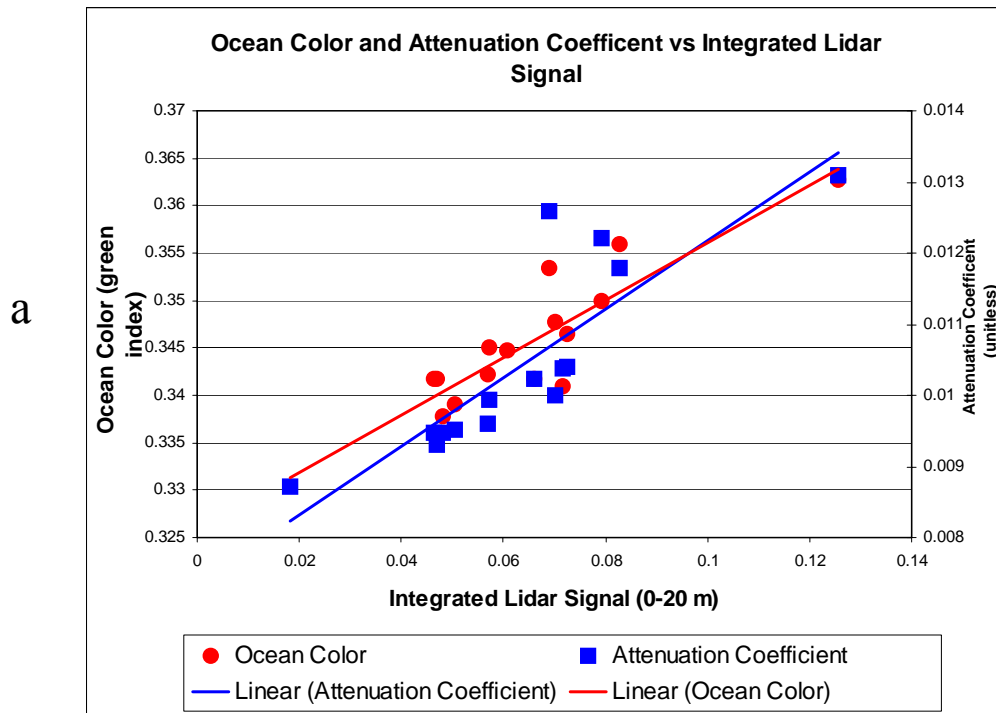
Figure 28. Significant correlations between (a) airborne-derived integrated lidar signal strength from 10-20m and the density (biomass per unit area) of four species groups of zooplankton; (b) airborne-derived integrated lidar signal strength from 10-20m and the density (abundance per unit area) of three species groups of zooplankton or total zooplankton (all species) density.

a
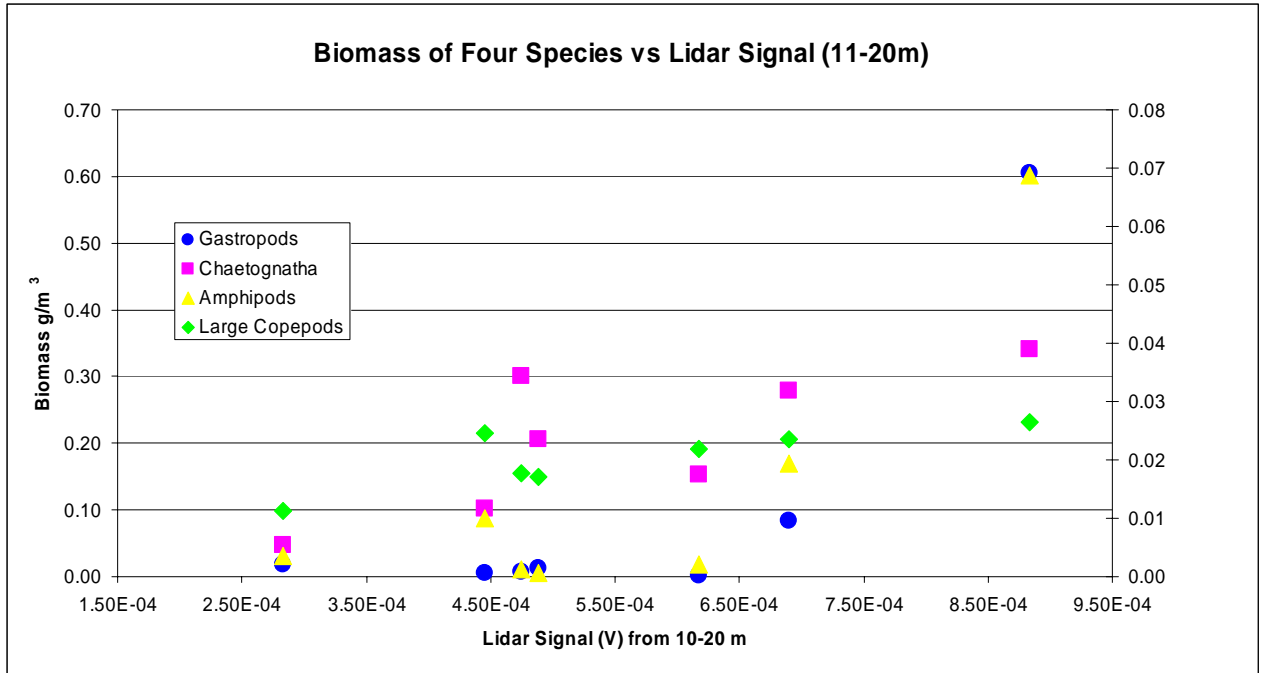
b
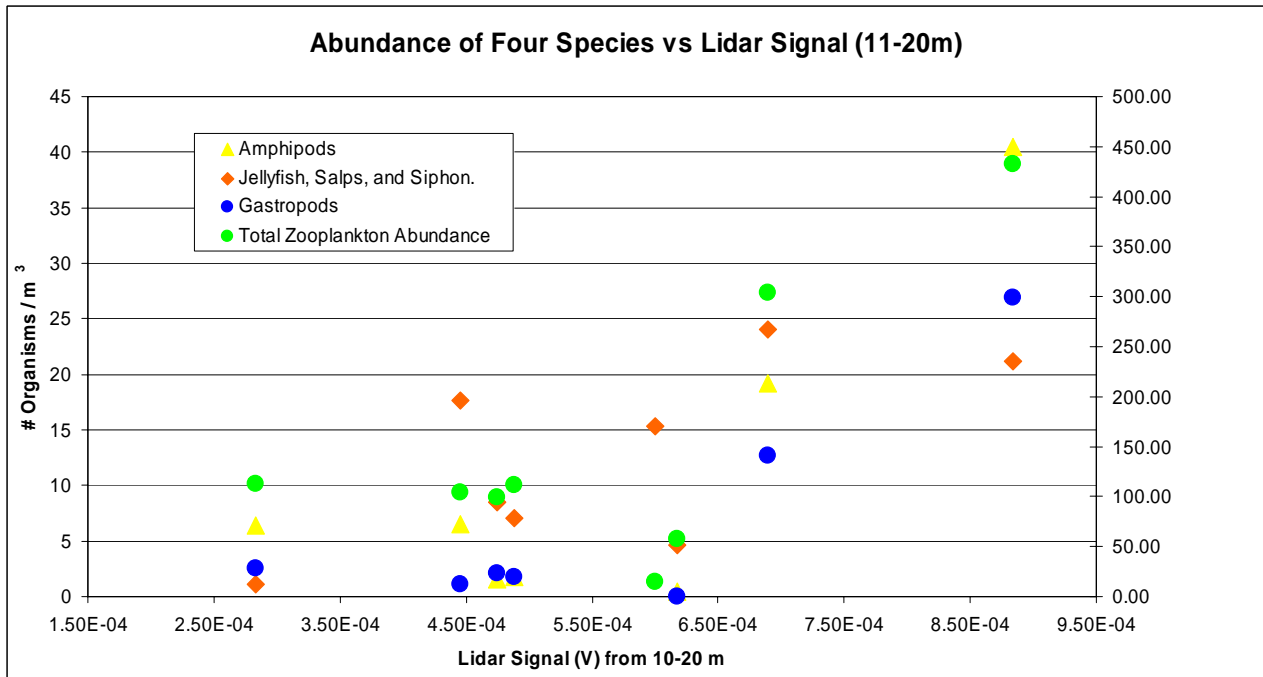
Figure 29. The graphs indicate fine scale detail in the structure and spatial variability (200 m resolution) at several GLOBEC zooplankton sampling stations. The pie diagrams represent community structure from Mocness tows for the 0-20 m depth (left) and 20-40 m depth range (right). Lidar profiles show the "two-layer" structure also observed in the net sampling with distinct species composition differences.
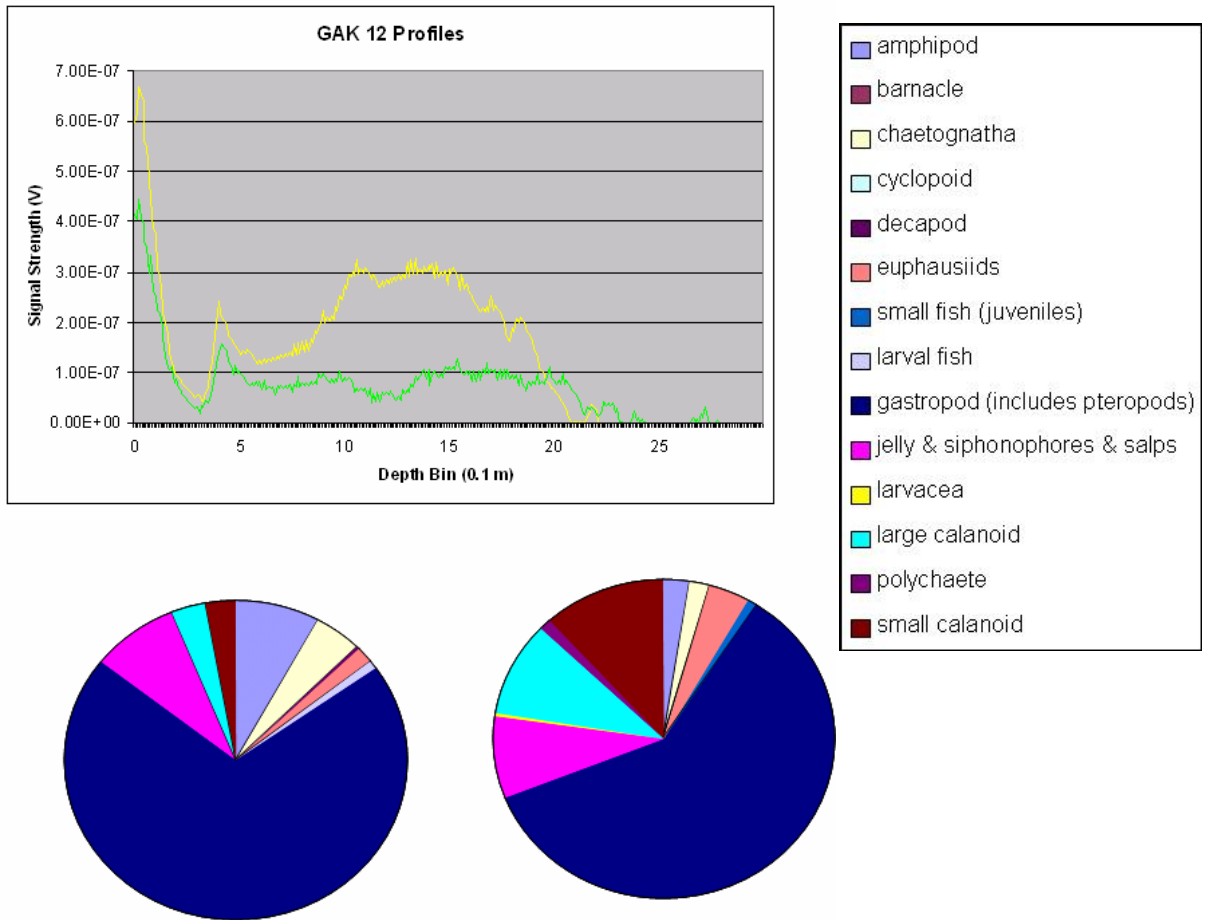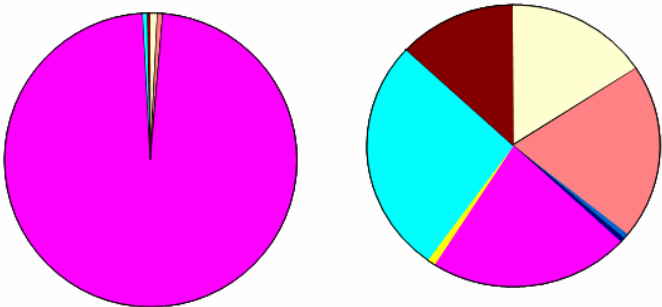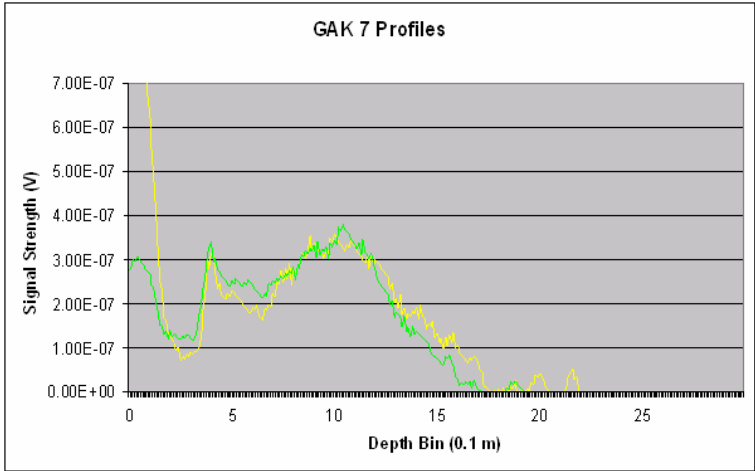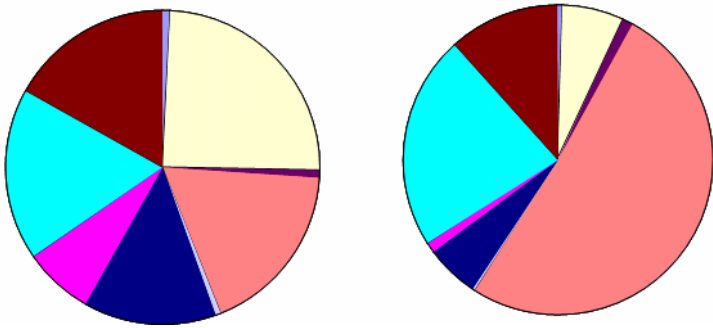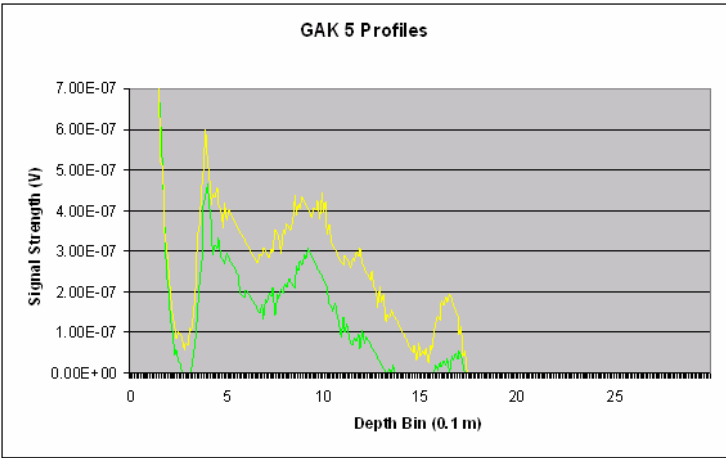
Estimating Phytoplankton Biomass with Airborne Remote Sensing

The results for this section are representing by a draft publication attached in Appendix I entitled:

Estimating phytoplankton biomass in coastal waters of Alaska using airborne remote sensing

By Martín A. Montes-Hugo,, Kendall Carder, Evelyn Brown, Robert J. Foy, Jennifer Cannizaro, Scott Pegau

Abstract

Empirical airborne remote-sensing relationships were examined to estimate chlorophyll <u>a</u> concentration in the upper mixed layer (chl_{FOD}) of coastal waters of Afgonak/Kodiak Islands during July-August 2002. Band-ratio and spectral-curvature models were tested using satellite remote-sensing reflectance ($R_{rs}(\lambda)$) measurements. Additional shipboard and airborne $R_{rs}(\lambda)$ data were also analysed to evaluate consistency of proposed chl_{FOD}-$R_{rs}(\lambda)$ relationships. Validation of chlorophyll algorithms was performed using data collected in the northern-part of the Gulf of Alaska and Bering Sea during 1996, 2002, and 2003 cruises. Likewise, oceanographic conditions during the surveys were typified to interpret variability of chl_{FOD} fields. The SeaWiFS band-ratio algorithm OC2d was the most sensitive R_{rs} combination ($R_{rs}(509)/R_{rs}(553)$) to detect chl_{FOD} variability. No valid statistical regressions were established for band-ratio or spectral-curvature relationships in the blue spectrum (<500 nm). Fertile waters (>5 mg m^{-3}) were preferentially located over shallow banks (~50 m) and the entrance of the bays. The approach used in this study to derive chl_{FOD} values could be universal for Alaskan coastal waters. However, chl_{FOD}-$R_{rs}(\lambda)$ relationships must be calibrated locally for a given season.

RGB Video andThermal Imagery, an Aerial Image Training Se for Seabirds, and Gated Camera Results

Attached are sampled of the video imagery processed. They show results from the thermal infrared (IR) camera and three-chip color video (RGB) imagers that are run simultaneously during flights. Because the time and location codes are recorded on the digital tracks of both imagers simultaneously, the imagery can be overlaid in a given time code representing identical spatial regions. The strengths of the IR camera for mapping sea bird and marine mammal distributions are demonstrated. This is obviously true at night; however, the strengths can also be seen in cases of rough water and sun glints or glare. Sea bird distributions may be strong indicators of productive areas as sea birds are often seen associated with whales and other marine mammals. Sea bird distributions will be combined with subsurface signal strength from the lidar to quantify the relationship and association (sea birds – subsurface standing stocks). If the association is strong, sea

bird distributions may be indicators of pelagic foraging patches for marine mammals and sea lions. These data were mapped to excel spreadsheets.

Our main recommendation for RGB and thermal imaging is to increase altitude where possible. Although 300 m is optimal for the lidar, video collection is optimized at much higher altitudes due to the high resolution capabilities of the cameras, the reduction in glint and reflection issues, and to maximize the image swath (a function of altitude). However, over Alaskan waters, clouds often restrict the aircraft to under 2000 ft so to be fully useful, cameras much be adjustable for operation at low and high altitudes.
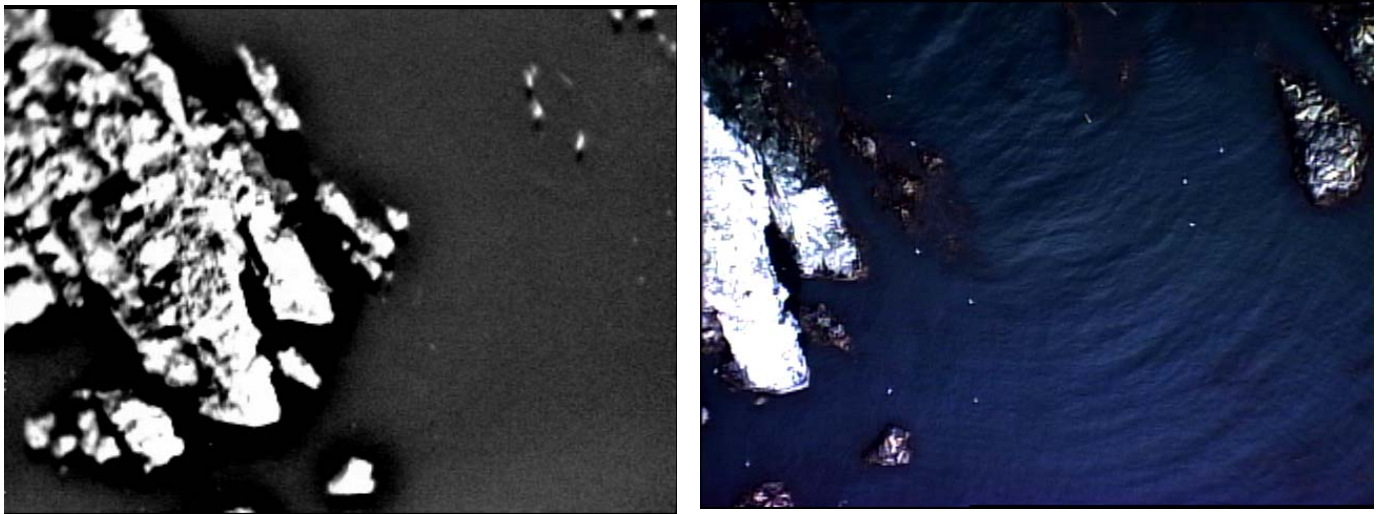
Figure 30 - IR (left) and RGB (right) images of birds by rock
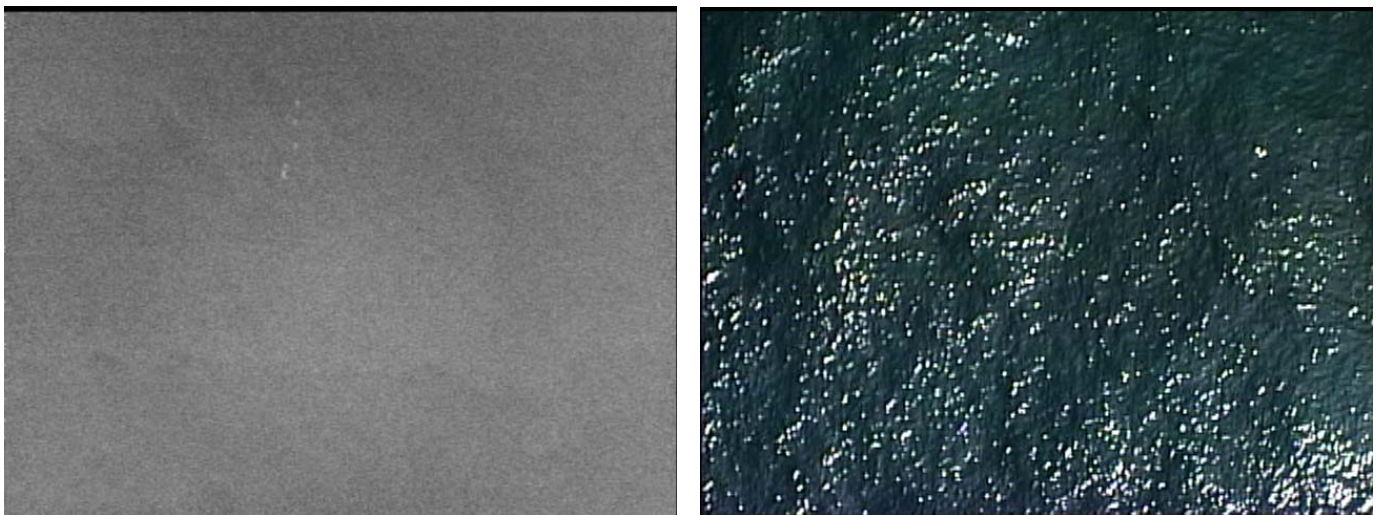
Figure 31 - IR (left) and RGB (right) images of birds floating in a line
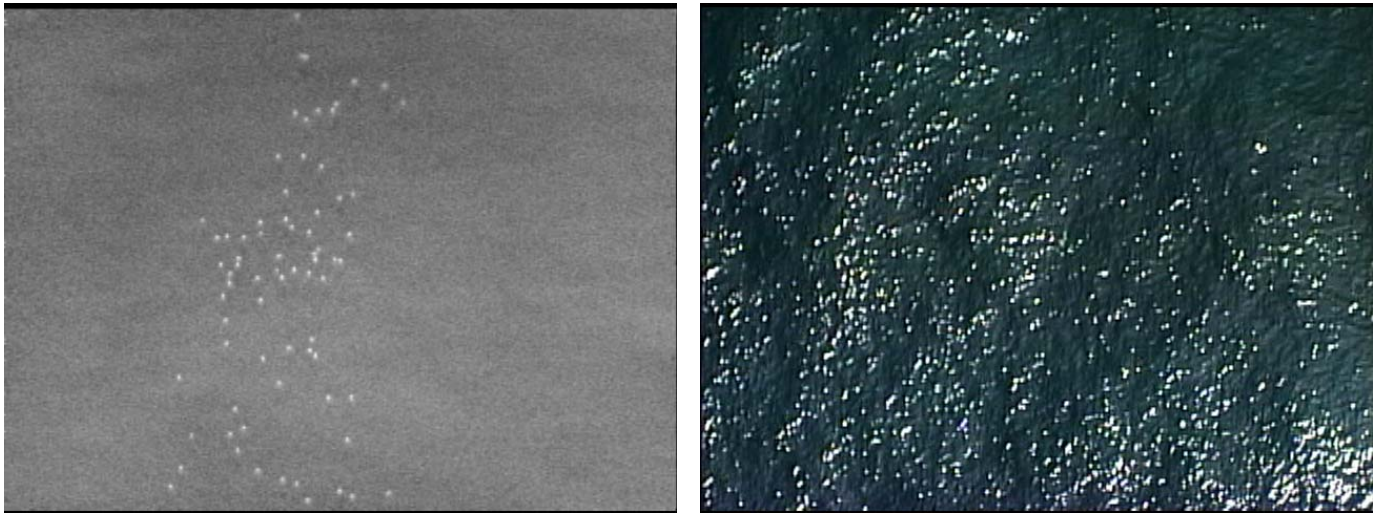
Figure 32 - IR and RGB images of a group of birds
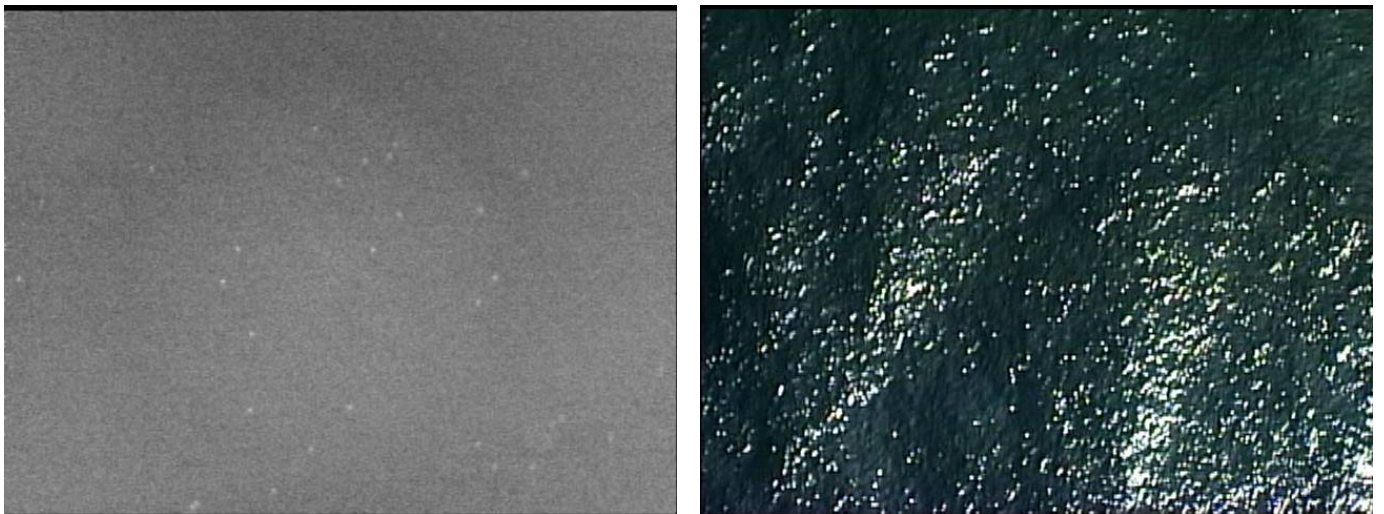
Figure 33 - IR and RGB images of scattered flock

Figure 34 - whales surfacing

Figure 35 - group of small birds on water
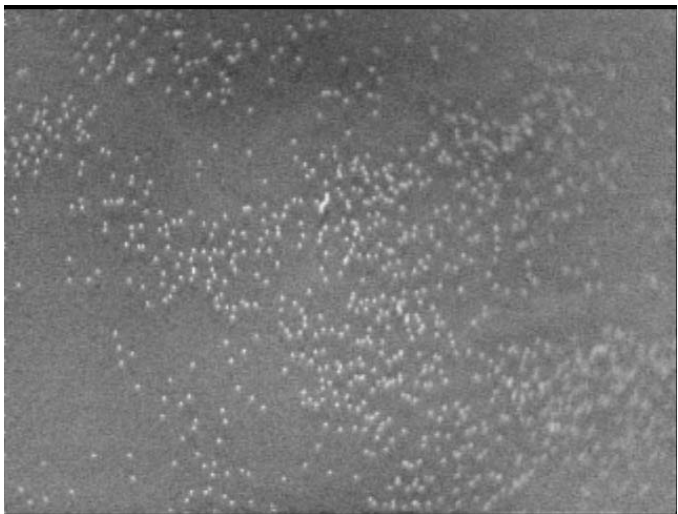
Figure 36 - large group of small and large birds on water

Figure 37 - variety of large and small birds moving at surface

Figure 38 - small and large birds on water and flying (unprocessed)

Here is an image that will be run through several adjustments to bring out the number, activity, and size of the birds present. The data isn't altered in any way during processing but enhanced to aid the eye in detecting and distinguishing anomalies.

Figure 39 - small and large birds on water and flying (inverted)

This is an inverted image of the original. As you can see, not only are the dots characteristic of size, but the larger birds are very dark while the smaller birds are shades lighter. Also, whether it be sitting, flying, taking off, the birds activity is fairly easy to determine from the picture. (streaks – birds taking off, dots – birds sitting in the water, etc…)
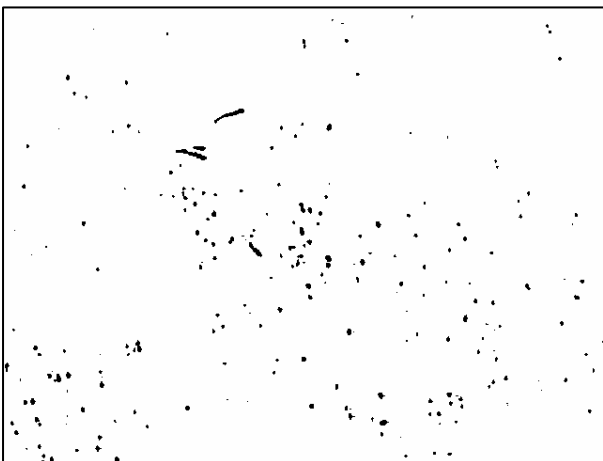
Figure 40 - small and large birds on water and flying (inverted & threshold)

The threshold was then taken from the previous image to achieve a black and white image. The threshold and be adjusted to display pixels that where more or less saturated depending on how sensitive of an image the processor desires.
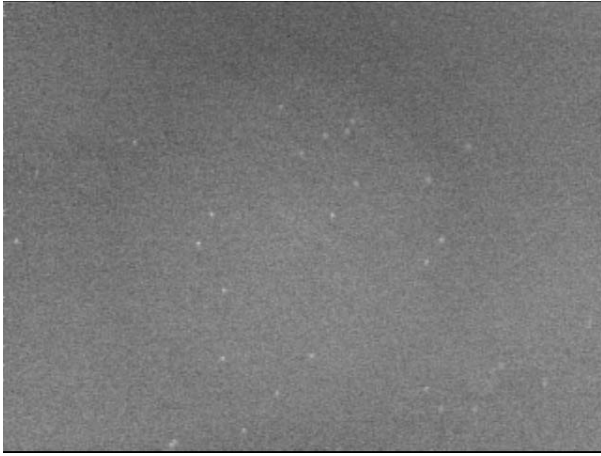
Figure 41 - scattered birds
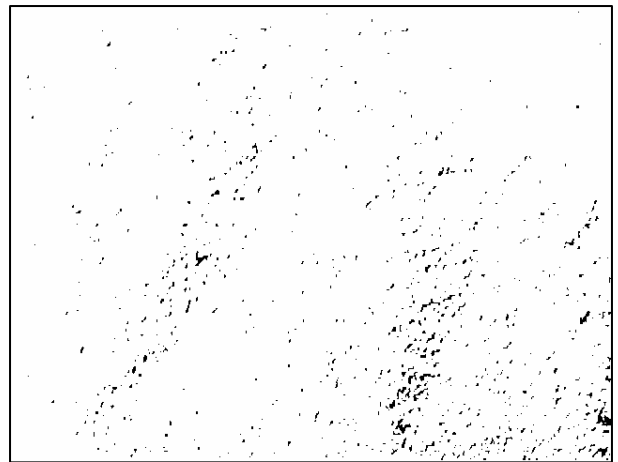
Figure 42 - Threshold of scattered birds with high visual saturation.

Here is an example of how visual (RGB) images can be totally saturated with reflected sunlight that detection of birds without the thermal camera would impossible.
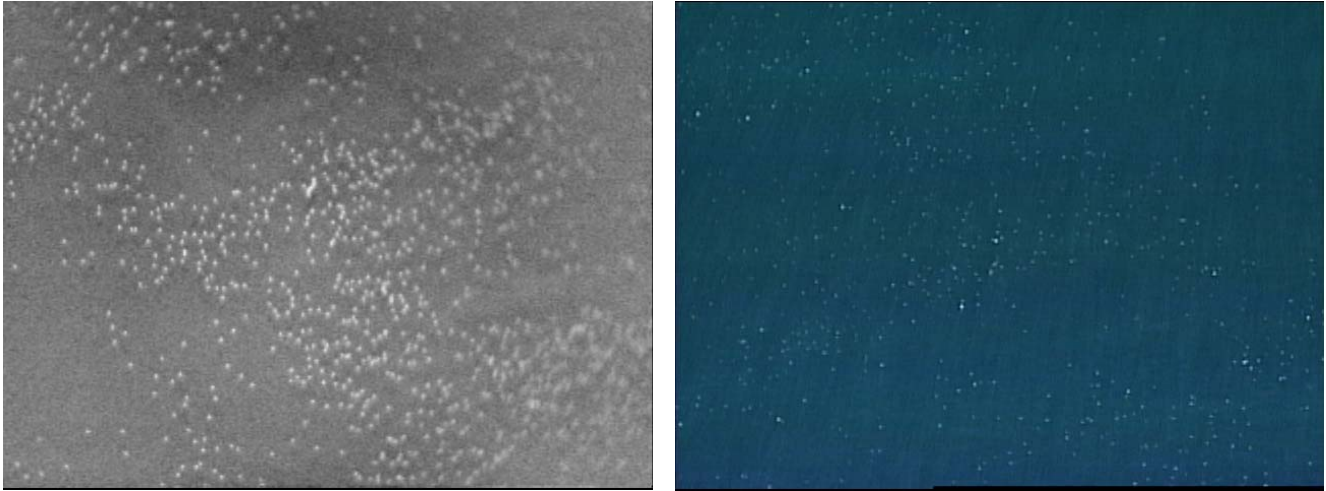
Figure 43 - large group of small birds

On May 21, surveys were flown synoptic with bird observers in skiffs. We were in constant radio contact to document the exact flyover times in order to line up bird counts afterwards.

In this data set, frames are in synch, but may not perfectly overlay the exact area. For example the IR camera may be focused for a range of 990 meters while the RGB camera is focused for infinity.

  Validation Areas (locations of features identified by a skiff crew) are outlined as:
       Bird Ball GMT 2222
       Cape Chiniak GMT 2250
       Fish schools and surface feeding birds GMT 2330
       Directly over skiff GMT 2343
        Directly over skiff GMT 2347
       Whales and shearwaters GMT 0003

Figure shows the cumulative flight path over the Validation Areas. It is easy to see the targeted area for several passes are made over most of the targets. Images of the features are shown. Images and features were logged to spread sheets including time and location stamps.

Although the processing of the combined data sets was beyond the scope of the project, we were hopeful that we could acquire additional funds to produce image identification error estimates and to experiment with additional camera resolutions and survey altitudes. The additional project was not funded, however the data remains in spreadsheets and a GIS database. We are hopeful that we can continue to work and complete the study in the future.

Figure 44. Cumulative flight path flown in coordination with sea bird researchers for the purpose of creating a video – image training set to explore the use of airborne imaging for sea bird mapping.
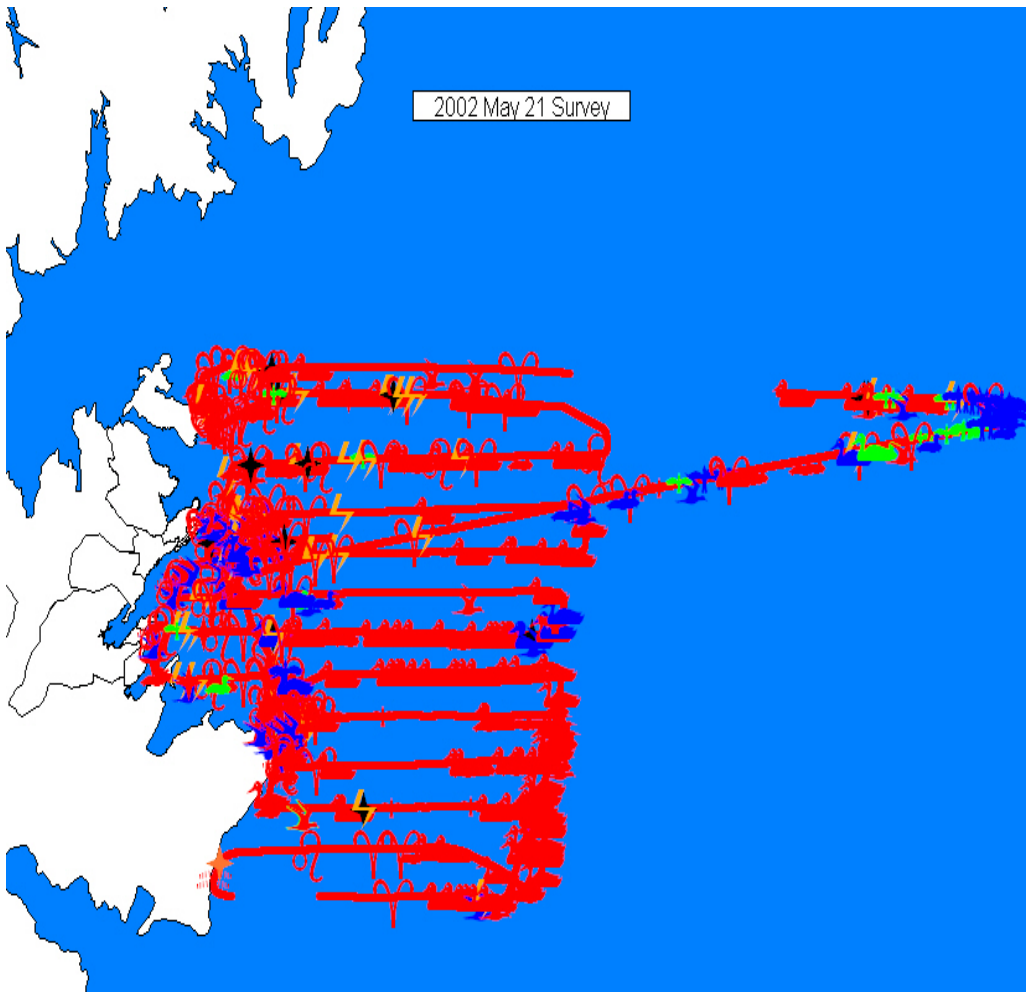
Figure 45
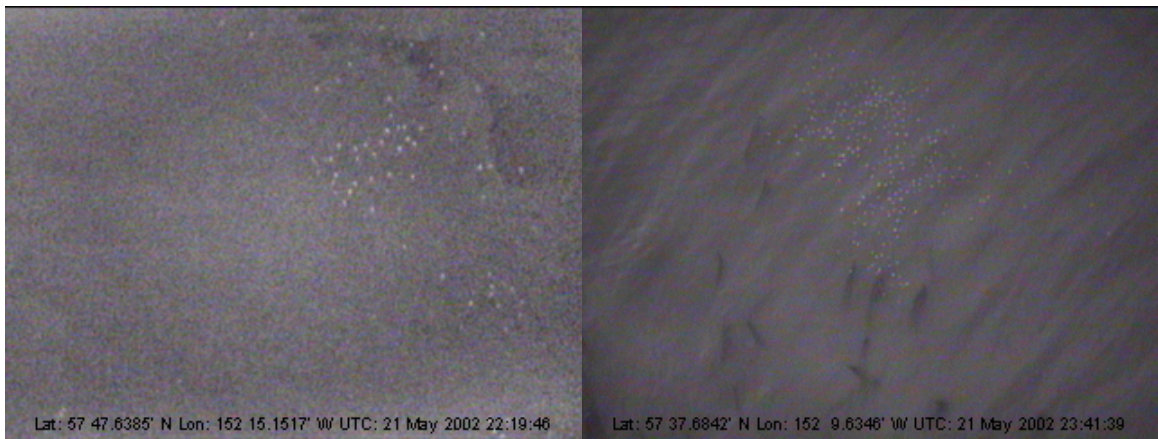
Figure 46
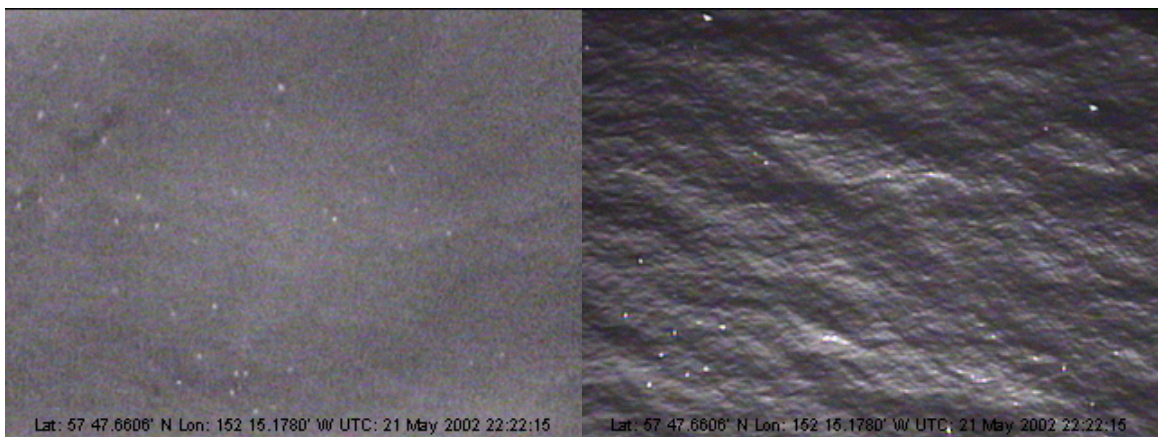
Figure 47

Figure 48

Figure 49
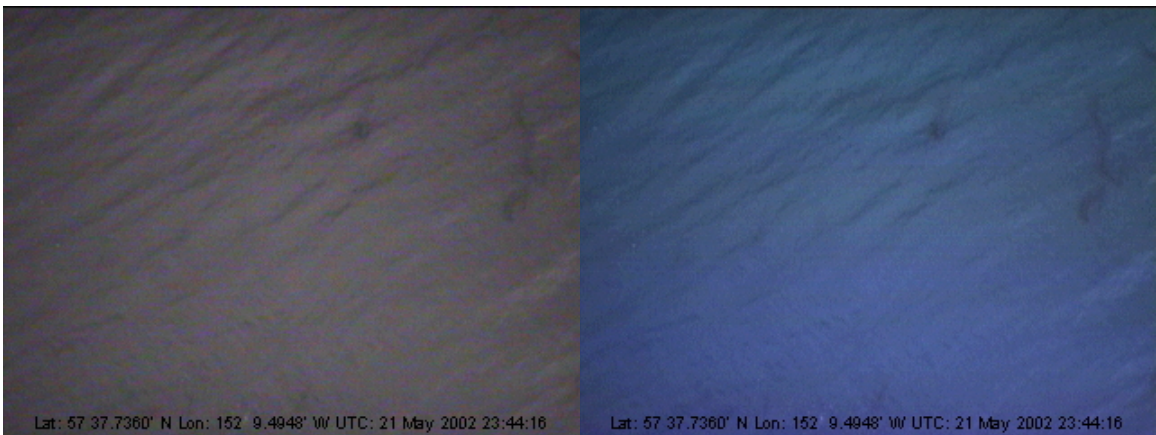
Figure 50

Figure 51

A new feature for this project was the experimentation with the gated video during the second year of the study, 2002. Synced with the lidar, we were able to capture some imagery of features but had difficulty in identifying the targets without some ship board observations. However, we captured a school of pink salmon, identified by a fishing vessel working below us, in the video (Figure 52). The fish were not visible with the naked eye. The gated video was unreliable during our surveys in 2002 simply because we were constantly adjusting settings to make it work. By the end of the study, we identified the problems including technical issues to be resolved in the laboratory concerning electronic control. We concluded that this technology is especially valuable in areas with a specific species or structure that is present (e.g. herring or salmon surveys) and images can be used to confirm that structures identified as fish schools are fish and not some other structure. Images could also be used to estimate the size of the fish captured by lidar backscatter and thus for expansion of signal to meaningful indices of biomass or abundance.

Figure 52. Image from a video gated synced to the pulses of the lidar (top); shown here is a school of pink samon approximately 5 m below the surface. The bottom image is true color (visual) of the same body of water; the green glint is from the laser spot.
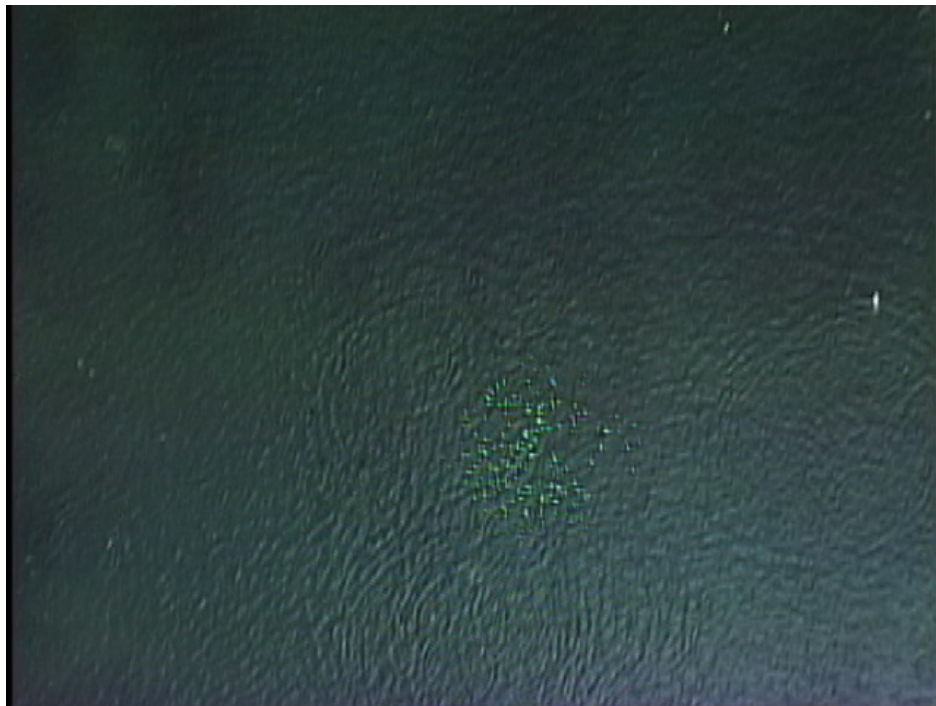
Finally, we show an example of the thermal data collected with the thermal infrared imager of consequence to marine mammals studies. Figure 53 shows the thermal pattern visible in the surface water following the traverse of a whale. Although we have not matched the species identifications with the georeferenced data, this whale was either a grey or a humpback whale. These patterns have never previously been observed. Therefore the ability to map marine mammal distribution and movements, using this type of information, is ground-breaking science. We are currently developing pattern recognition software to enable us to identify and map the patterns observed in the dataset.

Figure 53. The thermal pattern left in surface waters following the traverse of a baleen whale, in this case either a grey or humpback whale).
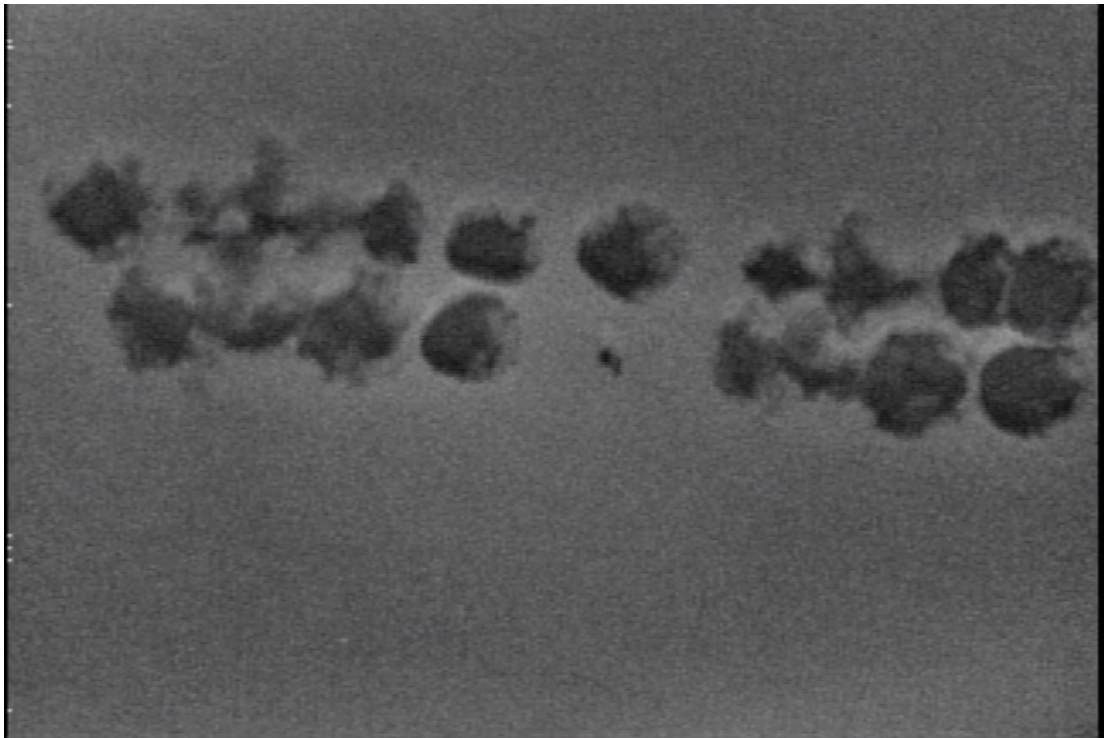
In this report, we have demonstrated the value of airborne data collection for mapping distribution, density and abundance of phytoplankton, zooplankton, fish schools, and surface feeding apex predators. We have demonstrated that this information can be collected synoptic with physical environmental data and that biological distributions can be meaningfully related to the physics exclusively collected from airborne platforms. However, the real value lies in the potential to explore larger spatial scales and at higher temporal resolutions than is physically possible aboard ships or from satellites. In an extreme subarctic environment such as the GOA, storm-induced variability and short-term (1-5 d) variation in primary and secondary production is the rule rather than the exception. Although valuable, satellite data is only partially useful because of days with cloud cover and the gap between orbital paths over a given region.

The cost of aircraft, fuel, personnel time and data processing costs (approximated at 3:1 processing time to data collection) was approximately $1400 per hour for this study. At a typical survey speed of 125 knots, the cost of data collection per km is $5.20. A typical ship survey including vessel and scientific crew costs and excluding data processing costs is $15,000 per day. Given a 12 hr work day and average data collection speed over the period of 6 knots, the cost of data collection per km is estimated at $112.5. The economy of airborne data is obvious.

It is not suggested that airborne survey techniques replace ship surveys, but rather be used to expand studies, especially of processes occurring in the upper 50 m of the ocean. In subarctic waters, this is the most productive region. Airborne methods would be especially useful in exploring processes with high short-term variability, such as primary and secondary ocean production, in increasing the probability of detection of ephemeral events, such as apex predator foraging bouts, and in expanding the spatial coverage of ocean surveys. In combination with a vertically profiling camera system, lidar-ship data could accurately map key plankton communities and structure without disturbance, an unfortunate occurrence with net sampling. We are just beginning to understand the importance of key plankton assemblages and their distribution to the maintenance of forage fish populations and ecosystem health. Airborne methods are also valuable in shallow regions with limited access to ships. Nearshore regions house thousands of tons of forage species such as sand lance, herring, spawning capelin and other juvenile fishes, yet these areas are often overlooked because of accessibility issues. The greatest value would be realized with combined airborne-ship surveys that extract and use the strengths and downplay the weaknesses of each platform. Of particular use for GEM would be regularly scheduled surveys with increased frequency during highly productive periods (spring and summer) over established transects, such as the Seward Line bisecting the GOA and along the Alaska Coastal Current. With multiple instruments, physics (SST, ocean color and salinity) can be collected synoptic to measurements of fish and plankton density, vertical structure, spatial patchiness, and horizontal extent. In addition, counts of sea birds and marine mammals can be extracted without bias from thermal imaging. Data processing and web posting could be standardized and completed in near real times. However, an additional pilot study is needed to estimate image processing errors in sea

bird counts and species identification. A small amount of additional data is needed to compliment the data we have on hand; this pilot study would be necessary to recommend detailed camera settings, data collection altitude, and post-processing automation techniques.

We have merely "scratched the surface" of possibilities for data collection and marine science inquiry using these techniques and the data we have collected. We continue to analyze and publish work resulting from the two years of data collection from this study. Our data has been archived and could be of use for future investigations, data sharing and collective analyses. It is our hope this can be accomplished.

References Cited

Churnside, J.H., J.J. Wilson, and V.V. Tatarskii. 1997. Lidar profiles of fish schools. Applied Optic 36(24): 6011-6020.

Churnside, J. H., V. V. Tatarskii, and J. J. Wilson. 1998. Oceanic attenuation coefficients and signal fluctuations measured from a ship in the Southern California Bight, Applied Optics 37: 3105-3112.

Churnside, J.H., J.J. Wilson, and V.V. Tatarskii. 2001. An airborne lidar for fisheries applications. Optical Engineering 40 (3): 406-414.

Cliff, A.D. and J.K. Ord. 1981. Spatial processes: models and applications. Pion Limited, London.

Geary, R.C. 1954. The contiguity ratio and statistical mapping. The Incorporated Statistician 5: 115-145.

Hoge, F.E., R.E. Berry, and R.N. Swift. 1986. Active-passive airborne ocean color measurement. 1: Instrumentation. Applied Optics 25: 39-47.

Hunter, J.R. and J.M. Churnside. 1995. Airborne fishery assessment technology: a NOAA workshop report. NOAA Southwest Fisheries Science Center Administrative Report, La Jolla, California, LJ-95-02. 71 pp.

Hunter, J.R. and J.H. Churnside. 1998. An evaluation of the potential use of airborne lidar for inventorying epipelagic fish schools. Extended abstract, page 43 in American Fisheries Society 128th Annual Meeting Abstracts, Hartford, Conn.

Krekova, M.M., G.M. Krekov, I.V. Samkhvalov, and V.S. Shamanaev. 1994. Numerical evaluation of the possibilities of remote laser sensing of fish schools. Applied Optics 33(24): 5715-5720.

Lo, N.C.H., J.R. Hunter, J.H. Churnside. 1999. Modeling properties of airborne lidar surveys for epipelagic fish. Administrative Report No. LJ-99-01, NMFS, Southwest Fisheries Science Center, La Jolla, CA (in submission process for formal publication).

Squire Jr., J.L. and H. Krumboltz. 1981. Profiling pelagic fish schools using airborne optical lasers and other remote sensing techniques. Mar. Tech. Soc. J. 15(4): 27-31.

Zorn, H. M., J. H. Churnside, and C. W. Oliver (2000), "Laser Safety Thresholds for Cetaceans and Pinnipeds," Marine Mammal Sci. 16, 186-200.

Appendix I. Estimating phytoplankton biomass in coastal waters of Alaska using airborne remote sensing

Martín A. Montes-Hugo[a,*], Kendall Carder[a], Evelyn Brown[b], Robert J. Foy[c], Jennifer Cannizaro[a], Scott Pegau[d]

[b]*Institute of Marine Science, University of Alaska Fairbanks, School of Fisheries and Ocean Sciences, Fairbanks, AK 99775-7220*

[c]*Fishery Industrial Technology Center, School of Fisheries and Ocean Sciences, University of Alaska Fairbanks, AK 99615-7401*

[d]*Kachemak Bay Research Reserve, Homer, NOAA, AK 99603*

[a, *] Corresponding author: EOS lab, College of Marine Science, University of South Florida, 140 7th Ave S, St. Petersburg, FL 33701, USA, Phone: 727-553-3952 Fax: 1-727-5533918; E-mail address: mmontes@mail.usf.edu.

Abstract

Empirical airborne remote-sensing relationships were examined to estimate chlorophyll <u>a</u> concentration in the upper mixed layer (chl_{FOD}) of coastal waters of Afgonak/Kodiak Islands during July-August 2002. Band-ratio and spectral-curvature models were tested using satellite remote-sensing reflectance ($R_{rs}(\lambda)$) measurements. Additional shipboard and airborne $R_{rs}(\lambda)$ data were also analysed to evaluate consistency of proposed chl_{FOD}-$R_{rs}(\lambda)$ relationships. Validation of chlorophyll algorithms was performed using data collected in the northern-part of the Gulf of Alaska and Bering Sea during 1996, 2002, and 2003 cruises. Likewise, oceanographic conditions during the surveys were typified to interpret variability of chl_{FOD} fields. The SeaWiFS band-ratio algorithm OC2d was the most sensitive R_{rs} combination ($R_{rs}(509)/R_{rs}(553)$) to detect chl_{FOD} variability. No valid statistical regressions were established for band-ratio or spectral-curvature relationships in the blue spectrum (<500 nm). Fertile waters (>5 mg m^{-3}) were preferentially located over shallow banks (~50 m) and the entrance of the bays. The approach used in this study to derive chl_{FOD} values could be universal for Alaskan coastal waters. However, chl_{FOD}-$R_{rs}(\lambda)$ relationships must be calibrated locally for a given season.

71

1. Introduction

In the last five years, the northern part of the Gulf of Alaska (NGOA) has been the focus of several scientific projects (e.g. FOCI-National Oceanographic and Atmospheric Administration, APEX-University of Alaska) interested in understanding the causes of decline of Steller Sea Lion populations (Loughlin et al., 2000; Winne & Foy, 2002). Nutritional stress caused by climate variability is one of the most important factors explaining such decline firstly detected 30-years ago (Winne & Foy, 2002). Since prey availability for Steller sea lions is linked to phytoplankton biomass (B) distributions (Hirons et al., 2001), monitoring of B represents a fundamental tool to figure out changes on sea lions dynamics under different environmental conditions.

In NGOA waters, global spatial patterns of chlorophyll $\underline{a}$ concentration (chl), a B proxy, have been studied using standard satellite algorithms (Gregg, 2002; Brickley & Thomas, 2004). However, these algorithms cannot detect small-scale (<1 km) variations of chl, and near the coast they fail to accurately estimate chl values due to land proximity (Reinersman & Carder, 1995) and bottom radiance contributions (Lee et al., 2001). Synoptic chl mapping using ship surveys has not been feasible in shelf waters of NGOA due to the dynamic conditions (e.g. strong winds, long-shore transport) (Stabeno et al., 2004) and restricted access to shallow areas (Brown et al., 2002). The use of airborne remote-sensing (Lee et al., 2001; Brown et al., 2002) provides a possible solution to estimate small-scale horizontal distributions (~0.1 km) of chlorophyll values under fluctuating conditions such as the NGOA. Aerial surveys allow synoptic views, are faster and less expensive than ship cruises (Brown et al., 2002), and unlike satellites, flights can be scheduled at various times per day to accommodate tidal and meteorological

conditions. Also, atmospheric correction of radiance measured aboard the planes (~300-1000 m above sea surface) is straightforward and minor (greater signal/noise) compared to that used with satellite platforms (Hu et al., 2000). In spite of their advantages, all color remote-sensing instruments retrieve only chl values from the first optical depth ($z = 1$/beam attenuation coefficient) due to the exponential signal decrease with depth (IOCCG, 2000). Multiple factors affect the spatial distribution of chl over the NGOA shelf and change during the year (e.g. nutrient availability, zooplankton grazing) (Stabeno et al., 2004; Brickley & Thomas, 2004). During spring and summer, high chl values (>10 mg m^{-3}) are still observed from Cook Inlet southward around Kodiak Island and out to the shelf break (Sambrotto & Lorenzen, 1987; Stabeno et al., 2004). Additional nutrients supplied by various mechanisms (e.g. tidal mixing) have been suggested as the main controlling factor for productivity (Stabeno et al., 2004). However, the effect of different water transparencies on horizontal chl distributions during summer has not yet been explored.

The aim of the present study was to estimate chl values in the first optical depth (chl$_{FOD}$) of coastal waters of NGOA using high-resolution airborne data. The final intention is to investigate relationships between small-scale B distributions, oceanographic features (e.g. fronts), and foraging areas of Steller sea lions. Two hypotheses are tested: (1) chl algorithms using longer wavelengths will perform better to estimate B, (2) areas with largest B will coincide with intermediate environmental conditions (mixing, nutrients, light). Airborne spectral upwelling radiances and downwelling PAR (photosynthetically available radiation) irradiance (400-700 nm) data were gathered over waters of the eastern shelf of Afgonak/Kodiak Islands during summer

(July-August) of 2002. Performance of band-ratio and spectral curvature R_{rs} algorithms to retrieve chl values was evaluated with simultaneous measurements of chl and remote-sensing reflectance (R_{rs}) data. Oceanographic surveys of environmental variables (e.g. temperature, water transparency) were coordinated with aerials missions.

2. Methods

2.1. Atmospheric correction

Remote-sensing measurements from airplanes usually do not require extensive atmospheric path-radiance corrections unless airborne spectra are obtained from relative high altitudes (e.g. >3 km for Airborne visible Infrared Imaging Spectrometer) (Lee et al., 2001). In this work, total radiance above-water measurements at each wavelength ($L_t (\lambda)$) were first selected according to cloud-free conditions by interpolation of downwelling irradiance above sea-surface values (E_d^+) obtained during each flight. Fog-contaminated pixels of the original scene were also removed based on visual inspection of data collected during flights. A quasi-single-scattering approximation was suggested (Rayleigh-aerosol multiple scattering ignored) to relate water-leaving radiance (L_w) to L_t (Gordon et al., 1983):

$$L_t (\lambda) = L_r (\lambda) + L_a (\lambda) + t (\lambda) L_w (\lambda) \tag{1}$$

where $t (\lambda)$ is diffuse transmittance of the atmosphere, and L_r and L_a are Rayleigh and aerosol radiances computed as follows:

$$L_x(\lambda) = [\omega_x(\lambda)\, \tau_x(\lambda)\, F'_o(\lambda)\, p_x(\theta,\theta_o,\lambda)]/4\pi \tag{2}$$

$$p_r(\theta,\theta_o ,\lambda) = \{P_r (\theta_-,\lambda)+[\rho(\theta)+\rho(\theta_o)]\, P_r(\theta_+,\lambda)\}/\cos\theta \tag{3}$$

$$\cos\theta_\pm = \pm \cos\theta_o \cos\theta +\sin\theta_o \sin\theta \cos(\phi-\phi_o) \tag{4}$$

74

$$P_r (\theta_\pm, \lambda) = \frac{3}{4} [1 + \cos^2\theta_\pm] \qquad\qquad (5)$$

where x is Rayleigh (r) or aerosol (a), ω_x is the single-scattering albedo ($\omega_a = 1$), θ_o and

ϕ_o are the solar zenith and azimuth angles, θ and ϕ are the zenith and azimuth angles of a

vector from the point of the sea-surface to the sensor, P_r is the Rayleigh phase function,

and $\rho(\theta)$ is the Fresnel reflectance. Skylight reflectance effects were accounted with a

first-order adjustment by subtracting L_{780} to $L_t (\lambda)$ in equation (1) (Lee et al., 2001).

Rayleigh optical thickness (τ_r) interpolated between 0 and 1 km was provided by

Elterman (1968) tables. Since the aircraft was flying well below the ozone layer, $t (\lambda)$

was calculated considering an aerosol transmittance equal to 1 (Gordon & Clark, 1980).

Path-radiance due to aerosol scattering was calculated over clear-water pixels where a

minimum water-leaving radiance at 665 nm is expected ($L_a^o = L_t^o (665) - L_r^o (665)$).

Contribution of aerosol scattering to $L_t (\lambda)$ was then estimated:

$$L_a (\lambda) = S (\lambda_i, \lambda_{665}) L_a^o \qquad\qquad (6)$$

where $\lambda_i = 411, 443, 491, 509, 553$, and $\lambda_o = 665$ nm.

$$S (\lambda_i, \lambda_{665}) = \varepsilon (\lambda) F'_o (\lambda)/F'_o(665) \qquad\qquad (7)$$

A value of $\varepsilon (\lambda) = 1$ was assumed in this study as a first-order correction

applicable to maritime atmospheres as in standard Coastal Zone Color Scanner (CZCS)

processing (Gordon et al., 1983). $F'_o(\lambda)$ is equal to the instantaneous extraterrestrial solar

irradiance $F_o (\lambda)$ (ozone optical thickness = 0). Values of $F_o(\lambda)$ were obtained from

Neckel & Labs (1984) tables. Aerosol horizontal distribution over the aerial transects was

estimated from values of aerosol optical thickness at 865 nm (τ_{865}) obtained from Sea-viewing Wide Field-of-view Sensor (SeaWiFS) images during the period studied.

2.2. Empirical airborne methods for deriving chl from remote-sensing measurements

Similar to satellite-borne sensors, development of airborne empirical chl models is still on-going (Harding et al., 1994; Sathyendranath et al., 2004). Airborne color algorithms remain basically comparable to those of satellite remote-sensing relationships since both types of remote-sensing platforms have been sharing almost the same spectral resolution, and in some cases even the same color channels (e.g. Daedalus spectrometer matches CZCS) (Perez-Ruzafa et al., 1996). Empirical satellite chl algorithms are based on nadir-normalized water-leaving radiance normalized (nL_w) and remote-sensing reflectance ($R_{rs}(\lambda) = L_w(\lambda)/E_d^+(\lambda)$) ratios (O'Reilly et al., 1998). Spectral-curvature or inflection-ratio chl algorithms have been used without atmospheric correction at low aircraft altitudes since the 80's (e.g. Campbell & Esaias, 1983). These models are very sensitive to curvature changes (G) of R_{rs} around a centered wavelength λ_i (e.g. 490 nm):

$$G_{m, n}(\lambda_i) = S(\lambda_i)^2/S(\lambda_i - m) S(\lambda_i + n) \qquad (8)$$

where S is the remotely-sensed water property (e.g. R_{rs}).

Although G and band-ratio algorithms may cover a wide range of field chl (0.1-10 mg m^{-3}) values (Campbell & Esaias, 1983; Gordon & Morel, 1983), performance of these empirical algorithms may be deteriorated in Case II waters (i.e. those waters where inherent optical properties are also dominated by constituents such gelbstoff) (Campbell & Esaias, 1983; Sathyendranath et al., 2004). In this work, performance of four cubic-polynomial band-ratio (OC2a = $R_{rs}(412)/R_{rs}(553)$, OC2b = $R_{rs}(443)/R_{rs}(553)$, OC2 =

$R_{rs}(491)/ R_{rs}(553)$, OC2d = $R_{rs}(509)/ R_{rs}(553)$) (O'Reilly et al., 1998), and one spectral-curvature ($G_{1,1}(491) = R_{rs}(491)^2/(R_{rs}(443) R_{rs}(509))$ models (Campbell & Esaias, 1983) were tested to estimate chl_{FOD} values in NGOA waters. According to the literature (Grew, 1980; O'Reilly et al., 1998), selected chl algorithms were the most reliable as global indicators of chl.

2.3. Field measurements

The East side of Afgonak/Kodiak Islands shelf is characterized by having several bays and islands (Fig. 1a). The southern branch of the Alaska Coastal Current is flowing southward along the eastern Afgonak/Kodiak Islands shelf. This onshore current, forced by northerly freshwater inputs and wind forcing, is relatively weak and with many meanders (Stabeno et al., 2004). Kodiak environments have been historically more productive than other NGOA regions, even during summer conditions when higher water turbidity caused by freshwater plumes is expected (Sambrotto & Lorenzen, 1987; Stabeno et al., 2004). Likewise during summer, shelf waters around Afgonak/Kodiak Islands present a strong thermocline, which limits the vertical flux of nutrients even though several nutrient-enrichment processes have been identified (e.g. upwelling due to bathymetric effects and mixing) (Stabeno et al., 2004).

Aerial surveys of $L_t (\lambda)$ and $E_d (\lambda)$ were effectuated during 27-28 July, and 17 August 2002 on the eastern shelves of the Afgonak/Kodiak Islands (Fig. 1b). Airborne sampling lines were designated to cover a number of different water masses/features including shallow banks, troughs and areas with small islands. Surveys during July were complementary while August transects overlapped July ones circa 58° N to the south. More intense flight measurements were carried out in Marmot Bay around Whale Island

due to the relatively elevated productivity of these waters (Dr. Robert Foy, person. comm.). As suggested by Campbell & Esaias (1983), flight times were scheduled according to the sun's elevations between 20° and 50° to avoid sun glint. Measurements of $L_t(\lambda)$ and $E_d(\lambda)$ were performed at 411, 443, 491, 509, 553, 665, and 780 nm (10 nm bandwidth) with a spectrometer OCR-507-R03A and OCR-507-ICSA, respectively (MicroSAS, Satlantic, Canada). At 300 m altitude (average height during flights), field of view of the radiance sensor (28° in air) allowed across track data collections with a maximum spatial resolution of 72.5 m. This corresponded also with the minimum pixel size since the radiance detector was positioned with a zero zenith angle. Although the MicroSAS sampling rate was 6 data (7 channels) per second and every 6.5 m (along track distance), original radiometric readings were binned every 200 m (~ 3 s) by averaging. Geo-located radiance and irradiance data were corrected for pitch, roll and height for each flight.

Preliminary results showed that chl field measurements matching R_{rs} data during aerial surveys were insufficient, thus shipboard and satellite R_{rs} data were additionally analyzed. Field surveys for testing chl remote-sensing algorithms were carried out during 14-16, 19-29 July, 16-18 August 2002 (FOY dataset), and 1-21 May, 21 July-12 August 2003 (PEGAU dataset) (Fig. 1c). FOY and PEGAU chlorophyll concentrations were matched with satellite reflectance spectra (SeaWiFS) within three hours of the satellite pass. L2 imagery products (R_{rs} at 412, 443, 490, 510, and 555 nm) were obtained from DAAC (http://daac.gsfc.nasa.gov) and processed using a 5 x 5 mask with SEADAS 4.6 software. Further validation of selected chl remote-sensing algorithm was effectuated with *in situ* R_{rs} and chl data obtained in Bering Sea during 18-19, 21-28 April 1996

(CARDER dataset). Briefly, *in situ* upwelling radiance and sky radiance spectra were measured 90° from the solar plane and 30° from nadir and zenith, respectively (Lee et al., 1996). Values of E_d^+ were computed:

$$E_d^+ = \pi L_G/R_G \qquad\qquad (9)$$

Measurements of $L_G (\lambda)$ were made perpendicular to the graycard reflector, and $R_G (\lambda)$ is the reflectance of the graycard reflector. All measurements were performed using a custom-made, 512-channel spectroradiometer (~350-850 nm; ~25 nm resolution) (Lee et al., 1996). Calculating the water leaving radiance is more difficult since measurements of L_t must be corrected for reflected sky radiance (L_{sky}) and possible solar glint. Water leaving radiance spectra were calculated as:

$$L_w = L_t -(\rho(\theta) L_{sky} + \Delta) \qquad\qquad (10)$$

Where Δ is a solar glint correction derived assuming $R_{rs} (750)$ equal to zero. Scans with anomalously high $L_t (750)$ values were omitted to minimize glint effects. Multiple measurements were taken of L_t, L_G, and L_{sky}.

Only for FOY stations, vertical profiles of chl, PAR, temperature, salinity were made. Sampling lasted from 10:00 to 15:00 h daily, and had an average working period per station of 30 minutes. For each R_{rs}-chl comparison, every chl_{FOD} was the average of chl samples between zero and the first attenuation depth (~7 m, ~90 % of L_w is originated at that depth). Pigment concentration was determined by fluorescence after extraction with acetone 90% (Venrick & Hayward, 1984). Surface and underwater downward PAR was determined with a light-meter LI-COR (LI-190SB, LI-192SB) (precision: ± 5% as quoted by the manufacturer – LiCor Inc., Lincoln, Nebraska). PAR transmission was

calculated within the upper mixed layer as the ratio between PAR values measured at 20

and 0 m (T_{20}). Integrated chl within the euphotic zone (B_{EU}) was obtained by trapezoidal

integration between zero and the euphotic depth (z at which PAR equal 1% of surface

PAR). Daily L3 coastal wind data (25 km resolution, SeaWinds sensor,

http://podaac.jpl.nasa.gov) were used to interpret aerosol origins, and modeled chl

distributions. In coastal waters influenced by freshwater inputs, gelbstoff is inversely

related to salinity (Blough et al., 1993). Hence, the potential effect of gelbstoff on chl

variability was assessed using surface salinity fields during each flight track. Likewise, a

numerical filter originally proposed for satellite data was applied to airborne R_{rs} (λ) ratios

to identify gelbstoff-rich waters over the study area (Carder et al., 1999):

$$R_{rs} (412)/R_{rs} (443) = 0.95 \left[R_{rs} (443)/R_{rs} (553) \right]^{0.16} \qquad (11)$$

Original MODIS wavelengths are slightly different from MICROSAS

wavelengths (e.g. 551 nm instead of 553 nm) even though these differences (~2 nm) may

be considered negligible (O'Reilly et al., 1998). Airborne R_{rs} (λ) ratios falling below the

case I water (i.e. phytoplankton and its metabolic products dominate water optical

properties) relationship (11) indicate high-gelbstoff data points. Notice that filter (11)

also provides a space-based method to separate data points with packaged pigments

(points below case I curve) from those with unpackaged pigments. Pigment-package

effect is manifested as a flattening on phytoplankton absorption peaks with increasing

intracellular pigment concentration due to shelf-shading (Morel & Bricaud, 1981). To

quantify the influence of bottom depth on nL_w and R_{rs} spectra measurements and

describe ecologic effects of hydrographic features on chl distributions, high-resolution

bathymetry (~8.3 km) around Afgonak/Kodiak Islands (Pacific Marine Environmental

Laboratory, Hermann et al., 2002) was analyzed. High-resolution coastline (~0.2 km) was obtained by plotting closed polygons of Global Self-consistent hierarchical shoreline database (Wessel & Smith, 1996). Water column mixing was estimated based on vertical density differences measured between surface and pycnocline depth ($d\rho$). Water level data relative to the mean low level water (MLLW) was obtained from Sand Point tidal prediction station in Kodiak Island (NOAA/NOS, http://co-ops.nos.noaa.gov). Tide show to be mixed, with a dominant semidiurnal component and maximum amplitude of 2.5 m.

2.4. Statistical analysis

Band-ratio and spectral-curvature relationships were log-transformed, and their performance to estimate chl_{FOD} was compared using the root mean square error in log_{10} scale of quantity between N derived and true values (O'Reilly et al., 1998):

$$RMSE_{log10} = \{\sum [log_{10} (q_n^{der})-log_{10} (q_n^{true})]^2 /N\}^{.5} \qquad (12)$$

The linear percentage error for q_n (chl_{FOD}) models placing equal emphasis on underestimates as well as on overestimates and is computed as:

$$\varepsilon_{rr} = 0.5*[(10^{RMSElog10}-1)+(1-10^{RMSElog10})] \qquad (13)$$

Likewise, goodness of fitting of spectral-curvature models was evaluated using linear regression of log-log R_{rs}-chl_{FOD} data (Sokal & Rohlf, 1995) as suggested by Campbell & Esaias (1983). Time series of estimated chl_{FOD} horizontal fields was obtained by kriging interpolation using Surfer 8.0 (Cressie, 1991).

3. Results

3.1. Airborne water leaving radiance and reflectance

Ambient light parameters, position and bottom depths encompassed during 2002 MICROSAS surveys are summarized in Table 1. North-central (27 July), southern (28

July), and south-central (17 August) aerial surveys covered a total of $5.34 \ 10^3 \ km^2$ (3,800 stations). Mean of water-leaving radiance at 665 nm in clear waters (57.84° N, -150° W) and for the whole period surveyed was 0.078 ± 0.0005 (L_t^o (665) = 0.131, L_r^o (665) = 0.0543). Values of $\tau 865$ were fairly constant throughout the airborne surveys (0.072 ± 0.006). Wind direction data from SeaWinds indicated a terrestrial/maritime origin of aerosols. Maximum nL_w (λ) values were observed at 491 nm and decreased greater towards shorter wavelengths (Table 2). Water-leaving radiance and remote-sensing reflectance were influenced by the intricate bathymetry of Afgonak/Kodiak shelves formed by a succession of troughs (> 200 m deep) and shallow banks (< 50 m) (Fig. 2). Some nL_w and R_{rs} spectra presented a maximum at 553 nm such those observed in very shallow waters (<30 m) (Fig. 2a). Highest (e.g. Stations A-C) values of R_{rs} were generally observed near the coast close to small islands (Fig. 2b). Notice in Figure 2a that the steepest slope between 411 and 491 nm corresponded to station F. With the exception of 665 nm channel, values of nL_w and R_{rs} values decreased for all MicroSAS channels from 27 July to 28 July, and increased again on 17 August (Table 2).

3.2. Chlorophyll models

Changes on R_{rs} (509)/R_{rs} (553) ratios explained the greatest variability ($RMSE_{log10}$ = 0.26, ε_{rr} = 0.64) observed in field chl_{FOD} data (chl_{FOD} range between 0.2 and 11 mg m^{-3}) as it is shown on figure 3 using log-log scale. Band-ratios relationships OC2a ($RMSE_{log10}$ = 0.41, ε_{rr} = 1.09), OC2b ($RMSE_{log10}$ = 0.29, ε_{rr} = 0.71), OC2 ($RMSE_{log10}$ = 0.33, ε_{rr} = 0.85) had a poorer performance to estimate chl_{FOD} respect with OC2d (Fig. 3a-c). There was not a significant regression between spectral-

curvature G (491) and chl$_{FOD}$ measurements ($P > 0.05$) (Fig. 3d). Further analysis

using additional *in situ* shipboard and airborne calibrated R$_{rs}$ values confirmed the

tighter relationship between R$_{rs}$(509)/R$_{rs}$(553) and chl$_{FOD}$ measurements (Fig. 4a).

Notice that figure 4 contains data for different years and obtained with diverse

sensors (e.g. airborne *vs* spaceborne) and atmospheric corrections schemes.

Regardless the dataset used, most of the chl points computed with OC2d were

underestimated compared to *in situ* pigment concentrations since modeled chl values

were located above the 1:1 chl$_{FOD}$ line (Fig. 4b). For the whole pool of chl$_{FOD}$-

R$_{rs}$(509)/R$_{rs}$(553) pairs (n = 56), $r^2 = 0.84$, RMSE$_{log10} = 0.20$, εrr = 0.48.

3.3. *Spatial distribution of estimated chlorophyll*

The band-ratio OC2d algorithm was the best-educated relationship to roughly

estimate chl$_{FOD}$ values in our study area between band-ratio and spectral-curvature

models tested. However, relatively high variability of estimated chl$_{FOD}$ values using

OC2d compromised calculation of absolute pigment concentrations with our dataset.

Thus, OC2d relationship was used instead to obtain an index of chl$_{FOD}$ during each flight

mission and for different areas of Afgonak/Kodiak shelves. Notice that the main goal of

this contribution was to identify areas potentially productive for Steller sea lion

populations and their connection to oceanographic variability. The development of local

chl algorithms in NGOA waters, and thus calculation of absolute chl values is outside the

scope of the present contribution.

Mean of chl$_{FOD}$ calculated from R$_{rs}$ (509)/R$_{rs}$ (553) values (chl$_{FODest}$) was 3.45

(se = 0.05, n = 1794), 2.68 (se = 0.08, n = 879), 4.44 (se = 0.09, n = 1928) for 27, 28 July

and 17 August 2002, respectively. In terms of regional trends, chl_{FODest} showed the lowest values in the northernmost stations of the time series (Fig. 5a). Mean of chl_{FODest} was significantly higher during 17 August than that calculated for 27-28 July (3.20 ± 0.04). On 27 July, high pigment patches (7-10 mg m^{-3}) developed preferentially over shallow waters of the central part of N. Albatross Bank and near Whale Island (Fig. 2b, Fig. 5a). An exception occurred near the southern coast of Afgonak Island over the Stevenson trough (~170 m). On 28 July, relatively high chl_{FODest} values (~10 mg m^{-3}) were again found over N. Albatross Bank. Likewise, high pigment concentrations were also detected along nearshore areas of Ugak Island and Chiniak Bay mouth (Fig. 5b).

On 17 August, chl_{FODest} values above 7 mg m^{-3} were widespread and distributed from the entrance of Marmot Bay to the entrance of Chiniak Bay (Fig. 5c). Similar to 28 July, rich chl waters were also present near Ugak Island and eastward of Chiniak Bay entrance over N. Albatross Bank. Notoriously, chl_{FODest} values up 20 mg m^{-3} were principally calculated east of Spruce Island (Fig. 5c). Overall for July-August surveys, relatively low chl_{FODest} values (~2 mg m^{-3}) were associated with Stevenson and Chiniak troughs.

3.4. Environmental ancillary information

Mean 0-2 m water temperature was higher in August (10.93 ± 0.32) than in July (9.31 ± 0.18) ship surveys. Warm waters (~11°C) were observed northeast of Marmot Island, Marmot Bay entrance, N. Albatross Bank, Chiniak trough, and northern inner part of Chiniak Bay (Fig. 6a). Minimum temperature values (~7.5 °C) were measured around and close to Marmot Island and the southern part of Perenosa Bay. Salinity values were

greater during July (31.90 ± 0.08) than August (31.55 ± 0.16) days. For July-August,

lowest salinity waters (~29.5) were located in the innermost part of Marmot Bay and

Chiniak Bay (Fig. 6b). Curiously, a low salinity patch (S = 31.5) surrounded by high

salinity waters (S = 32.0) was situated to the northeast of Marmot Island. Overall, water

column stratification was more significant in August ($\delta\rho = 0.31 \pm 0.04$) than in July

surveys ($\delta\rho = 0.22 \pm 0.03$). High $\delta\rho$ values ($\delta\rho > 0.6$) were generally found in relatively

deep waters (>150 m) such Stevenson trough and the middle part of Marmot Bay (Fig.

6c). Nevertheless, vertical mixing was also reduced near the coast such those areas

located in the innermost part of Marmot and Chiniak Bay. Homogenous water column

structure ($\delta\rho = 0$) was evident in shallow areas (<50 m) close to Marmot Island, Spruce

Island, Ugak Island and part of N. Albatross Bank. In general, airborne reflectance

measurements showed more rich-gelbstoff waters in July than in August (Fig. 7). Based

on equation (11), percentage of points with 'high-gelstoff/high-package effect' flagging

was 53, 74, and 41 % for 27, 28 July and 17 August, respectively. Water transparency

estimated from PAR transmission at 20 m did not vary in significant way between July

($T_{20} = 6.2 \pm 0.6$ %) and August ($T_{20} = 6.5 \pm 1.1$ %) stations. Lowest PAR attenuations

(up to 30 %) were characteristic over a bank extending northeast of Marmot Bay, the

southern part of Chiniak Bay entrance and a spot over N. Albatross Bank (Fig. 8a).

Interestingly, not always high PAR penetration stations ($T_{20} > 10\%$) corresponded with

troughs and in some cases intermediate T_{20} were measured in the innermost part of the

Bay (e.g. Marmot Bay). In most of the cases, there was a fair matching between chl_{FODest}

and B_{EU} values for the whole study area (Figs. 5 and 8b). Mean of B_{EU} during August

($B_{EU} = 164.49 \pm 8.51$ mg m^{-2}) decreased compared to that calculated during July ($B_{EU} = 238.97 \pm 9.08$ mg m^{-2}). Three high phytoplankton biomass areas showed up again over N. Albatross bank (>500 mg m^{-2}), along the entrance of Marmot Bay and Chiniak Bay (~400 mg m^{-2}), and northeast of Marmot Island over a trough (~250 mg m^{-2}). Low B_{EU} waters (~150 mg m^{-2}) were typical around Marmot Island, innermost part of Bays, and Stevenson trough. A clear mismatch between chl$_{FODest}$ and B_{EU} was evident in the southern part of Afgonak Island between Marmot Island and Marmot Bay entrance (Figs. 5a and 8c).

4. Discussion

Steller sea lions populations of NGOA, now considered endangered species, have exhibited the most pronounced decline in Afgonak/Kodiak shelves since the 70's (Angliss et al., 2001). In the same region, Logerwell et al. (2003) suggested that one of the most important factors of such decline (prey availability) seems to be determined by chl patchiness. In this study, high-resolution airborne R$_{rs}$ data was used to estimate chl patchiness over coastal waters of Afgonak/Kodiak Islands during summer of 2002. The ratio R$_{rs}$ (509)/R$_{rs}$ (553) was the best index of B levels in surface waters of NGOA waters. The success of OC2d in our study may be related to the importance of phytoplankton light scattering over absorption when chl is relatively high (>5 mg m^{-3}) (Campbell & Esaias, 1983). O'Reilly et al. (1998) found that band-ratio R$_{rs}$(510)/R$_{rs}$(555) yields the lowest RMS when chl values are well above 1.5 mg m^{-3}. O'Reilly et al. (1998) also reported more accurate chl estimates than ours using OC2d (RMSE$_{log10}$ = 0.235). However, their results are not strictly

comparable to ours since OC2d was originally developed with global data (SeaBAM), thus it was not tunned up to particular regions such the NGOA. Furthermore, SeaBAM dataset contains very little data from polar regions and chl measurements above 8 mg m^{-3}. The band-ratio $R_{rs}(510)/R_{rs}(555)$ was also a better predictor of chl in NGOA waters compared to those using shorter wavelengths because it was less influenced by non-phytoplankton constituents (e.g. gelbstoff) that absorb light very strongly in the blue spectra (λ<500 nm) (Sathyendranath et al., 2004), and pigment-packaging effects (Kahru & Mitchell, 1998). For this reason, chl band-ratio and spectral-curvature relationships with wavelengths shorter or equal to 490 nm did not work in this study. In a fjord-like embayment characterized by gelbstoff-rich waters, Sathyendranath et al. (2004) used an airborne band-ratio algorithm based on R_{rs} (510)/R_{rs} (550) and R_{rs} (620)/R_{rs} (550) values to estimate chl variability (3-22 mg m^{-3}). In coloured waters of Baltic Sea, Darecki et al. (2003) reported satellite-derived R_{rs} (550)/R_{rs} (590) as the most statistically significant algorithm to estimate chl values between (1-50 mg m^{-3}). Although no gelbstoff measurements were done during July-August 2002, the gelbstoff/packaging effect numerical filter (equation 11) suggested a significant contribution of humic substances/packaging effect to short-wave light attenuation. Important sources of gelbstoff in NGOA waters during summer are rivers (Royer, 1979). These freshwater inputs, originated by glacier/snow melting and sporadic runoff events, are enriched in colored substances when they cross anoxic-acidic ponds (muskeg meadows) rich on organic matter (e.g. wood detritus) (Terschak, 2002). Vertical mixing (inshore) and biological production

(offshore) cannot be ruled out as additional sources of gelbstoff during 2002 surveys (Pegau, 2002). Glacier plumes not influenced by muskeg meadows are low in humic substances even though they can still contributes significantly to light attenuation at shorter wavelengths (412-490 nm) since they are rich in suspended fine-sediment (Pegau, 2002; Curran et al., 2004). Based on chl estimations without gelbstoff (semianalytical algorithm, Carder et al., 1999) (data not shown) pigment-packaging also appeared to be in this study a major factor affecting band-ratio and spectral-curvature relationships at wavelengths below 500 nm. Another limitation of using shorter wavelengths (λ < 500 nm) to estimate chl in NGOA waters was their shallow penetration along the vertical. This fact was particularly disadvantageous in NGOA waters during summer since maximum chl values were typically situated below the detection limit of blue R_{rs} channels. In that regard, a green wavelength combination such OC2d was more efficient since it was able to reach deeper waters (mean first optical depth~ 7 m) where in most of the cases a maximum chl peak developed (mean depth ~9.3 m). For this reason, B_{EU} variability had a fair agreement with chl_{FOD} horizontal distributions. In North Sea during summer, sub-surface chl peaks determine timing of spawning of pelagic organism including fish (Munk & Nielsen, 1994), and an analogous situation was probably present in NGOA waters during this study.

In spite of the OC2d advantages respect to the other algorithms tested, chl estimates were less reliable a few kilometres away from the coast. In very near-shore waters (< 30 m), interference of bottom albedo reflectance is an issue. This effect is more pronounced between 550 and 620 nm and also depends on water-bottom optical

properties (Lee et al., 2001). In this study changes in green and brown algae abundances, and variations in sediment composition were expected to be the main factors increasing R_{rs} (553) respect with R_{rs} (553) values near the coast. For instances, dense beds of green and brown macroalgae, and sand-gravel bottom caused over-estimation chl_{FODest} values (Fig. 5c) around the eastern part of Spruce Island (Gulf of Alaska Coastal Imagery Site, CIRCA-EVOS, http://imf.geococh.html). In this particular day, bottom influence on total R_{rs} (553) received at the airborne sensor was also enhanced due to low tides (~1 m MLLW).

OC2d-derived chl_{FOD} showed that most fertile waters were preferentially located at the entrance of the Bays where large depth changes occur within short distances (< 10 km), northeast of Marmot Island, and over the N. Albatross Bank nearby Chiniak trough. Relatively high nutrients, strong currents, and irregular bottom morphology characterize similar areas (e.g. Portoloc bank, Stabeno et al., 2004). Interestingly, these habitats have also been associated with dense fishing stocks of walleye pollock (~64 % of the diet of Steller sea lion) (Logerwell et al., 2002). Although, chl_{FOD} distributions were roughly comparables between July and August and for the same region, chl_{FODest} values tended to increase during August surveys. This B built-up was mot probably related to higher water temperature and additional land-derived nutrient concentrations (e.g. Iron) during August even though the larger water stratification (Stabeno et al., 2004).

The approach used in this study to estimate chl distributions could be universal for Alaskan coastal waters even though algorithms must be tuned up locally and for the same season before they can be useful for other coastal areas.

Acknowledgements

References

Angliss, R.P., DeMaster, D.P., Lopez, A.L. (2001). Alaska marine mammal stock assessments, 2001. U.S. Dep. Comer., NOAA Tech. Memo. NMFS-AFSC-124, 203 p.

Blough, N.V., Zafiriou, O.C., & Bonilla, J. (1993). Optical absorption spectra of waters from the Orinoco river outflow: Terrestrial input of colored organic matter to the Caribbean. *Journal of Geophysical Research,* 98, 2271-2278.

Brickley, P.J., & Thomas, A.C. (2004). Satellite-measured seasonal and inter-annual chlorophyll variability in the Northeast Pacific and Coastal Gulf of Alaska. *Deep-Sea Research Part II*, 51, 229-245.

Brown, E.D., Churnside, J.H., Collins, R.L., Veenstra, T., Wilson, J.J., & Abnett, K. (2002). Remote sensing of capelin and other biological features in the North Pacific using LIDAR and video technology. *ICES Journal of Marine Science,* 59, 1120-1130.

Campbell, J.W., & Esaias, W.E. (1983). Basis for spectral curvature algorithms in remote sensing of chlorophyll. *Applied Optics,* 22, 1084-1093.

Carder, K.L., Chen, F.R., Lee, Z.P., & Hawes, S.K. (1999). Semianalytical Moderate-Resolution Imaging Spectrometer algorithms for chlorophyll a and absorption with bio-optical domains based on nitrate-depletion temperatures. *Journal of Geophysical Research,* 104, c3, 5403-5421.

Cressie, N.A.C. (1991), Statistics for Spatial Data, John Wiley and Sons, Inc., New York, 900 pp.

Curran, K.J., Hill, P.S, Milligan, T.G., Cowan, E.A., Syvitski, J.P.M., & Konings, S.M. (2004). Fine-grained sediment flocculation below the Hubbard Glacier meltwater plume. *Marine Geology*, 203, 83-94.

Darecki, M., Weeks, A., Sagan, S., Kowalczuk, P., & Kaczmarek, S. (2003). Optical characteristics of two contrasting Case 2 waters and their influence on remote sensing algortihms. *Continental Shelf Research*, 23, 237-250.

Eltermann, L. (1968). UV, visible, and IR attenuation for altitudes to 50 km, Report AFCRL-68-01653., U.S. Air Force Cambdrige Research Laboratory, Bedford, MA.

Gordon, H.R., & Clark, D.K. (1980). Atmospheric effects in the remote sensing of phytoplankton pigments. *Boundary-Layer-Meteorology,* 18, 299-313.

Gordon, H.R., Clark, D.K., Brown, J.W., Brown, O.B., Evans, R.H., & Broenkow, W.W. (1983). Phytoplankton pigment concentrations in the middle atlantic bight: comparisons between ship determinations and Coastal Zone Color Scanner estimates. *Applied Optics,* 22, 20-36.

Gordon, H.R., & Morel, A.Y. (1983). Remote assesment of coean color for interpretation of satellite visible imagery: a review. Springer-Verlag, New York, pp.114.

Gregg, W.W. (2002). Tracking the SeaWiFS record with a coupled physical/biogechemical/radiative model of the global oceans. *Deep-Sea Research Part II*, 49, 81-105.

Grew, G.W. (1980). Real-time test of MOCS algorithm during superflux 1980. In NASA CP-2188 (1981), p. 301.

Harding, L.W., Itsweire, E.C., & Esaias, W.E. (1994). Estimates of phytoplankton biomass in the Chesapeake Bay from aircraft remote sensing of chlorophyll concentrations 1989-92. *Remote sensing of environment,* 49, 41-56.

Hermann, A.J., Haidvogel, D.B., Dobbins, E.L., & Stabeno, P.J. (2002). Coupling Global and Regional Circulation Models in the Coastal Gulf of Alaska. *Progress in Oceanography*, 53, 335-367.

Hirons, A.C., Schell D.M., & Finney B.P. (2001). Temporal records of d13C and d15N in North Pacific pinnipeds: inferences regarding environmental change and diet. *Oecologia,* 129, 591-601.

Hu, C., Carder, K.L, & Muller-Karger, F.E. (2000). Atmospheric correction of SeaWiFS imagery: assessment of the use of alternative bands. *Applied Optics,* 39, 3573-3581.

IOCCG (2000). International Ocean Colour Coordinating Group. Remote sensing of ocean colour in coastal, and other optically-complex, waters. p140, Sathyendranath, S. (Ed.), Reports of the international ocean-colour coordinating group, No. 3, IOCCG, Dartmouth, Canada.

Kahru, M., & Mitchell, B.G. 1998. Spectral reflectance and absorption of a massive red tide off southern California. *Journal of Geophysical Research*, 103, C10, 21,601-21,609.

Lee, Z., Carder, K.L., Chen, R.F., & Peacock, T.G. (2001). Properties of the water column and bottom derived from Airborne Visible Infrared Imaging Spectrometer (AVIRIS) data. *Journal of Geophysical Research*, 106, 11639-11651.

Logerwell, E.A., Fritz, L., Hollowed A., McDermott, S., Stabeno, P., & Wilson, C. (2002). The fishery interaction team: Investigating the potential impacts of commercial fishing on the foraging success of endangered Steller sea lions. Alaska Fisheries Science Center, National Oceanographic and Atmospheric administration, report. April-June 2002.

Logerwell, E.A. Hollowed, A.B., Wilson, C., & Stabeno, P. (2003). Does climate-driven variability in the oceanographic structure of the Gulf of Alaska shelf affect fish community composition by modulating the degree of interspecific competition between juvenile pollock and capelin?. Cimate variability and Sub-Artic Marine Ecosystems Symposium, May 16-20 2005, Victoria, Canada.

Loughlin, T.R., & York A.E. (2000). An accounting of the sources of Steller sea lion, Eumetopias jubatus, mortality. *Marine Fisheries Review,* 62, 40-45.

Morel, A., & Bricaud, A. (1981). Theoretical results concerning light absorption in a discrete medium and application to the specific absorption of phytoplankton. *Deep Sea Research*, Part A, 28, 1,357-1,393.

Munk, P., & Nielsen, T.G. (1994). Tropho-dynamics of the plankton community at Dogger Bank: predatory impact by larval fish. *Journal of Plankton Research*, 16, 1,225-1,245.

Neckel, H., & Labs, D. (1984). The solar radiation between 3300 and 12500. *A Sol. Phys.*, 90, 205-258.

O'Reilly, J.E., Maritorena, S., Mitchell, B.G., Siegel, D.A., Carder, K.L., Garver, S.A., Kahru, M., & McClain, C. (1998). Ocean color chlorophyll algorithms for SeaWiFS. *Journal of Geophysical Research,* 103, c11: 24,937-24,953.

Pegau, V.S. (2002). Inherent optical properties of the Central Artic surface waters. *Journal of Geophysical Research*,107, c10, 8035.

Perez-Ruzafa, A., Gilabert, J., Bel-Lan, A., Moreno, V., & Gutierrez, J.M. (1996). New approach to chlorophyll a determination in shallow coastal waters by remote sensing. *Scientia Marina,* 60, 19-27.

Reinersman, P., & Carder, K.L. (1995). Monte Carlo simulation of the atmospheric point-spread function with an application to correction for the adjacency effect. *Applied Optics,* 34, 4453-4471.

Royer, T.C. (1979). On the effect of precipitation and runnof on coastal circulation in the Gulf of Alaska. *Journal of Physical Oceanography*, 9, 553-563.

Sambrotto, R.N., & Lorenzen, C.J. (1987). Phytoplankton and primary production. In D.W. Hood and S.T. Zimmerman (Eds.). The Gulf of Alaska (pp. 249-282). U.S. Dep. Of Commerce.

Sathyendranath, S., Platt, T., Irwin, B., Horne, E., Borstad, G., Stuart, V., Payzant, L., Maas, H., Kepkay, P., Li, W.K.W., Spry, J., & Gower, J. (2004). A multispectral remote sensing study of coastal waters off Vancouver Island. *International Journal of Remote Sensing,* 25, 893-919.

Sokal, R.R., & Rohlf, F.J. (1995). *Biometry*, W.H. Freeman & Company, New York 498 pp.

Stabeno, P.J., Bond, N.A., Hermann, A.J., Kachel, N.B., Mordy, C.W., & Overland, J.E. (2004). Meteorology and Oceanography of the Northern Gulf of Alaska. *Continental Shelf Research,* 24, 859-897.

Terschak, J.A. (2002). Phenanthrene adsorption by melanoidins and marine humic acids. PhD. Dissertation, University of Alaska Fairbanks.

Venrick, E.L., & Hayward, T.L. (1984). Determining chlorophyll on the 1984 CalCOFI surveys. *CalCOFI Reports*, 25, 74-79.

Wessel, P., & Smith, W.H.F. (1996). A global, self-consistent, hierarchical, high-resolution shoreline database. *Journal of Geophysical Research*, 101, 8741-8743.

Wynne, K., & Foy R.J. (2002). Is it food now? Gulf Apex Predator-prey study. In Steller *Sea Lion Decline: Is it Food II.* (Eds.) D. DeMaster and S. Atkinson. University of Alaska Sea Grant, AK-SG-02-02, pp. 49-52.

Table 1: Flight track ancillary data and main remote-sensing variables during aerial surveys over coastal waters of Afgonak/Kodiak shelves. Time: local time, Acov: surface area coverage (km^2) 10^3, Lat: latitude (°), Lon: longitude (°), Zcov: bottom depth range (m), θ_o = solar zenith angle (°), D: photoperiod (h).

Date	Time	Acov	Lat	Lon	Zcov	θ_o	D
7/27/02	7:00-12:55	3.68	57.71, 58.71	-152.75, -151.08	21-260	39.8-51.3	16.5
7/28/02	9:00-10:33	1.18	57.39, 57.73	-152.46, -151.54	11-221	41.9-50.8	16.3
8/17/02	9:00-11:20	1.66	57.48, 58.04	-152.91, -151.67	50-216	45.6-55.5	15.0

Table 2: Water-leaving radiance and remote-sensing reflectance measurements over coastal waters of Afgonak/Kodiak shelves. nL_w: nadir-normalized water-leaving radiance ($\mu W\ cm^{-2}\ nm^{-1}\ sr^{-1}$), R_{rs}: remote-sensing reflectance (sr^{-1}) (10^{-3}). MicroSAS channels (nm) are indicated in the second row. Between parentheses is one standard error.

Date	nL$_w$						R$_{rs}$[a]				
	411	443	491	509	553	665	411	443	491	509	553
7/27/02	0.326 (.005)	0.406 (.006)	0.478 (.007)	0.448 (.006)	0.443 (.006)	0.364 (.017)	3.9	4.4	4.7	4.5	4.6
7/28/02	0.166 (.003)	0.219 (.004)	0.272 (.004)	0.242 (.004)	0.219 (.004)	0.172 (.012)	2.2	2.6	2.9	2.6	2.6
8/17/02	0.228 (.008)	0.275 (.010)	0.319 (.013)	0.279 (.013)	0.329 (.020)	0.154 (.015)	2.7	3.0	3.0	2.6	3.3

[a] standard error for all wavelengths was $1 \cdot 10^{-4}$.

Fig. 1. Airborne, ship and satellite surveys over the study area. (a) Geographic location of Afgonak/Kodiak Islands in the northern part of the Gulf of Alaska; the small inset showed with more detail the area where pigment concentrations were estimated during aerial measurements, (b) flight tracks during July (red dots) and August (blue dots) 2002, (c) field chl measurements of FOY dataset (2002 July: red dots, August: blue dots), PEGAU dataset (2003, May-July-August) image coordinates (yellow dots); Validation points of airborne R_{rs}-chl relationship (green dots) based on shipboard, satellite (SeaWiFS) and airborne reflectance measurements; notice that all chl sampling stations of CARDER dataset were used to test the chl remote-sensing models.
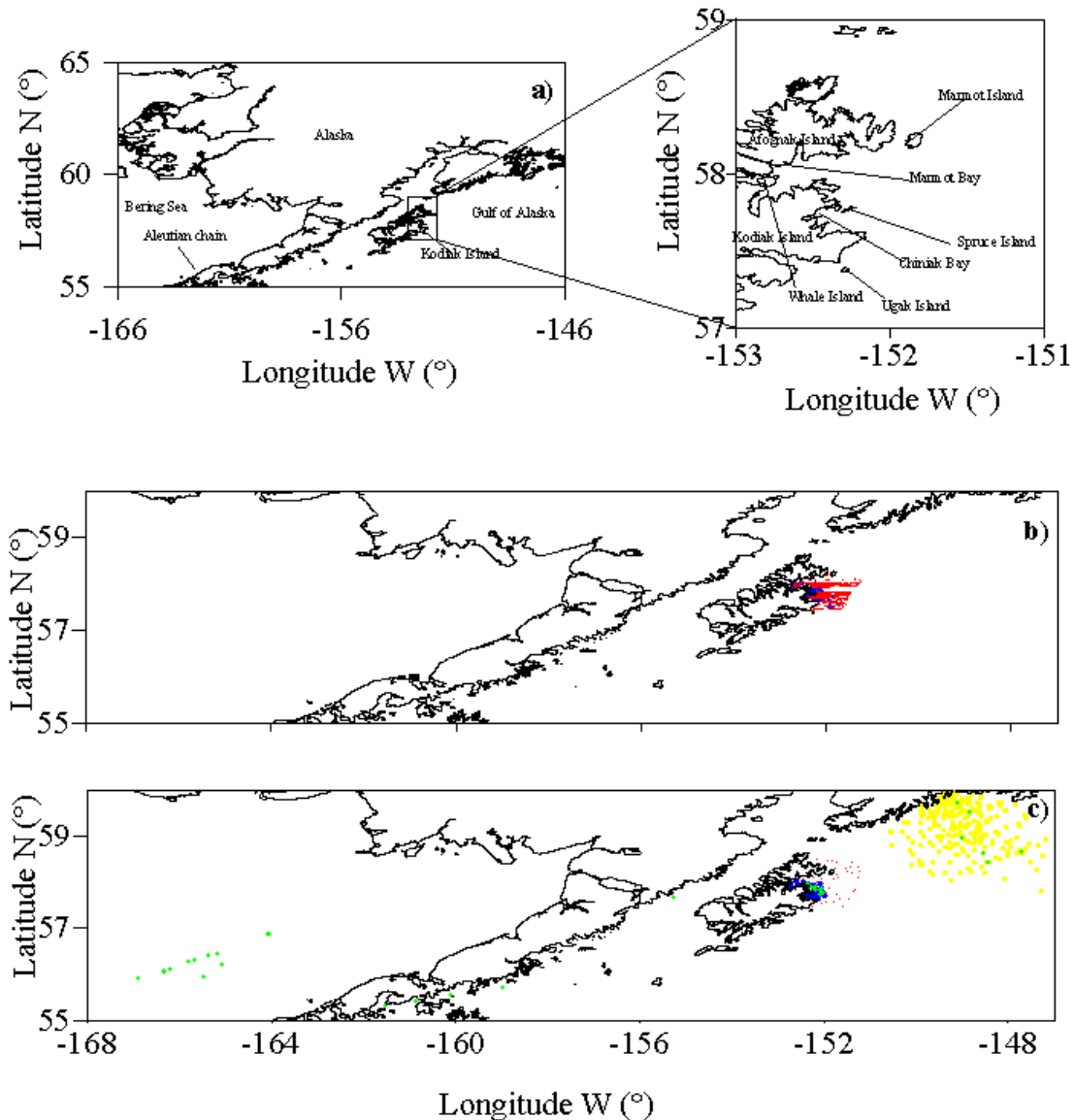
Fig. 2. Typical remote-sensing reflectance spectra and bathymetry of Afgonak/Kodiak shelf waters. (a) Spectral reflectance curves for shallow/deep and inshore/offshore waters, (b) Bathymetric levels on the eastern shelf of Afgonak/Kodiak Islands and position of $R_{rs}(\lambda)$ spectra, Fig. 2a. Shallow banks (<50 m) and troughs (~200 m) are represented with blue and red colors, respectively. Portlock bank is situated northeast of Marmot Island (58.5° N, -150.5° W).
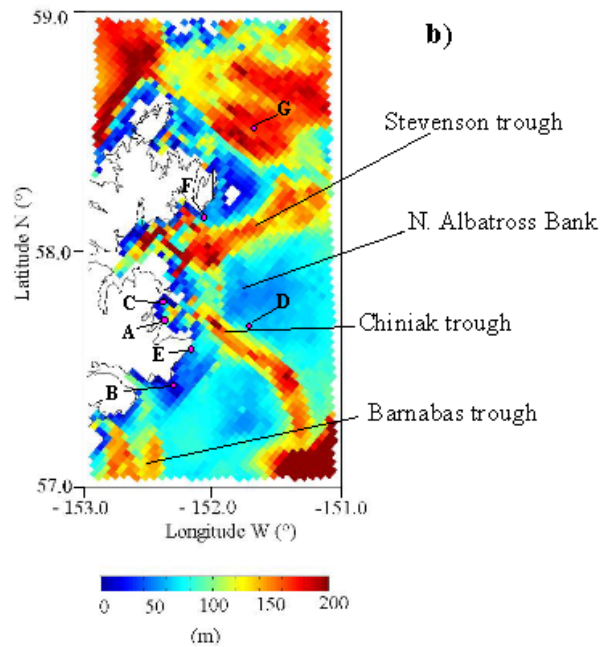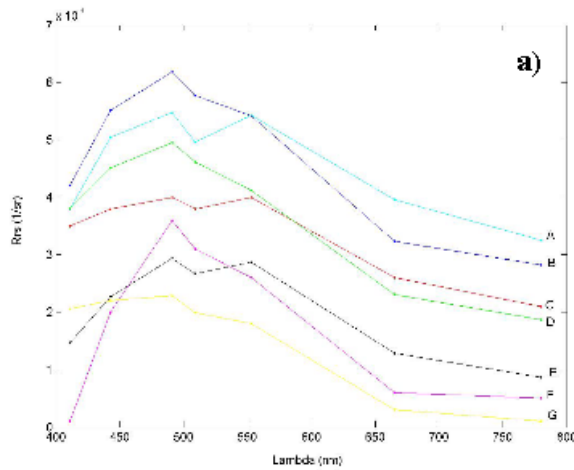
Fig. 3. Performance of band-ratio and spectral-curvature algorithms to retrieve chlorophyll *a* concentrations at the first-optical depth of Alaskan Coastal waters. (a) SeaWiFS OC2a, (b) SeaWiFS OC2b, (c) SeaWiFS OC2, (d) $G_{1,1}(491)$; R represents the ratio of R_{rs} for band-ratio or spectral-curvature algorithms, modified cubic polynomial models of chl (solid line) (O'Reilly et al., 1998), linear regression fitting (dotted line), field data (solid circles).
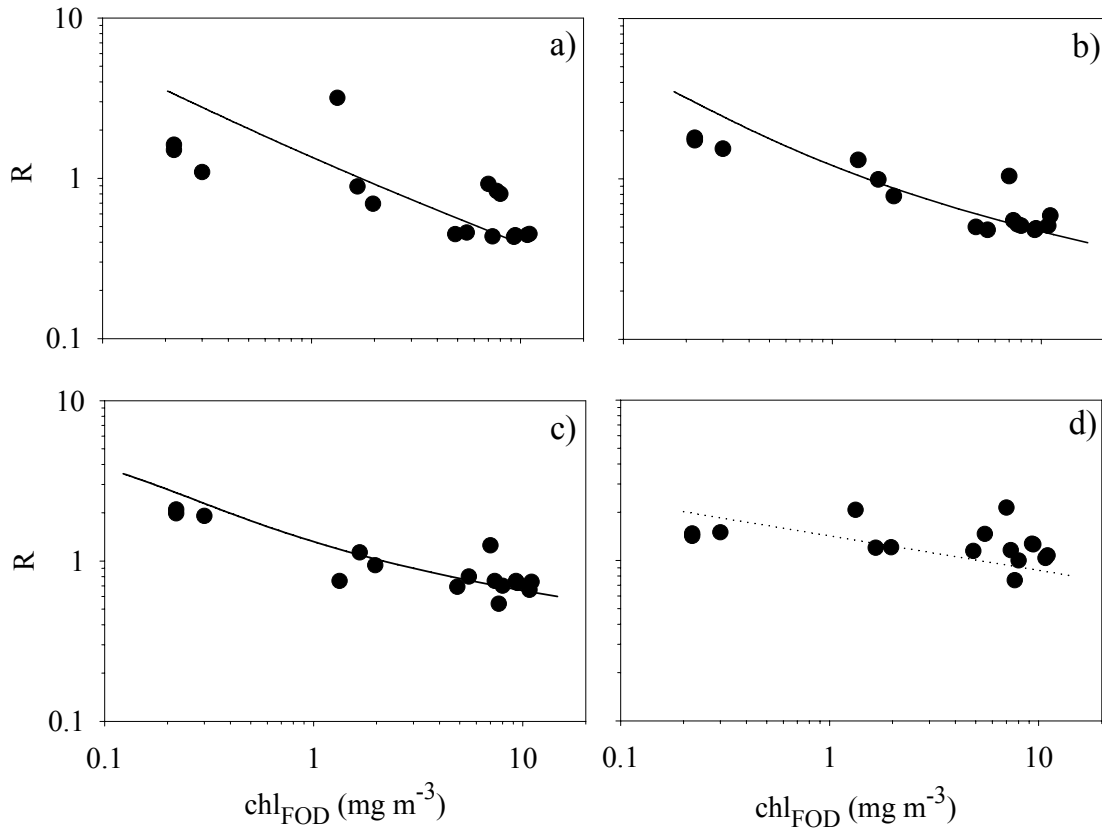
Fig. 4. Airborne remote-sensing algorithms to estimate chlorophyll in coastal waters of NGOA. (a) log-log relationship between reflectance ratio ($R = R_{rs}(510)/R_{rs}(555)$) and chl values for the first optical depth, theoretical chl values calculated from OC2d algorithm and using R values determined by different sensors are represented with a solid line, airborne data 2002: crosses, n = 6, SeaWiFS 2002 dataset: solid triangle, n = 10, SeaWiFS 2003: solid circle, n = 6, *in situ* shipboard: open circles, n = 33, (b) relationship between field chlorophyll measurements (chl_{FOD}) and calculated chl values using OC2d, 1:1 curve between observations is indicated with a solid line.
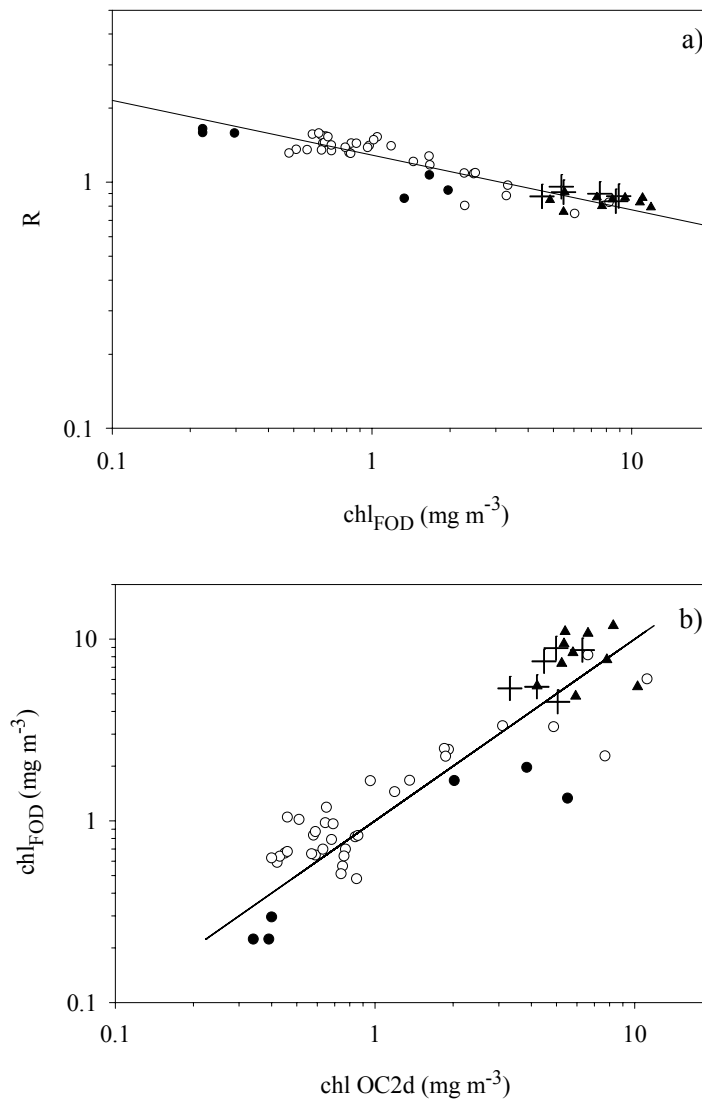
Fig. 5. Horizontal distributions of estimated chlorophyll concentration at the first optical depth during summer 2002. (a) 27 July, (b) 28 July, (c) 17 August.
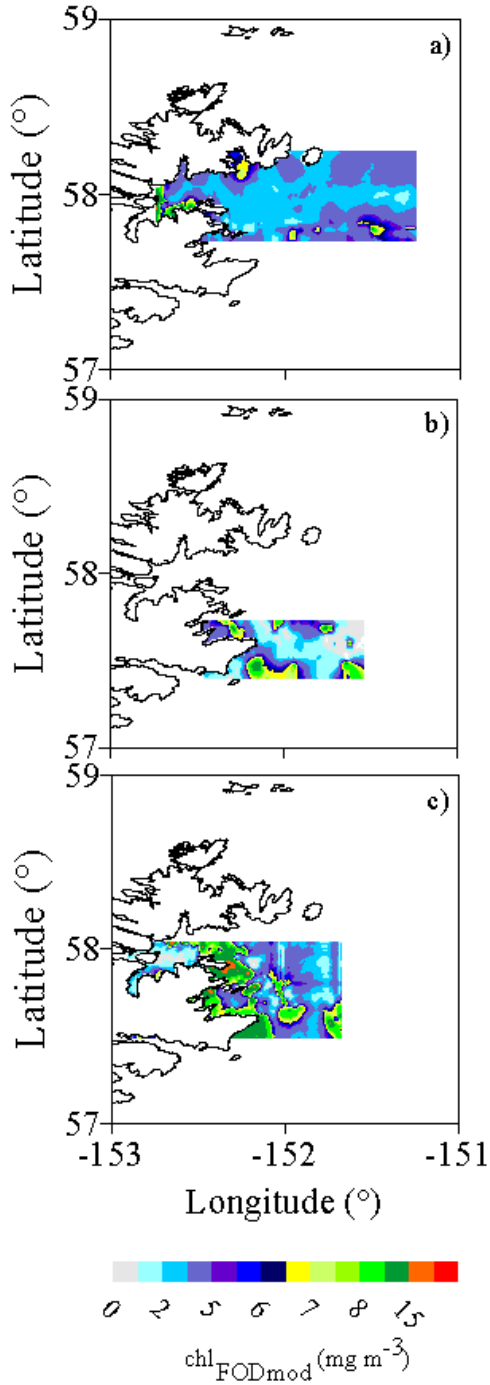
Fig. 6. Horizontal distribution of ancillary hydrographic information during summer 2002. (a) temperature, (b) salinity, (c) water column stratification.
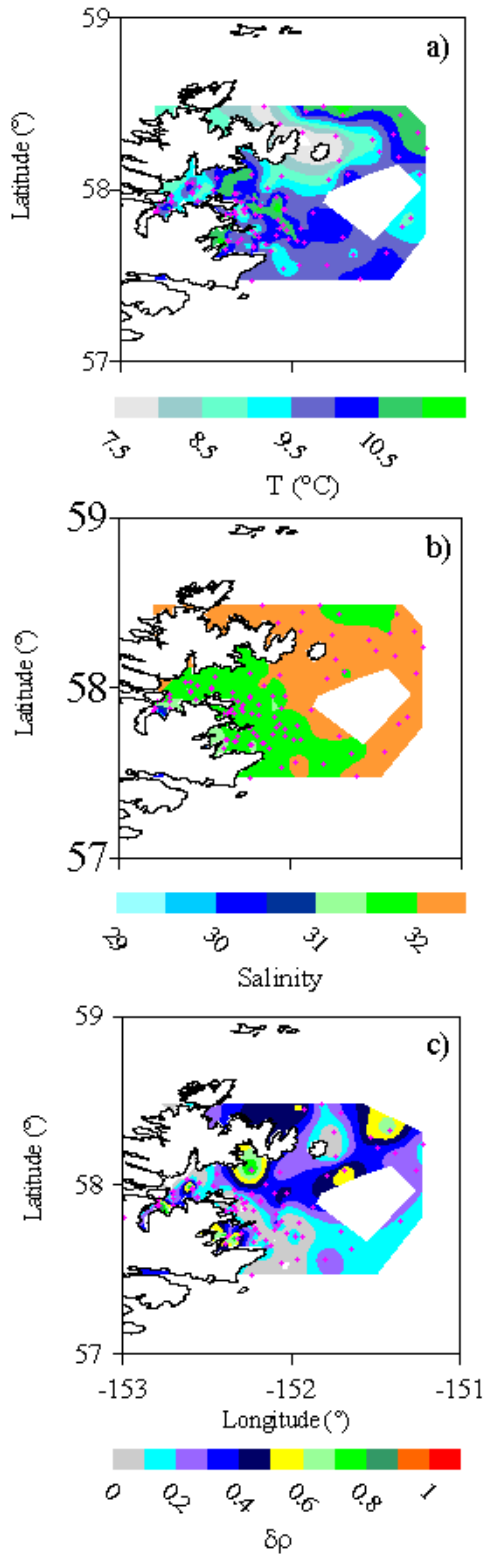
Fig. 7. Numerical filter for detecting waters with different gelbstoff content in coastal waters of Afgonak/Kodiak shelves. (a) 27 July, (b) 28 July, (c) 17 August 2002. The solid line in each panel represents the case I filter: $R_{rs}(412)/R_{rs}(443) = 0.95 [R_{rs}(443)/R_{rs}(555)]^{0.16}$. Gelbstoff enrichment and/or phytoplankton cells with significant packaging effects characterize dots below this line.
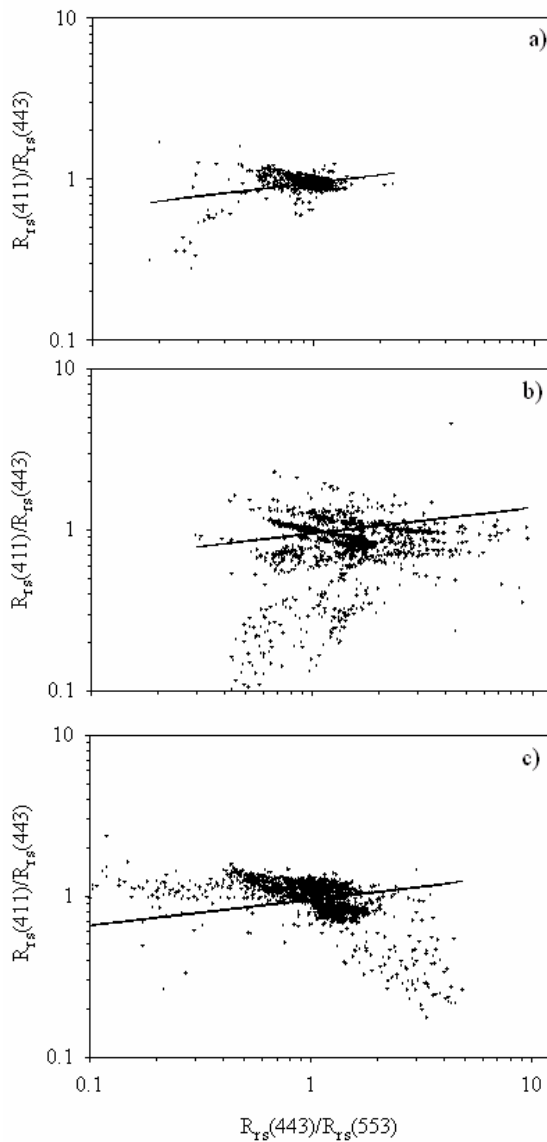
Fig. 8. Horizontal distribution of ancillary optical and biological information during summer 2002 (a) PAR transmission between 0 and 20 m, (b) integrated chl throughout the euphotic zone (B_{EU}).